Post-Disaster Damage and Response Assessment with PlanetScope Satellite Imagery

Case Study February 2023 Türkiye-Syria Earthquakes

Shreya Deep Bansod (S2483343)
July, 2024

SUPERVISORS:
Prof. Dr. Norman Kerle
Prof. Dr. Marc van den Homberg

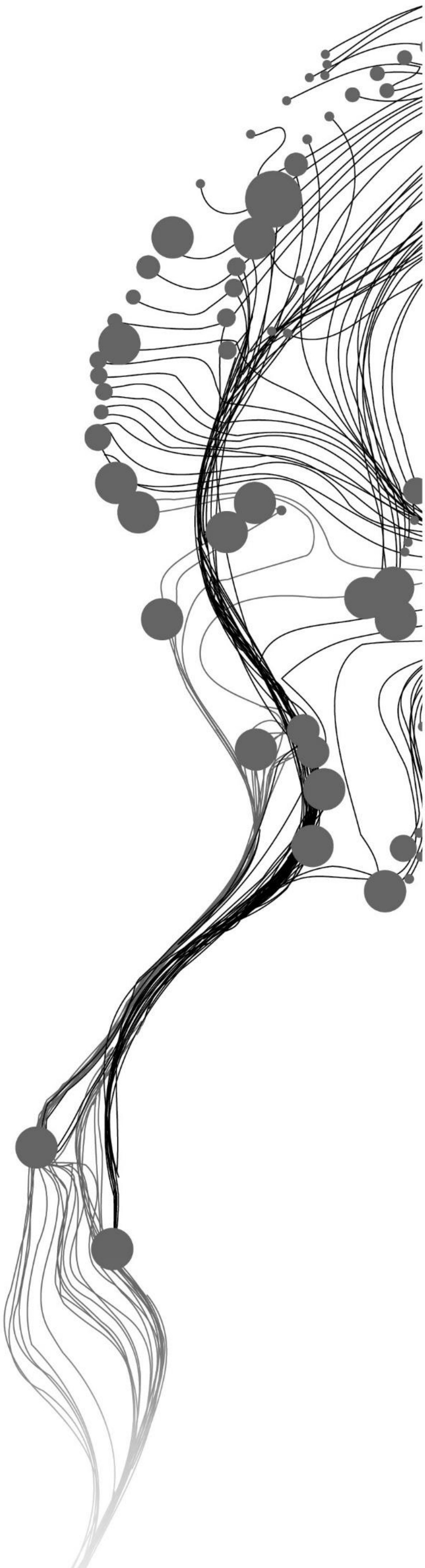

Post-Disaster Damage and Response Assessment with PlanetScope Satellite Imagery

Case Study February 2023 Türkiye-Syria Earthquakes

Shreya Deep Bansod (S2483343)
Enschede, The Netherlands, July 2024

Thesis submitted to the Faculty of Geo-Information Science and Earth Observation of the University of Twente in partial fulfilment of the requirements for the degree of Master of Science in Geo-information Science and Earth Observation.
Specialization: Natural Hazards and Disaster Risk Reduction

SUPERVISORS:
Prof. Dr. Norman Kerle
Prof. Dr. Marc van den Homberg

THESIS ASSESSMENT BOARD:
Prof. Dr. V. G. Jetten (Chair)
Prof. Dr. Henry Meissner, German Aerospace Center (DLR) (External Examiner)

ABSTRACT

Every year, major disasters occur worldwide, requiring substantial response and recovery efforts. These efforts are often hampered or delayed due to incomplete information from all affected areas. High-spatial resolution remote sensing data, such as optical imagery from satellites and 3D point clouds generated from sources like LiDAR etc. are widely used to support post-disaster phases, focusing mainly on damage assessment and long-term recovery. However, the immediate and short-term response often goes unmonitored once the event fades from the spotlight. Additionally, most efforts tend to concentrate on the major urban areas, making them highly location-specific and often neglecting rural and other hard-to-reach human settlements. This also leads to limited understanding of the complex response phase due to constraints like limited coverage, infrequent data, and high costs associated with very-high resolution remote sensing data. These limitations make such datasets unsuitable for large-scale damage assessments and frequent monitoring of dynamic activities after a disaster event.

This research therefore explores the utility of PlanetScope for (1) large-scale damage assessment covering both urban and rural areas, (2) detection and monitoring of response activities, and (3) integration with higher resolution images (WorldView and Pleiades) to understand their synergistic potential. PlanetScope is a constellation of 130+ satellite doves capturing almost the entire planet (except the poles) daily. The spatial resolution of PlanetScope is 3-4 meters, lower than WorldView and Pleiades. However, the spatial coverage and high temporal resolution provides the avenue to acquire images for any area of interest and date, except when hindered by high cloud cover or extreme events. Using the February 2023 Türkiye-Syria earthquakes as a case study, we employed texture feature extraction using GLCM for selected locations from Türkiye with a supervised machine learning algorithm, Random Forest, for classification. The potential of higher-resolution datasets was evaluated by using them as ground truth, confirming presence of activities in focus, and for enhancing PlanetScope image details through sharpening. Due to the limited availability of very-high-resolution images and ground truth data from Syria, the analysis primarily focused on locations in Türkiye. However, a location from Syria was selected to assess the generalizability of model trained and tested on data from Türkiye.

Our findings show that PlanetScope effectively supports grid-based damage detection, identifying zones with collapsed buildings and calculating damage densities to highlight hotspots in both densely (urban) and sparsely (rural) populated areas. PlanetScope imagery is also useful for monitoring response activities, such as the evolution of temporary shelters and debris detection. However, damages not showing debris or missing roofs and small isolated temporary shelters are challenging to detect due to PlanetScope's nadir acquisition and limited resolution. High temporal resolution of PlanetScope aids debris detection but is less effective for tracking removal due to the limitation posed by its spatial resolution and unavailability of related ground truth data. Integration of PlanetScope with higher-resolution data in multiple ways shows their synergistic potential to produce a detailed and comprehensive damage assessment. However, large-scale assessment and frequent monitoring can be hindered by the limited coverage and frequency of the higher-resolution satellite images. Lastly, the generalizability test conducted on a location in Syria showed that direct application of the model resulted in poor accuracy due to differences in settlement pattern and texture properties between the two regions. However, when the model was trained on data from Syria, it achieved high accuracy.

In conclusion, the results prove that PlanetScope can effectively support rapid, large-scale damage and response assessment that can enable efficient allocation of resources and support for emergency responders. Advance feature extraction and classification algorithms can further help in improving the accuracy of results. Additionally, advance integration methods can help in enhancing details of PS images which can also lead to direct quantification of changes observed resulting in more meaningful insights.

ACKNOWLEDGEMENTS

Reflecting on the past two years, I realize that this period has represented the steepest learning curve of my life so far. First and foremost, I extend my heartfelt gratitude to my supervisor, Prof. Dr. Norman Kerle, for his patient and constant mentorship since the beginning of this MSc course. Working under his guidance inspired me to step outside my comfort zone, challenge myself, and explore avenues that have proven beneficial even beyond the scope of this thesis. I am also deeply thankful to Prof. Dr. Marc van den Homberg for his guidance, support, and motivation throughout the entirety of this thesis, internship, and beyond. His energy and enthusiasm have been a constant source of inspiration for me. Special appreciation goes to Prof. M. Sonobe and Prof. A.C. Blanco for their prompt responses to my doubts regarding the methodologies of their respective papers, which significantly helped me in my research. I also sincerely thank Bruno, for his help in planning out my work timeline numerous times and also providing solutions to my thesis-related concerns and worries.

I am grateful to the ITC Faculty for selecting me as one of the recipients of the ITC Excellence Scholarship, without which I would not have been able to embark on my master's journey at the University of Twente. My sincere thanks to Nirat, for providing the necessary financial support when I did not want to seek support from my parents and the banks in India were slow to process my loan application (my stubborn self was determined to take full responsibility for pursuing a post-graduate degree abroad). I extend my gratitude to Gurkaran for his friendship and mentorship. Acknowledging my writing skills were not the strongest (and they remain a work in progress), he was instrumental in helping me articulate my ideas for the motivation letter when I was applying for MSc courses back in 2022.

I am indebted to my parents and my brother, who have always supported my decisions and have been there for me, particularly during challenging or overwhelming times far from home. I also thank my friends- Shubham, Tanmay, Manisha, and Gurkaran- for always checking up on me despite the time zone difference. They provided me with a space to vent and share my happiness. Special thanks to Tanmay for studying with me online and keeping me company on days when working alone on the thesis felt particularly isolating. I would also like to thank my friends- Girija, Chakshu, Wibi, Sry, Salsa, Faheed, Surya, Aleksandra and Sachi who made me feel at home away from home and were always there whenever I reached out for help. Additionally, I express my gratitude to Nishit, who was not only a friend but also a mentor when I started this thesis. His insights during our post-dinner long walks provided me with clarity on the possibilities and helped build a strong foundation for my thesis.

Lastly, I extend my deepest thanks to Rutger, who made my thesis journey less stressful, helped me achieve a healthy balance with work, and instilled confidence in me with his constant cheerleading. I also appreciate his family and friends for their warm welcome and for making me feel at home, helping me miss my family a little less.

I apologize if I have missed mentioning anyone in this section. I extend my heartfelt thanks to every person who has contributed to making life easier during my MSc course in one way or another. My heart is full, and I am immensely grateful for this entire master's journey. I will surely reminisce about these days with fondness in the years to come.

"Be not afraid of going slowly, be afraid only of standing still."

TABLE OF CONTENTS

LIST OF FIGURES

LIST OF TABLES

LIST OF EQUATIONS

LIST OF ABBREVIATIONS

AOI- Area of interest
ANN- Artificial Neural Networks
AUC- Area Under Curve
CNN- Convolution Neural Networks
EMS- Emergency Management System
FEMA- Federal Emergency Management Agency
FN- False Negative
FP- False Positive
GA- Genetic Algorithm
GCP- Ground Control Points
GLCM- Gray Level Co-Occurrence Matrix
IFRC- International Federation of Red Cross
KDE- Kernel Density Estimation
LBP- Local Binary Patterns
LCLU- Land Cover Land Use
LiDAR- Light Detection and Ranging
MODIS- Moderate Resolution Imaging Spectroradiometer
NA- Not Available
OBIA- Object-based Image Analysis
OSM- OpenStreepMap
PS- PlanetScope
QGIS- Quantum Geographic Information System
RNN- Recurrent neural network
ROC- Receiver Operating Characteristic
RS- Remote Sensing
SAR- Synthetic Aperture Radar
SVM- Support Vector Machine
TLS- Terrestrial Laser Scanning
TN- True Negative
TP- True Positive
UAV- Unmanned Aerial Vehicle
UNDRR- United Nations Office for Disaster Risk Reduction
UNHCR- United Nations High Commissioner for Refugees
VIIRS- Visible Infrared Imaging Radiometer Suite
WHO- World Health Organisation

1. INTRODUCTION

1.1. Background

Throughout Earth's history, natural hazards have been an inevitable part of the planet. These hazard events, when causing disruptions to the functioning of a community or society, are called disasters (UNISDR, 2015). Slow-onset hazardous events like drought, sea-level rise etc. develop gradually and can be predicted well in advance. This provides time to take measures or anticipatory actions to mitigate the predicted impact ahead of the hazards (IFRC, 2021). While sudden-onset disasters like earthquakes, flash floods etc. are not only difficult to predict but their unforeseeable severity and scale pose a unique challenge because adequate response and recovery resources cannot be allocated in advance for all the impacted regions.

Disaster response begins immediately after the disaster to save lives and address the essential requirements of the affected population (UNDRR, 2013). This is followed by the recovery phase (Figure 1) which focuses on reinstituting the disaster-affected community or society, their assets, systems and activities to mitigate future disaster risk (UNISDR, 2015). Post-disaster response and recovery are complex processes that are least understood, with this period often going unnoticed or unmonitored (Ghaffarian and Emtehani, 2021) when the disaster event fades from the spotlight. This also contributes to disproportionate disaster relief and response efforts as comprehensive information from all vulnerable places fails to reach the responding authorities. Therefore, complete information on the extent of damage and subsequent response is vital for ensuring adequate post-disaster assistance and distribution of resources to all the affected population.

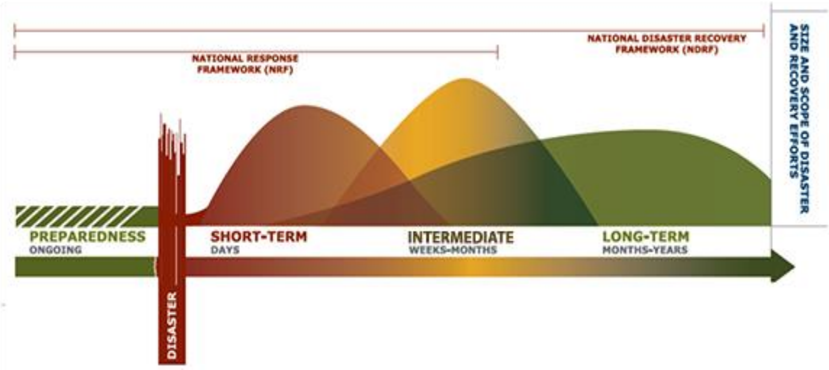

Figure 1. Response and recovery Continuum with corresponding activities by FEMA (FEMA, 2016)

Disaster response efforts are managed by multiple stakeholders (Table 1) who may directly or indirectly interact to address various interdisciplinary tasks effectively (Fontainha et al., 2022). These stakeholders include local, national and international government and/or non-governmental organizations, volunteer groups and community members depending on the scale and impact of the disaster event. The resilience of the impacted community majorly depends on how effectively these organisations coordinate and implement their responses (Norris et al., 2008).

Table 1. Stakeholders in disaster response (Shafique and Warren, 2016)

Stakeholders	Primary function	Information needs	Direct use of RS data
Affected community, volunteer groups	First responders before external support arrives, identifying immediate needs	Extent and impact of disaster event	✓
		Aid distribution	✓
Government organisations	Coordinating response activities, supporting needs assessment, allocation of resources, and information dissemination to the affected population	Damage assessments	✓
		Impacted population	✓
		Resources needed	×
NGO	Offering support with relief operations like medical aid, shelter, food etc., facilitating participation of the community	Needs assessment	✓
		Coordination points with other authorities	×
Private organisations	Providing resources and expertise, supporting relief operations through CSR activities	Resource requirements	×
Donors	Providing financial support	Financial needs and budget	×
Academia	Providing policy recommendations based on analysis and research	Access to data and information for analysis	✓

From Table 1, it can be seen that the use of different remote sensing (RS) data are vital in understanding and supporting post-disaster activities concerning response and recovery. Their properties, such as multispectral information from optical imagery, all-weather and day and night imaging by SAR, the high point-cloud density of LiDAR and the flexibility of UAVs to be flown at a desired altitude with any sensor over the area of interest, make RS data a valuable source for facilitating post-disaster decision making. Recent studies have also emphasized the application of various supervised and unsupervised machine learning techniques, particularly when dealing with extensive datasets that focus on improving methodologies and providing new approaches in addition to integrating multiple high-resolution remote sensing data.

Supervised machine learning models include algorithms like random forest (RF), extreme gradient boosting (XGBoost) and support vector machine (SVM) are often used for classification tasks. These algorithms depend on a labelled dataset for training followed by using the learnt information to map new instances (Alloghani et al., 2020). On the other hand, unsupervised algorithms like autoencoders, and generative adversarial networks (GAN) learn data based on pattern recognition and show the most utility in cases where a labelled dataset is absent or to create a labelled dataset which is further used in a supervised learning task (Hofmann, 2001). The selection of the machine learning method depends largely on the scope and requirement of the study, for example, Chen et al. (2022) in their research on identifying building cracks highlighted the absence of annotated point cloud and the time-consuming nature of creating labelled datasets made them opt for unsupervised learning method for their research. Whereas Virtriana et al. (2023) used the random forest algorithm for damage classification because of its ability to handle large datasets, stability against outliers and parallel processing.

A common observation across multiple studies indicates that some use remote sensing data predominantly for direct physical assessments, such as quantifying building damages (Liu et al., 2022; Valentijn et al., 2020). While some use it to analyse processes indirectly, such as monitoring land cover and land use (LCLU) changes for recovery (Ghaffarian and Kerle, 2019). The latter shows that even though direct information on certain processes might not be available, the more subtle or indirectly observable features can be used as proxy indicators to gain insights into various processes (Table 2). These features refer to the characteristics or attributes that can be extracted from remote sensing data that highlight specific activity or changes in the scene (Salau and Jain, 2019). Table 2 shows that spectral and texture features have been largely used to identify damaged buildings/areas by studying the changes and irregularities and, measuring the number of reconstructed buildings to assess progress in recovery are some examples of the use of such proxy indicators (Ghaffarian et al., 2018).

Table 2. Features with remote sensing data requirement.

Activity	RS indicators	Features				RS data requirement	References
		Geometry	Texture	Spectral metric	Land use/ cover		
Damage detection Damages (Table 3: scale) can be observed immediately after the primary and secondary events	Building deformation	✓	✓	✓		Primary damages: Bi-temporal pre- and post-event images Secondary damages: multi-temporal post-event images.	(Adriano et al., 2019; Tong et al., 2012)
	Structural/building damages	✓					
	Road/urban areas/vegetation	✓	✓	✓	✓		(Havivi et al., 2022; Izadi et al., 2017)
	Damage extent		✓	✓	✓		(Olorunfemi et al., 2020; Stone and Mohammed, 2017)
Response Begins immediately after the disaster event and can be observed for several days, weeks or months	Construction of temporary shelters		✓	✓		Hyper-temporal post-event images (frequent-daily or weekly)	(Omarzadeh et al., 2021)
	Debris removal		✓	✓			(Khodaverdizahraee et al., 2020)
	Demolition of collapsed structures		✓	✓			(Pirrone et al., 2020)
	Population displacement			✓	✓		(Braun et al., 2019)
	Power outage			✓		Pre and post- multi-temporal images	(Román et al., 2019)

Table 3. Damage scale (adopted from Copernicus EMS classes)

Damage scale	Description
Minor	Slight damages such as gaps on the roof surface
Major	Substantial changes such as partial roof or wall collapse
Complete	Destruction such as the collapse of building(s)

Geometric features in RS correspond to shapes focusing on lines and edges (Salau et al., 2019) while spectral features are extracted by combining different bands to retain the most significant feature (Kumar et al., 2020). Land cover refers to the physical and biological attributes of the earth's surface such as soil and vegetation types, water bodies etc. and the ways in which human activities have made use of the land is referred to as land use (Liping et al., 2018). Texture features are extracted from the spatial arrangement of pixel values in an image and are more commonly used compared to other features because they do not require image segmentation beforehand (Kupidura, 2019). Table 2 provides examples of studies in which these features have been used to support post-disaster response assessments focusing on specific activities. Due to the exploratory nature of this research coupled with the properties of data being used, the study primarily concentrates on texture features (explained further in section 2.3.4).

While the several remote sensing data sources with evolving analysis methodologies have made it possible to capture post-disaster details at different levels, many reasons make such sources suboptimal for monitoring the immediate response activities. For example, response activities like demolition of damaged structures, clean-up of debris, and transition of shelters (temporary to semi-permanent) remain undocumented due to the unavailability of frequent data for the area of interest. Moreover, the cost of such high-resolution data is high (Appendix 1), making it an expensive exercise to cover and monitor the entire impacted region regularly.

Additionally, current research in the realm of post-event damage (Wu et al., 2021) and response assessment (Antoniou et al., 2020) using remote sensing data focuses mostly on urban or densely populated areas. Vulnerable communities residing in remote, peripheral, and rural locations who are disproportionately affected due to their social and economic vulnerabilities get less attention due to their geographic isolation (Metzger et al., 2014). One of the other contributing factors to this oversight in research is the absence of a comprehensive multi-temporal dataset (both pre- and post-disaster) for such regions (Figure 3).

In conclusion, the limited spatial coverage and low temporal resolution of currently used datasets often overlook other affected areas and hinder the ability to capture immediate post-disaster changes.

1.2. Research motivation

In recent years, the PlanetScope (PS) constellation of 130 satellites covering approximately 200 million km² every day (Frazier et al., 2021) has gained considerable interest from researchers, particularly in monitoring frequent changes in any area of interest. PS provides low-cost, high resolution (3 – 4 m) at nadir, 4 and 8-band imagery with three products - basic scene, ortho scene and ortho tile. Except for the former, the ortho products are orthorectified with additional post-processing applied, making them almost analysis-ready.

In the domain of disaster management, the potential of PS has been studied for hazard mapping, monitoring and detecting changes, such as land use/land cover changes (Filho et al., 2023; Wang et al., 2022), wildfire damage assessment (Chung et al., 2020), flood mapping (Leach et al., 2022), extracting building inventory information (Kaplan and Kaplan, 2020), integration with very-high resolution data for building damage detection (Fu et al., 2022) and damage assessment using spatial autocorrelation (Blanco, 2022). Despite its versatility, PS's utility in understanding the post-disaster response phase remains underexplored. Undertaking research focusing on very detailed assessment and monitoring with PS data alone may pose challenges due to its spatial resolution of 3-4 meters (Figure 2), in addition to reduced utility during unfavourable atmospheric or cloud conditions (Figure 7).

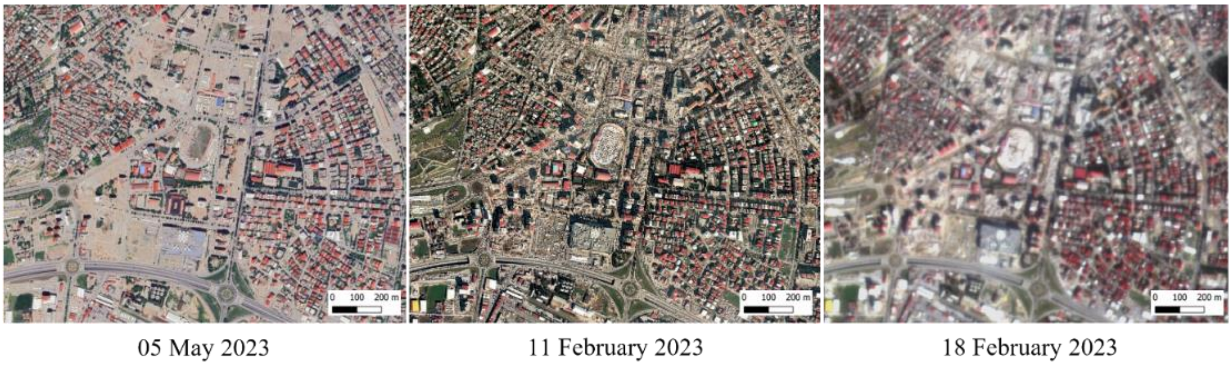

Figure 2. Comparing satellite data: SPOT (left), WorldView (centre), PlanetScope (right)

However, its high temporal resolution (near daily revisit time) and large coverage offer opportunities to explore large-scale damage and response assessment covering inaccessible or hard-to-reach locations that may further help address the oversight of remote communities (Figure 3).

Figure 3. Pre- and post-event data availability from different high-resolution satellite data sources for the Kahramanmaraş earthquakes that occurred on 6th February 2023. The scene covers the province of Hatay from Türkiye and its surrounding region spanning an approximate area of 7800 km² that experienced several aftershocks with the highest magnitude of 6.7. (a) WorldView (0.3 meters), (b) SPOT (1.5 meters), (c) Pleiades (0.5 meters), (d) Pleiades Neo (0.3 meters), (e) PlanetScope (3 meters).

This research aims to assess the extent to which PlanetScope (PS) data can be used to support post-disaster damage and response assessment. The Türkiye – Syria 2023 7.8 magnitude earthquake was selected as the case study, which occurred on 6th February. This study utilises hyper-temporal PlanetScope and available multi-temporal WorldView and Pleiades images from the event. The research will compare the availability of data and information from PlanetScope with additional higher-resolution images to understand how PS presents additional and complementary potential to support post-disaster damage and response assessment.

1.3. Objectives and research questions

1.3.1. Main objective

To analyse the suitability of PlanetScope (PS) in identifying post-disaster damages, and response activities using texture-based feature extraction and supervised machine learning algorithm for classification for the case study of 2023 Türkiye - Syria earthquake struck regions.

1.3.1.1. Sub objectives and research questions

i. To investigate the utility of PlanetScope in detecting post-disaster damage.
    - Can PS be used to undertake damage detection in both densely and sparsely populated regions?
    - Can the identified damage by PS be quantified?
    - How well does the generalizability of the damage detection model trained and tested on data from Türkiye extend to detecting damage in Syria?

ii. To investigate the utility of PlanetScope in detecting post-disaster response activities.
    - For which response activities can PS be used to monitor in both densely and sparsely populated regions?
    - Can the identified activities by PS be quantified?

iii. To determine the synergetic potential of PS with available higher resolution satellite images to increase the comprehensiveness of change detection using data integration technique.
    - How can higher-resolution data be integrated with PS?
    - How does the incorporation impact the comprehensiveness of damage and response assessment?

1.4. Thesis structure

The chapters of this thesis are organized as follows:

- Chapter 2 offers a comprehensive literature review focusing on the post-disaster response phase. It details the use of remote sensing data to support this phase, with further emphasis on the application of PS data for the same.
- Chapter 3 describes the study areas and data used in this research.
- Chapter 4 outlines the methodology employed to address the research questions.
- Chapter 5 presents the results obtained in each step of this research for the sub-objectives.
- Chapter 6 provides a detailed discussion of the results and their implications in the context of the research questions.
- Chapter 7 highlights the identified limitations, offers recommendation for future work, and includes the concluding remarks.

2. LITERATURE REVIEW

This chapter provides a comprehensive literature review, building upon the themes introduced in the previous section. It covers the definition of post-disaster response, highlighting its importance and the challenges faced. This is followed by understanding the use of remote sensing data to support damage detection and response assessment and exploring the spatial coverage of existing studies. This chapter also describes the trade-off between spatial and temporal resolution of higher spatial resolution datasets. Followed by ways of integrating different datasets in remote sensing studies, the focus is placed on the extraction of features from satellite data, particularly texture feature extraction. Finally, the chapter explores the application of PlanetScope satellite data in damage detection and response assessment, focusing on its capabilities and limitations.

2.1. Understanding post-disaster response

2.1.1. Definition

Disaster response refers to the actions taken immediately after an event (Figure 4) to save lives, reduce the impact of the event, ensure safety and meet the needs of the impacted population (Tomaszewski et al., 2015). It is an important and challenging phase that focuses on both immediate (relief) and medium-term response continuing for several days or weeks. Immediate response activities include saving lives and providing basic necessities (like food, clothing and shelter) to the affected population (Todd et al., 2011). The medium-term response phase entails ensuring public safety, clean-up operations, assessment of damage, needs assessment, restoration of essential services and communication of relevant public information (Cumbane et al., 2019; National Research Council, 2006). These activities from the response phase also impact the process of recovery, highlighting the importance of their adequate implementation (FEMA, 2016).

Figure 4. The Disaster Management Cycle (Bosher et al., 2021)

2.1.2. Challenges

Based on the location, type, severity and timing of a disaster event, the challenges encountered during the response phase also vary. Oden et al., (2012) identified challenges related to coordination between actors collaborating to undertake the relief operations, curating and disseminating timely information and access to resources and/or information for impacted populations as the main recurring challenges during this phase. Moshtari et al. (2021) studied the relief operations from the 2017 Iran-Iraq earthquake to also find similar challenges in addition to pointing out the reasons behind them. These include complexity in the needs of impacted communities, short time for implementation, limited resources and funding, disruption to infrastructure hindering accessibility and limited capacity of responding authorities.

2.2. Importance of post-disaster damage and response assessment

After a disaster event, it is important to understand the impact of the event and the needs of the community to determine the steps and priorities for response activities. Disaster response assessment provides information on the impact of the disaster on the community, infrastructure and environment helping the stakeholders align their efforts and resources efficiently (Rogova et al., 2006).

Additionally, coordinating and managing the response activities is challenging as the severity and frequency of hazards increase, demanding attention for a proportionally large population. With limited resources, capacities of the responding authorities, short response time and changing dynamics of the post-disaster scenario (Ye et al., 2020), post-disaster response assessment helps to understand the speed and reach of relief operations. Additionally, it also helps to assess the level of coordination among the responding organisations in addition to identifying the gaps to further support preparedness for future events.

2.3. Remote sensing-based methods for post-disaster damage and response assessment

The use of remote sensing to support the different phases of disaster management has become a commonly used approach largely due to the availability of a diverse dataset. The analysis undertaken by academicians and decision-makers using such data has proven to support the different phases of disaster management (Boccardo et al., 2015). For example, rapid damage assessments provided during the emergency response phase by actors like Copernicus EMS, and UNOSAT use very-high-resolution satellite imagery covering the affected area (Cotrufo et al., 2018). Such assessments use change detection to often calculate variations in the features extracted (Table 1) from two or more single or multi-source images (before and after the event). Once the changes are calculated, a threshold is set, or a pattern is identified that corresponds to meaningful changes. This approach has been used in multiple studies (Table 4), for example, Adriano et al., (2019), Syifa et al., (2019) and Virtriana et al., (2023) used multi-source spectral features for damage mapping. Gibson et al., (2023) compared fire extent and severity mapping of Sentinel 1 (radar) and Sentinel 2 (optical) along with GLCM texture metric and found that texture indices increased the performance of classification for both the sensors. Khodaverdizahraee et al., (2020) developed an automated method to detect damage and remove debris from changes in texture and spectral measures of very high-resolution satellite images, where the differences from pre- and post-event images were used as input for classification.

Table 4. RS data supporting post-disaster assessments.

Purpose	Features	RS data	Ancillary data	Machine learning	Reference
Fire extent mapping	Texture	Sentinel 1 and 2 (10 meters resolution)	Precipitation data	SVM	(Gibson et al., 2023)
Damaged assessment (large-scale)	Spectral, texture and shape	Landsat-8, Sentinel-2 and WorldView-2 (panchromatic and multispectral)	Field data (photographs) and reference map from UNITAR for validation	Artificial Neural Networks (ANN), SVM and Semi-automated (OBIA)	(Omarzadeh et al., 2021; Syifa et al., 2019)

Building damage assessment	Spectral (intensity, coherence) and geometry (DEM)	SAR scenes from ALOS-2 PALSAR-2, Sentinel-1, WorldView II	Optical Sentinel-2 and PlanetScope sensors, OpenStreetMap (OSM) building data, Copernicus EMS damaged labels, xDB data	Random Forest, Convolution Neural Networks (CNN)	(Adriano et al., 2019; Valentijn et al., 2020; Virtriana et al., 2023)
Debris removal	Texture, spectral (brightness), shape	QuickBird panchromatic and 8-band multispectral (1.2 meters and 0.8 meters respectively), WorldView II	Built-up data, building damage survey	Genetic Algorithm (GA), ANN, SVM	(Izadi et al., 2017; Khodaverdizahraee et al., 2020; Sonobe, 2020)

2.3.1. Spatial coverage

Although post-disaster response assessments and studies undertaken using the various high-resolution remote sensing data provide detailed information, they often concentrate on specific locations generally due to their limited spatial coverage. This is particularly true when the focus is on settlements or inhabited areas. For instance, studies by Aimaiti et al., (2022), Deng et al., (2022) and Xie et al., (2022) only used images from urban locations to test the damage assessment methods or classification results. Similarly, the rapid assessment done by emergency management organisations also uses these high-resolution datasets to perform damage assessments while only being able to do it for the requested locations depending on the availability of images (Spasenovic et al., 2019), often focusing on densely populated areas while covering regions surrounding those areas (Figure 3). The social and economic vulnerabilities of communities residing in remote locations are worsened due to the impact of catastrophic events. The Global Natural Disaster Assessment Reports of 2020 and 2022 also highlight that rural locations have over 80% of annual casualties due to disasters and recognize the need to reduce their physical exposure to these disasters (IFRC et al., 2021; UNDRR, 2022). One of the main reasons behind this is the limited availability of information which gives rise to several challenges like reduced rescue operations efficiency, ineffective resource allocation and response management efforts (Yang et al., 2024) in remote locations. This highlights the importance of adequate coverage and focus on such settlements and communities, particularly during emergencies.

2.3.2. Temporal resolution

The development and progress in remote sensing systems have enabled the undertaking of desired tasks at different spatial and temporal scales. However, a trade-off generally exists between the spatial and temporal resolution, where fine spatial resolution datasets have relatively coarse temporal resolution that can limit their usage in monitoring frequent and rapid changes (Hosseiny et al., 2022). For example, Szpakowski et al. (2019) in their research covering fire risk mapping highlighted that satellites like Sentinel-2 perform well in detecting fires, but their lower temporal resolution makes them less ideal for monitoring the active fires. Frequent mapping to capture rapidly changing conditions (such as active fires) usually uses moderate (5-30 meters) to lower (over 30 meters) spatial resolution datasets that have higher temporal resolution. However, for the response activities mentioned in Table 2, effective monitoring at any desired location requires high (1-5 meters) and/or very-high (less than 1 meter) spatial resolution datasets having high temporal resolution as well (SatSummit, 2015). Very-high-resolution datasets such as WorldView, and Pleiades technically meet the technical requirements however their limited and inconsistent coverage (Annex 1 and Figure 3) does not support monitoring the dynamic changes that require frequent images of the area of interest.

2.3.3. Data integration

Remote sensing studies often combine multiple data types to get a more comprehensive understanding of the activity in focus. This is observed across all the fields (environmental, urban, disaster etc.) where the interaction of multiple components necessitates the use of different datasets. For instance, Cerbelaud et al., (2021) undertook flood damage detection using high-resolution satellite data with ground truth, contextual information, digital elevation model and land use information as ancillary data. Vizzari (2022) also integrated higher spatial resolution satellite images with Sentinel data to improve the accuracy of object-based image classification. Table 4 also provides several examples where the integration of additional datasets such as building footprints, precipitation data, field surveys, higher resolution satellite images etc. have supported remote sensing analysis. Such datasets complement the spatial analysis from satellite images to provide more comprehensible insights and structured information.

On the other hand, the integration of additional datasets also presents limitations and requires additional computational efforts due to scale differences, completeness of information, varying data quality and so on. For instance, the accuracy and completeness of building footprints made manually or by automation like that in OSM are different from the ones generated by yet another automatic method or algorithm by a different source (Gevaert et al., 2024) (Figure 10). Such a case requires manual checks for completeness followed by transformations to align the digital footprints with actual building footprints. There are also cases where the integration of satellite images of varying scales requires resampling to harmonize them, as was done by Vizzari (2022). Hence, such data integration cases require additional computations and cross-checks to ensure compatibility to utilize their collective functionality.

2.3.4. Feature extraction

Feature extraction is used to represent information by retrieving the unique attributes from a given or acquired dataset (Salau et al., 2019). In the field of remote sensing, it is one of the important steps preceded by image classification. Feature extraction is particularly useful when spectral information alone is not sufficient to support the task (Kumar et al., 2020) or high-dimensional data requires reduction (Li et al., 2022). Several studies illustrate the use of different feature extraction methods, such as local binary patterns for feature extraction to detect slum areas in pre-, immediately after and post-disaster events (Ghaffarian and Emtehani, 2021), recurrent neural networks (RNN) for extracting spatial and temporal information for land use classification (Xu et al., 2021) and convolution neural network (CNN) for extracting road features from satellite images (Abdollahi et al., 2020).

While features based on deep learning approaches like CNN have proven to be more effective than conventional approaches (Vetrivel et al., 2018), this research used Gray-Level Co-Occurrence Matrix (GLCM) for texture feature extraction coupled with a supervised machine learning algorithm for classification purposes. This was done because of limited data and better interpretability of features extracted from GLCM compared to those from CNN which require additional analysis to understand the learned features (Hosseiny et al., 2022). This supports the goal of this exploratory research, gaining insights into PlanetScope data characteristics which can be achieved through easily interpretable features.
Texture analysis has been widely used in the field of remote sensing as its features can provide important information based on the relationship between pixel values in an image. It has been used to support post-disaster assessments such as small (Wei et al., 2020) to large (Lubin et al., 2019) scale damage detection, mapping the extent of the disasters (Gibson et al., 2023; Wei et al., 2020) and monitoring recovery (Ghaffarian and Kerle, 2019; Quan et al., 2020). These studies show that varying texture features have proven to help provide a quantified measure of the changes and describe them by exploring the spatial distribution within the desired area (Zhang et al., 2017). There are multiple methods for texture analysis (Figure 5), however, the GLCM is one of the most recurring methods across several studies in addition to

giving relatively better outcomes compared to other methods. For example, Kupidura (2019) compared the land use/cover classification performance of GLCM (using high-resolution WorldView and Pleiades images) with two other methods, namely Laplace filters and Granulometric analysis and found that GLCM was effective in enhancing the classification. Although GLCM texture measures have high dimensionality (Belgiu & Drăgut, 2016), meaning each data point in the sample set (such as buildings) includes 8 texture variables, they have demonstrated good performance with respect to the computation time and complexity (Heurtier, 2019). Furthermore, with the rise of utilizing machine learning algorithms in the field of remote sensing, large datasets are efficiently handled, thereby mitigating issues related to high-dimensional data handling (Maxwell et al., 2018).

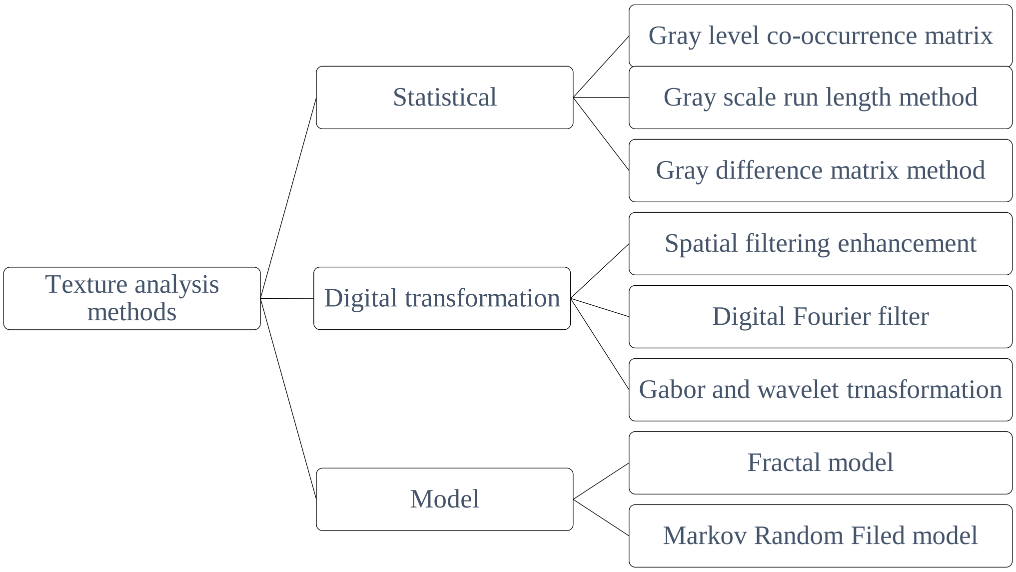

Figure 5. Texture analysis methods (Liu et al., 2021)

GLCM has the following texture measures:

Table 5. Texture measures in GLCM (Hall-Beyer, 2017)

Measure name	Calculation formula
Homogeneity	$\sum_{i,j=0}^{N-1} \left(\frac{p_{i,j}}{(1 + (i - j)^2)}\right)$
Contrast	$\sum_{i,j=0}^{N-1} P_{i,j}(i - j)^2$
Dissimilarity	$\sum_{i,j=0}^{N-1} P_{i,j}\lvert i - j\rvert$
Mean	$\sum_{i,j=0}^{N-1} i(P_{i,j})$
Variance	$\sum_{i,j=0}^{N-1} P_{i,j}\left(j - \mu_j\right)^2$
Entropy	$\sum_{j=0}^{N-1} P_{i,j}(-\ln P_{i,j})$
Angular second moment (ASM)	$\sum_{i,j=0}^{N-1} P_{(i,j)}^2$
Correlation	$\sum_{i,j=0}^{N-1} P_{i,j}[\frac{\left((i - \mu_i)(j - \mu_j)\right)}{\sqrt{(\sigma_i^2)(\sigma_j^2)}]}$

In the equations from Table 5, i and j Digital Number (DN) values are labels of the columns and rows (respectively) of the GLCM. $P_{i,j}$ are the probability values within the window for the adjacent pixels. μ is the mean and σ the standard deviation.

For GLCM analysis, a window size is selected and used on small sub-regions of the image to analyze the texture. The size is selected based on the spatial resolution of the image and the scale of the texture to be analyzed (Hall-Beyer, 2017). This is followed by deciding the direction and distance in which the relationship between pixels is to be examined. Based on these, the different combination of pixel values is calculated within the window and measures like contrast, dissimilarity, homogeneity, energy etc. are calculated, which provide a quantitative measure of texture. Table 4 shows that multiple studies use texture-based analysis in the field of post-disaster response, majorly to classify damaged buildings and the debris removal process. For instance, the study by Liu et al., (2023) found that homogeneity, energy, and entropy can be used to effectively distinguish collapsed buildings from non-collapsed ones compared to other texture methods like Local Binary Pattern (LBP), Gabour feature etc. Using the dissimilarity measure from GLCM, Sonobe (2020) also mapped collapsed buildings along with locations of debris removal to understand recovery from the 2016 Kumamoto earthquakes that occurred in Japan.

2.3.5. PlanetScope for post-disaster damage and response assessment

With its high temporal and spatial resolution, PlanetScope offers significant potential to support post-disaster damage mapping within a day if the weather conditions are favourable (Adriano et al., 2021). Several studies have successfully used PlanetScope images to perform large-scale damage assessments. For example, Cho et al., (2023) and Hamilton et al., (2023) demonstrated the usefulness of mapping large fires and Blanco (2022) developed an index based on spatial autocorrelation to measure the degree of damage using PS images for Typhoon Rai/Odette (2021) which hit the southern parts of the Philippines. Some studies have also focused on combining PlanetScope with various other remote sensing data sources, leveraging the most useful features of each. For example, Fotiou et al., (2023) used PlanetScope (optical) with Sentinel 1 and 2 (SAR) for impact assessment by understanding co-seismic change and ground subsidence along faults respectively. They found that such a methodology facilitates monitoring of seismic activities thereby improving preparedness and reducing potential risks associated with such events. Kussul et al., (2024) also studied the capability of PlanetScope in identifying artillery craters post-war in agricultural fields and successfully identified the ones with sizes greater than 50 m^2 in addition to tracking the development of the identified craters over time because of PlanetScope's high temporal resolution.

Given the high spatial and temporal resolution and large spatial coverage, existing studies only cover damage assessments with PlanetScope. Post-disaster response phase consists of several other dynamic activities that can be directly or indirectly observed from satellite images such as debris removal, temporary shelter evolution and restoration of infrastructure like road networks. PlanetScope's capability in detecting and monitoring such activities remains largely underexplored.

However, some properties of PlanetScope also pose a challenge to their efficient use as highlighted by Roy et al., (2021) such as the difference between consecutive overpasses varies due to different sensor orbits (Figure 8) and seasonal altitude changes, unavailability of images due to high cloud cover or featureless terrain, different acquisition angles by different sensors and more pronounced shadows by objects like trees or buildings if the image is acquired earlier in the day when the sun is lower in the sky. Several studies have also supported the presence of pixel-based radiometric inconsistencies (Francini et al., 2020), illumination differences between images from different dates (Blanco, 2022), limitations in its geometric accuracies (Schaeffer et al., 2022) and inconsistency in revisit time that impact the accuracy of models used for change analysis (Wang et al., 2022). Figure 7 also illustrates these differences for one of the areas being focused on in this research.
Considering PlanetScope's advantages like high temporal resolution and spatial coverage alongside the limitations mentioned and illustrated above, it becomes imperative to evaluate its utility in supporting post-disaster response assessment.

3. STUDY AREA AND DATASET

Following the review of the literature, this chapter focuses on the context of the Türkiye-Syria earthquakes that occurred in February 2023, which is selected as the case study for the research. This section outlines the study area and lists the datasets used, primarily consisting of satellite images.

3.1. Study area

Türkiye is a transcontinental country, situated partly in Asia and Europe. Due to its location and geomorphological structure, Türkiye is prone to natural hazards such as earthquakes, landslides, floods and wildfires. Most of the country is located at the intersection of three tectonic plates, the Eurasian, African and Arabian (Figure 6) making it highly susceptible to earthquakes. Alpyürür et al., (2022) utilized data from the Kandilli Observatory and Earthquake Research Institute of Bogazici University and found that 23 earthquakes of magnitude more than 6 occurred in the southwestern part of the country alone from 1900 to 2020.

On 6th February 2023, south-eastern Türkiye and northern Syria were hit by 7.8 and 7.5 magnitude earthquakes (also known as Kahramanmaraş earthquakes) on the same day. Major aftershocks followed the earthquake, such as the 6.4 magnitude on 20th February and another 5.8 magnitude in the region, amounting to a total of 14,107 aftershocks as of March 5, 2023 (Kelani et al., 2024). The provinces of Kahramanmaras, Hatay, Gaziantep and Adiyaman were most affected in Türkiye in addition to Idlib, Aleppo and the coastal regions of Latakia and Tartus from Syria. According to a recovery and reconstruction assessment report by the Turkish Government, total fatalities (as of the end of March) were close to 48,000 with 3.3 million displaced people and approximately 2 million living in tent camps and container settlements (Government of Türkiye, 2023).

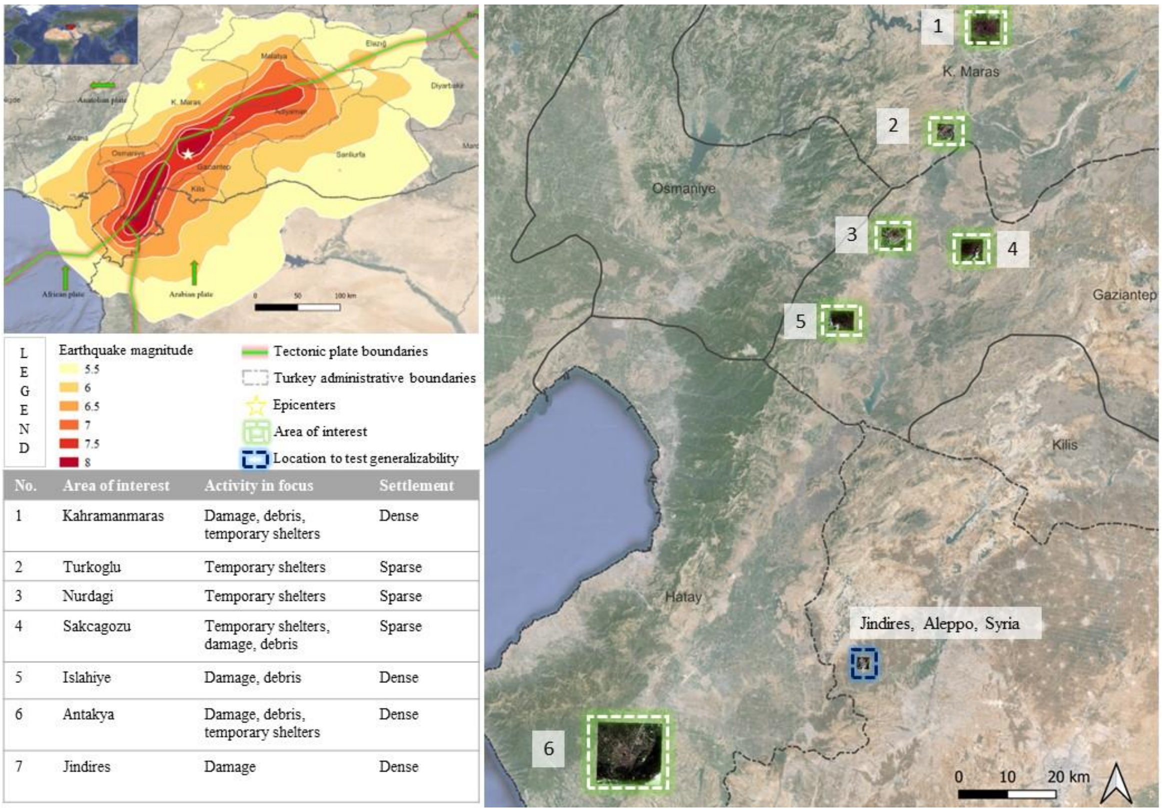

No.	Area of interest	Activity in focus	Settlement
1	Kahramanmaras	Damage, debris, temporary shelters	Dense
2	Turkoglu	Temporary shelters	Sparse
3	Nurdagi	Temporary shelters	Sparse
4	Sakcagozu	Temporary shelters, damage, debris	Sparse
5	Islahiye	Damage, debris	Dense
6	Antakya	Damage, debris, temporary shelters	Dense
7	Jindires	Damage	Dense

Figure 6. Study area

In the region where the earthquakes occurred are also some provinces that have a below-average income of Türkiye, in addition to more than a million Syrian refugees (approximately 50% of the total Syrian refugee population in Türkiye) (The World Bank and GFDRR, 2023). This research will focus on such border provinces (densely and sparsely populated) close to the earthquake epicentre from Türkiye, specifically Kahramanmaras (AOI 1), Turkoglu (AOI 2), Nurdagi (AOI 3), Sakcagozu (AOI 4), Islahiye (AOI 5) and Antakya (AOI 6) which will be referred to as the area of interest (AOI) in this research (Figure 6). While the focus should also be on the regions affected by the earthquake in Syria amid pre-existing war/conflict, due to the limited availability of higher resolution images and required spatial information to support processes like labelling, only regions of Türkiye have been used in this research. These study locations were selected based on the availability of corresponding higher-resolution satellite images (WorldView and Pleiades) and damage assessments (Copernicus EMS and/or UNOSAT). Jindires (Aleppo) from Syria (AOI 7) was selected to check the generalisation of the damage detection model trained and tested on data from Türkiye. This location was chosen due to the availability of damage assessment (used for validation) by UNOSAT.

3.2. Data used

The main data used in this research were PlanetScope satellite images. They were acquired through Planet Lab's Education and Research Program, which allows limited, non-commercial access of up to 5,000 km^2 of data monthly for one year. Higher-resolution satellite images were also used to support the analysis- WorldView and Pleiades. The WorldView images were acquired through Maxar's Open Data Program, which provides free access to available before and after-event satellite images. The Pleiades images were acquired through Airbus's Education and Research Programme. Through this programme, accepted student projects get access to 100 km^2 of data. In Table 6, an overview of the data files, their sources, ownership, restrictions or licence, form and formats is provided. Satellite images available for February and early March 2023 from the sources mentioned in the table below were used in this research. Refer to Appendix 1 for information on spatial and temporal resolution of the image sources.

Table 6. Secondary data used

Dataset	Owner of data	No. of images	Restrictions and licence	Data form	Format
PlanetScope Satellite images	Planet (2023)	86	Yes, limited access via education and research access	Raster	GeoTiff
WorldView Satellite images	MAXAR (2023)	09	Yes, limited access via open humanitarian data access	Raster	GeoTiff
Pleiades Satellite images	Airbus (2023)	06	Yes, limited access via the student account	Raster	GeoTiff
Copernicus EMS and Microsoft's Damage assessments	Copernicus EMS, Microsoft AI for Good (2023)	NA	No restrictions, open	Vector and reports	Shapefile, text
Built-up, land use land cover from AOI	OSM (2023)	NA	No restrictions, open	Vector	Shapefile

The main dataset for this study consists of PlanetScope images, Table 7 shows the number of images acquired for the different locations. The locations were selected based on the post-disaster activities in focus, the availability of higher-resolution WorldView images and existing damage assessments from the selected locations. The research utilized available WorldView images from the locations mentioned in Table 7 and available Pleiades images from Hatay (1 image) and Nurdagi (3 images).

Table 7. PlanetScope images from areas of interest

Country	AOI	WorldView image availability (post-event*)	Area covered PS (km²)	Month and date ranges (PS)						Total images (PS)
				February				March		
				01-05	06-13	14-20	20-28	01-07	08-14	
Türkiye	Kahramanmaras	1	37.7	1	3	3	5	1	2	15
	Hatay	1, incomplete coverage due to missing image	163.5	1	4	4	3	3	1	16
	Islahiye	2	20	1	3	2	5	1	1	13
	Nurdagi	2, incomplete coverage due to cloud cover	10	1	4	5	4	1	3	18
	Sakcagoz	NA	6	1	3	3	4	1	2	14
	Turkoglu	1, incomplete coverage due to cloud cover	10	1	1	4	3	0	1	10
Syria	Jindires	NA	7	1	1	-	-	-	-	2
		Total images								88

* No pre-event WorldView images available from AOIs. All post-event images are either from 7th or 8th February (immediately after the earthquake).

In summary, this chapter shows that the majority of study regions were selected from Türkiye, with one region from Syria due to the limited availability of ground truth and corresponding higher-resolution satellite images. This case study also illustrates the application of previously discussed data integration and sheds light on the challenges of conducting damage detection and response assessments in areas with limited data access.

Ethical consideration

This research focused on non-human subjects observed in satellite images, ensuring that no direct sensitive or private information related to any individuals was retrieved or shared. The primary aim was to assess PlanetScope's capability in supporting post-disaster response and damage assessment, strictly utilizing only the necessary images for analysis. The study followed the ethical standards by ensuring no data fabrication occurred and that all inferences drawn were justified.

The following section will detail the methodology employed for this study.

4. METHODOLOGY

Following a brief introduction of the study area and the data being used in this research, this section explains the methodology employed to address the research questions. This includes pre-processing steps, labelling approaches for damage, debris and temporary shelters, texture feature extraction with supervised machine learning for classification and how higher resolution data was integrated with PS in this research.

4.1. Data preparation

4.1.1. Pre-processing satellite images

For this research, PS images with a cloud cover of less than 15 % for the selected areas of interest were downloaded using the interface provided under the program. The PS images are deemed analysis-ready as they have already undergone atmospheric, radiometric, and geometric corrections. However, further radiometric normalization and geometric corrections were performed to reduce the differences observed due to misalignment and illumination differences between images from different timestamps of the same scene (Figure 7).

Radiometric normalization is used to remove the effects caused due to different sensors (Figure 8 a), sun illumination and atmospheric conditions (Figure 8 b) to make a comparison of multi or hyper-temporal images better (Santra et al., 2019).

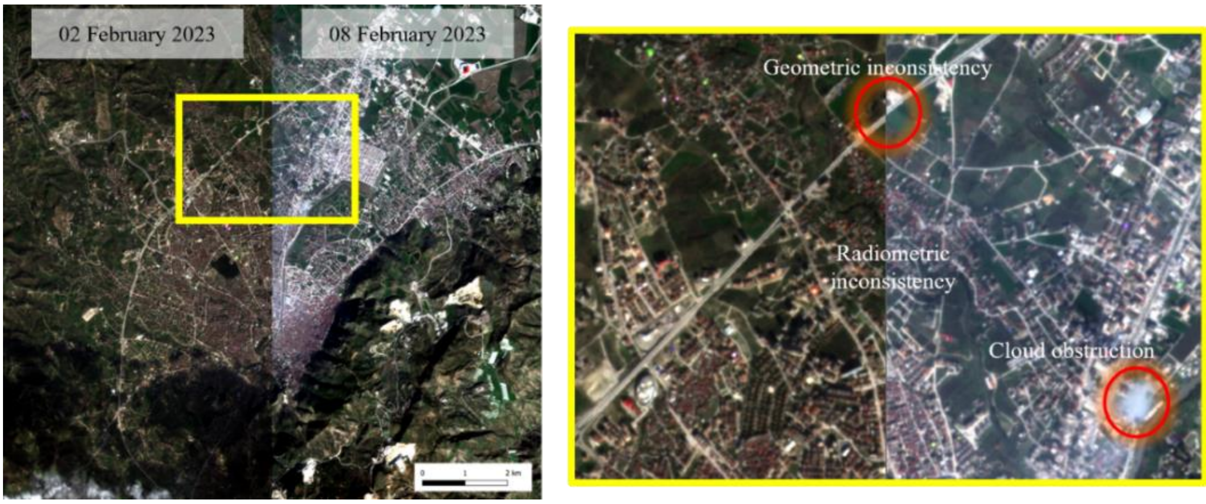

Figure 7. Geometric inconsistencies between PlanetScope images from Antakya (AOI 6) captured on the 2nd and 8th of February 2023.

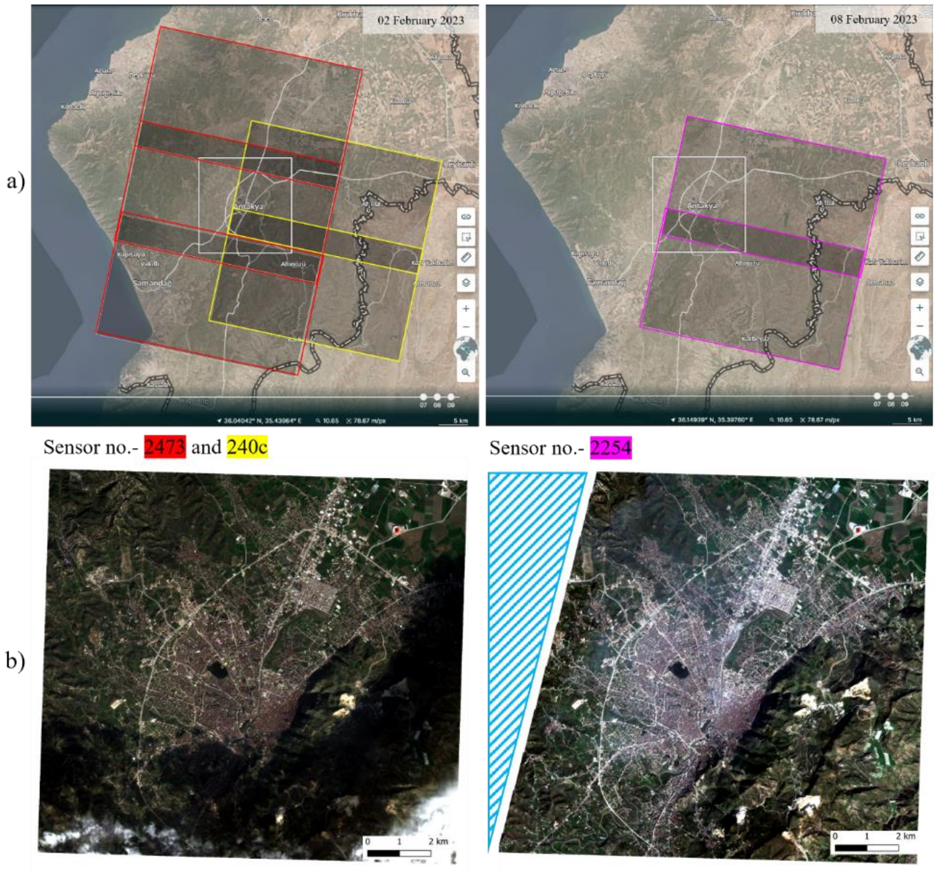

Figure 8. Radiometric inconsistencies between PlanetScope images from Antakya (AOI 6) captured on the 2nd and 8th of February 2023.

The acquired images were radiometrically normalized (relative) through histogram matching. The pixel values for the input images were adjusted to match the histogram of the pixel values of a reference image to achieve a similar radiometric appearance. Further, geometric correction was performed to ensure better alignment of the images from the same scene. This was done using ERDAS Imagine software, where ground control points (GCP) are generated by identifying stable features in the scene such as road intersections. The software also provides an option to generate the GCPs automatically. While using this approach, it was ensured that only the GCPs with the least error (less than 0.4) were selected. These points were used to improve the alignment of the images from each area of interest.

4.1.2. Labelling

Supervised machine learning was used for classification which required a labelled dataset. Due to the absence of a pre-existing labelled dataset, labelling was first done manually based on direct observations from PS images. Higher-resolution images were used later to confirm damaged buildings and response activities being studied in this research: evolution of temporary shelters (the presence of temporary shelters) and debris (debris collection sites), which are discussed in detail in section 4.7. Additionally, damage assessments for the event done by Copernicus EMS and Microsoft were also used to support the task in situations where the reliability of WorldView images was limited due to reasons like spatial coverage, cloud obstruction and the presence of other artefacts within the images. Labelling was done for the following-

- Damage - binary classification with ‘observable damaged’ and ‘no observable damage’ labels (Figures 9 a and b).

- Debris - multiclass with 'present', 'absent' (Figures 9 a and b) and 'debris disposal locations' (Figure 9 c) labels.
- Temporary shelters (Figure 9 d and e)- multiclass with 'present', 'absent', 'removed' (Figure 9 d) and 'presence of/transition to semi-permanent settlements' (Figure 9 e) labels.

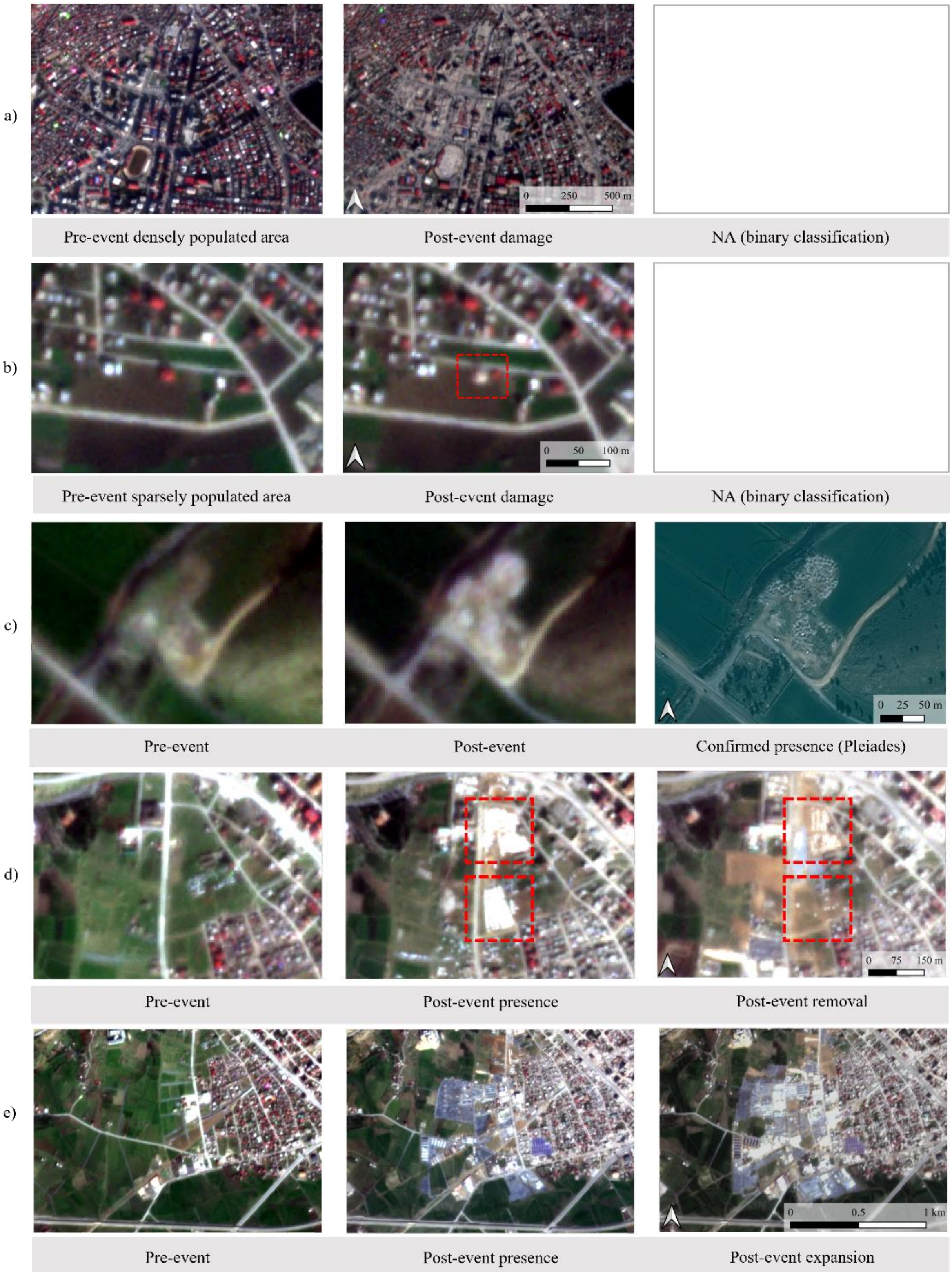

Figure 9. Examples from AOIs (Türkiye) show- (a) observed collapse of buildings and presence of debris in densely populated areas, (b) observed collapse of buildings and presence of debris in sparsely populated areas, (c) debris disposal site, (d) presence and removal of temporary shelters and (e) expansion of container settlements.

Table 8 describes the four types of labelling we explored. For the classification of damage and debris, building footprints were initially used as labels (Table 8 a). However, for the identification of temporary shelters, the focus was on areas beyond these footprints. This is because the temporary shelters were built on available open spaces, which included not only parks and stadiums but also available peripheral zones surrounding the towns, villages, road roundabouts, farmland and buildings, as can be observed in Figure 9 (d). This distribution posed limitations in quick delineation or segmentation of the image for monitoring temporary shelters. Therefore, a grid-based approach was adopted where grids representing non-built-up areas were used for labelling temporary shelters. This grid-based approach was subsequently also applied to the classification of damage and debris focusing on grids representing built-up areas (explained further in section 5.1).

This research focused on creating a balanced dataset for the classification of activities. For binary classification in the case of damage detection, this was done by adjusting the dataset to have an equal number of samples from both minority (1) and majority (0) classes by under-sampling the majority class (Verschoor, 2022). For a multi-class dataset, a similar approach was followed where the minority classes had significantly fewer number of samples than the majority class. The dataset was first adjusted by under-sampling the majority class to have the same number of samples as the samples of all minority classes combined. Further, due to classes such as 'debris collection site' having a lesser number of samples (within the minority classes), a weighted approach was introduced (Zhou et al., 2023). In this approach, weights were assigned to each minority class during classification proportional to its class frequency in the dataset to ensure a balanced representation of all classes.

4.1.2.1. Building Footprint

Figure 10 shows the coverage and completeness of available building footprint data from the selected area of interest. The information was extracted from OSM and Microsoft Building Footprints. It can be seen that both footprints do not align with the actual building footprint and OSM footprint has omitted some buildings. To address the issue of alignment, an affine transformation was applied on both footprints to shift them by specifying a distance in the X and Y directions in QGIS (Figure 10). Further, to address the issue of completeness, only the missing footprints in OSM were merged from the Microsoft building footprint data to create a complete dataset. OSM was selected as the primary dataset to represent the building information as it was better aligned to the actual footprint after transformation compared to Microsoft building footprints.

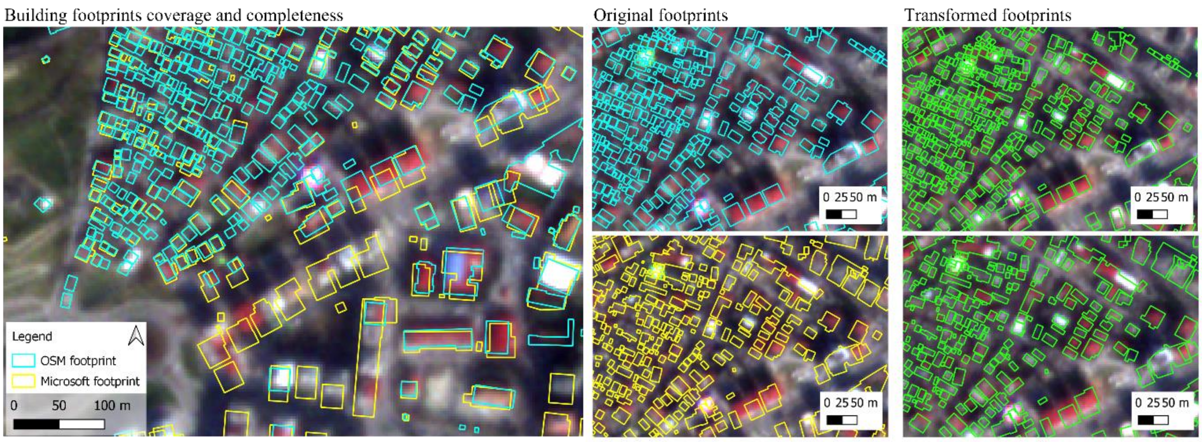

Figure 10. Comparison of building footprints from OSM and Microsoft and transformation overlayed on PS images

4.1.2.2. Grid

Table 8 (b and c) shows the grid representing the area of interest that was generated for labelling. During the labelling process for damage detection, it was noted that a single grid unit can contain parts of several building footprints. The labelling in this case was done by assigning the labels to each grid based on spatial correspondence with the labelled building footprint layer in QGIS. The label assigned to it corresponded to the highest value (1=damaged building) taken from the associated building footprints.

Table 8. Building footprint and grid-based approach used for damage labelling on PS images.

	Labeling unit	Building footprint used	PlanetScope images		Label assigned	Difficulty and uncertainty in labeling
			Pre-event	Post-event		
(a)	Building footprint	Yes	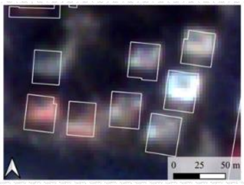	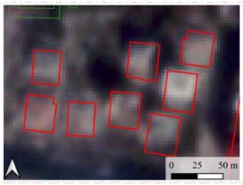	One label per building, provided example shows buildings labelled as 'damaged'	High difficulty when: • the building size is small, • The damage is not evident (absence of roof, presence of debris).
(b)	Building footprint and grid (800 m²)	Yes	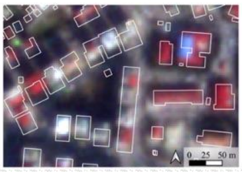	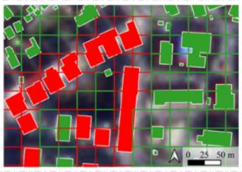	The label of the building, provided to overlapping grid unit. However, if the grid contains both 'damaged' and 'not damaged' building, it is still given the label of 'damaged'	Moderate difficulty. Cases of high uncertainty when grid contains more 'not damaged' building(s) than 'damaged' building(s) (or part of building).
(c)	Grid (800 m²)	No		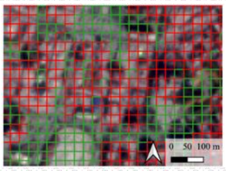	Grid unit with visible damage is labelled as 'damaged' and the grid with no visible damage is labelled as 'not damaged'	High difficulty. Visual inspection of each grid unit is subjective and may lead to inconsistencies. Distinguishing between damage and other artifacts (e.g., shadows) is challenging.
(d)	Grid (500 m²)	No	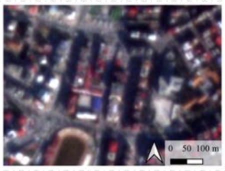	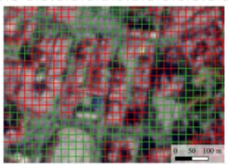	Grid unit with visible damage is labelled as 'damaged' and the grid with no visible damage is labelled as 'not damaged'	Moderate difficulty. While smaller grid-size may reduce ambiguity, challenges stated above persist.

This was followed by a visual check and required rectifications to ensure the correct representation of classes for each grid. The selection of grid size for each area of interest is explained in section 5.1.1. A similar approach was followed for labelling the response activities- the evolution of temporary shelters and debris. Grids representing the different classes for each response activity were labelled manually. Higher-resolution images were also used to validate the presence of response activities.

4.2. Texture feature extraction with Gray-Level Co-Occurance Matrix

Gray-Level Co-Occurrence Matrix (GLCM) was used for texture analysis in this research. GLCM provides eight texture measures, namely angular second momentum (ASM), contrast, correlation, dissimilarity, entropy, homogeneity, mean and variance that were calculated for all the PlanetScope images. These texture measures are calculated in predefined directions for pairs of gray-pixels in the image (Christaki et al., 2022), as shown in Table 9 using a window size of 3 by 3. A small window size was selected to extract clear and detailed information because increasing window size results in relatively less sharp and coarser texture features (Cao et al., 2019). However, Kim et al. (2023) found that the different window sizes do not significantly impact the change detection performance.

Table 9. GLCM directions (Batista et al., 2010)

Direction	Description
(0, 1)	Immediate neighbour below, vertical comparison
(1, -1)	Immediate diagonal neighbour, bottom-right
(1, 0)	Immediate right neighbour, horizontal comparison
(1, 1)	Immediate diagonal neighbour, top right

The 8 texture measures (Table 5) were calculated for each image (at least one pre-event and multiple post-event images) from every area of interest followed by extraction of texture measures for specific activities in focus- damage, debris removal and temporary shelters in this research. Image differencing was used to quantify changes in temporal analysis as has been done in various studies such as for identifying urban development (Luo et al., 2018), collapsed buildings (Erdogan et al., 2019) and landslides (Muhammad et al., 2022). After calculating the difference of each available consecutive timestamp (Figures 11 and 12), each texture measure was extracted for each segment (building footprint/grid) followed by the calculation of the mean for the segments to summarize the texture information for each unit. These values along with their respective labels for damage, debris and temporary shelters were compiled to create the dataset for classification through a machine-learning model.

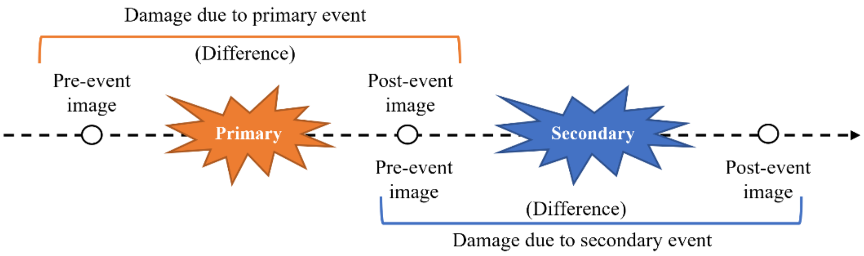

Figure 11. Time for damage detection

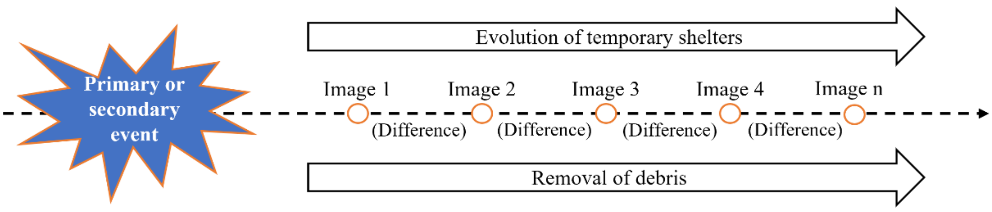

Figure 12. Timeline for changes in debris and temporary shelters

4.3. Supervised machine learning algorithm: Random Forest

Random forest algorithm was used in this research for classification purposes which randomly selects a subset of training samples to produce multiple decision trees that form the basis for classification (Belgiu & Drăgut, 2016). Random forest models have been used in multiple studies in the field of post-disaster assessments to support for example recovery monitoring (Ghaffarian et al., 2020), detection of collapsed buildings (Ji et al., 2019) and flood damage assessment (Tavus et al., 2022). The model's ability to successfully handle data with high dimensionality, multicollinearity and ability to be less affected by noise and outliers (Mei et al., 2019), along with providing variable importance (Kupidura, 2019) made it the preferred model for this research. An additional reason behind selecting the Random Forest model in this research is because of its ability to handle binary, multiclass, categorical or numerical outputs without requiring significant modifications to the algorithm.

The data were divided into training and testing sets, with 80% allocated for training and 20 % for testing. To find the best configuration of the model to maximize its effectiveness, hyperparameter optimization through grid search was performed in this research. This involves searching through a subset of data, evaluating the performance of the different combinations of parameters and selecting the combination that gives the best performance metrics. Hyperparameter tuning also helps in addressing overfitting or underfitting (Huang et al., 2023). The parameters used in this research were (Pal, 2005; Shi and Yang, 2016):

- The number of decision trees,
- The maximum depth of the trees,
- The minimum number of samples needed to split a node,
- The minimum number of samples at each leaf,
- The minimum number of features for the best split and,
- Bootstrap to introduce randomness into the model.

The model also checked for the features that contribute most significantly to its performance through feature selection (Zhang et al., 2017). This was done by analysing the cumulative feature importance based on a set threshold of 95%. Once this subset of features was selected, the model was trained again on the filtered dataset by focusing on the most informative features.

4.4. Validation

The model's performance for classification was checked using the evaluation metric containing accuracy, precision, recall, F1 score, confusion matrix and the area under the Receiver Operating Characteristic curve (ROC AUC) (Table 10). These are calculated as follows, where TP, TN, FP and FN refer to true positives, true negatives, false positives and false negatives respectively:

Table 10. Evaluation metrics and their formulas for classification performance (Shafique et al., 2022)

Evaluation metric	Formula
Precision	TP / (TP + FP)
Recall	TP / (TP + FN)
F1 score	2 * (Precision * Recall) / (Precision + Recall)
Accuracy	Correct Predictions / Total Predictions = (TP + TN) / (TP + TN + FP + FN)
ROC AUC	TP rate = TP / (TP + FN) and FP rate = FP / (FP + TN)

The precision score shows the total true predictions out of all the positive predictions made by the model. Recall measures the total true predictions out of all the predictions, for example, actual damaged buildings that were correctly identified by the model. The F1 score is the harmonic mean of precision and recall. Accuracy measures the number of correctly classified true positives and negatives; it provides an overall measure of the model's performance. ROC AUC is another performance measure that plots the TP rate against the FP rate, where the AUC value ranges from 0 to 1. A higher AUC value indicates better performance and should ideally be greater than 0.7 (Yang et al., 2021), annex 2 provides the interpretation of different ROC AUC values. Confusion matrices were generated to measure the performance of classification which shows the number of correct and incorrect predictions made per class. The classification results were also compared with ground truth data using WorldView and Pleiades images to evaluate the accuracy.

4.5. Quantification

4.5.1. Damage

Kernel Density Estimation (KDE) is a non-parametric method used to derive a continuous surface from an underlying unknown density function (Shuo et al., 2021). It has been used in several studies to convert point-based information to grid-based distributions for analysis, such as wildfire occurrence distribution (Shuo et al., 2021), housing and urban development (Fleming et al., 2017), assessing dynamics at forest edges (Wang et al., 2020) and identifying road accidents hotspots (Le et al., 2022; Loo et al., 2011; Thakali et al., 2015).

KDE first overlays a rectangular grid on the area of interest. A kernel is then used to calculate the density estimate of each grid cell, which is a function of specified shape and width. Equation 1 shows how KDE is calculated, where f(x, y) is the density estimate at location (x,y), n is the number of samples, h is the search radius (bandwidth or kernel size), d_i is the distance between the location (x,y), and the i_{th} observation (data point) and K is the kernel function.

Equation 1. Kernel Density Estimation (Kazmi et al., 2022)

$$f(x,y) = \frac{1}{nh^2} \sum_{i=1} K\left(\frac{d_i}{h}\right)$$

In this research, the 'Heatmap' tool offered by QGIS was used to calculate the mean and standard deviation of KDE values to identify and highlight damage hotpots (based on classification results with feature selection). KDE generates a raster map, to display the intensity and severity of damage as continuous surfaces. The level of damage intensity in different regions is then visually represented by using different colour codes.

Since this research explores a grid-based approach for damage detection, KDE aligns with its methodology as it also focuses on the visualization of data over defined grid cells. Several studies further highlight the benefits of adopting KDE. For example, a study by Wang et al. (2024) shows that KDE can handle spatial heterogeneity by adapting to the changes in density of the data. This makes them suitable for studies focusing on varying degrees of spatial concentration, as expected from a damage pattern after a disaster event. Kazmi et al. (2022) using KDE for road accident hotspot identification show its utility in creating informative and intuitive maps, which can also help identify damage zones in disaster-affected areas of interest.

4.5.2. Response

4.5.2.1. Temporary Shelters

Although the number of shelters constructed or removed was difficult to quantify with PS images alone due to their limited spatial resolution, the rate of expansion of the temporary shelters (particularly container settlements) was analyzed with the hyper-temporal images from Nurdagi (AOI 3). Since the classification of temporary shelters was also done using the grid-based approach, the number of grids covered by container settlements were counted from the collected images from successive dates. Using this count and the area of a grid unit, the cumulative area covered by the shelters along with their rate of expansion was calculated, which was measured in square meters per day (m^2/day). Calculation of settlement growth rates is common in studies that focus on quantifying and comparing the presence and expansion of informal settlements (Samper et al., 2020), densification of such settlements (Mudau et al., 2022) and land cover changes due to refugee settlement expansion (Friedrich et al., 2020).

4.5.2.2. Debris

Various remote sensing data sources can be used to provide information supporting the effective management of rubble and debris after a disaster-event. Numerous studies have shown this. For example, Axel et al. (2016) quantified road debris post-disaster using 3D data provided by point cloud lidar systems.

Saffarzadeh et al. (2017) state the reliability of using UAVs for capturing high-resolution images from the area of interest on desired dates to measure the amount of post-earthquake waste. Pollino et al. (2020) found the utility of very-high-resolution WorldView satellite images in identifying the distribution of different seismic rubble and its sensor's ability to capture the areas from different angles which allows for monitoring the volume of debris. While such datasets are expensive, which may pose limitations to their practical utility, these studies highlight the importance of very high-resolution data and its availability for any area of interest to identify and quantify post-disaster debris. PS images allow monitoring any region at any time (unless hindered by clouds and other artefacts) due to their high temporal resolution and spatial coverage, their spatial resolution and image acquisition at-nadir make them unsuitable for debris quantification tasks. However, KDE as explained in the previous section can also be used to identify the hotspots of debris in the scene that can help emergency responders to plan and prioritize their cleanup efforts. Since the KDE analysis for damage and debris produces similar heatmaps, each showing hotspots of damage and debris respectively, to avoid redundancy, only the quantification of damage is detailed in the results section.

4.6. Assessing generalizability

Generalizability is defined as the model's capability to perform well on data that it different from its training data (Gohil et al., 2024). It helps various users to address different tasks using the same process with similar features, having variation only in the user-provided training labels (Rolf et al., 2021). Several studies on change detection focus on the generalization of classification models. For example, Zhu et al. (2022) validated the generalization performance of their land use land cover change detection model using a larger dataset to improve the model's generalization capability. Pyo et al. (2022) focused on enhancing the generalizability of their forest change detection using open-source satellite images and the U-Net model. Du et al. (2024) proposed a supervised approach to improve the generalization of change detection models across different domains.

The complexity arising from the use of different remote sensing data sources, variations in geographies and spatial arrangement in built-up areas, and the selection of training data can challenge a model's generalization ability (Lunga et al., 2021). As highlighted in section 3, due to the limited availability of ground truth (corresponding higher-resolution images) from Syria, this research focuses on Türkiye's earthquake-affected regions. However, Jindires (Figure 13 a) from Syria was selected to test the generalization of the damage detection model trained and tested on data from Türkiye (Figure 13 b and c).

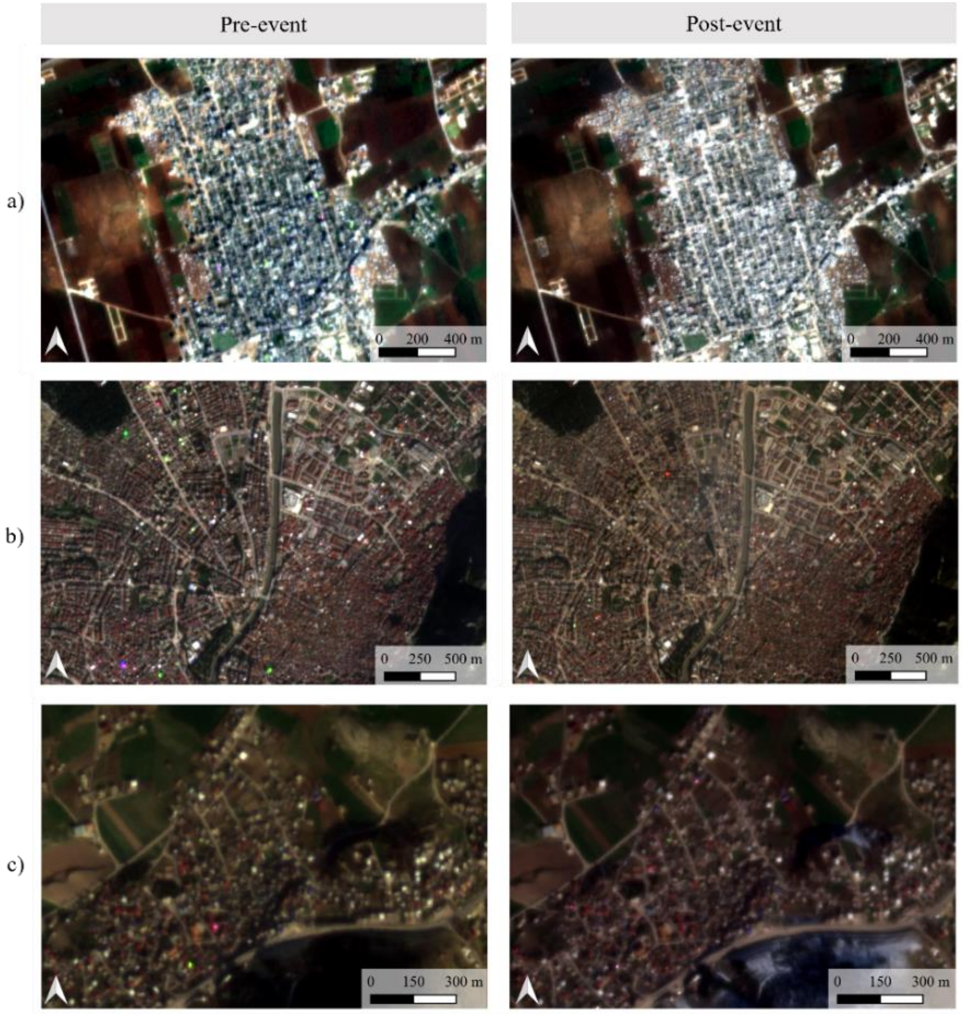

Figure 13. Visual comparison of the settlement patterns between the selected study areas used to test the generalization of the damage detection model (a) Jindires in Syria (AOI 7), (b) Antakya (AOI 6) and (c) Sakcagozu (AOI 4) representing examples of densely and sparsely populated areas respectively from Türkiye.

The documented post-disaster response to this earthquake event showed that Türkiye had a better and stronger response with more international attention (Uwishema, 2023) while Syria, already suffering from pre-existing conflict, received comparatively less international attention (Patwary et al., 2023). This difference in coverage was also evident in the satellite images made available for free by Maxar under its Open Data Program, which majorly covered areas from Türkiye, with only one image covering a region neighbouring Azaz city in Syria. Assessing the generalizability of the model allows to evaluate the model's applicability in a different geographical area beyond the initial study area and check whether the methodology and model could be directly applied to the neighbouring region also impacted by the earthquake. This helps to check if the developed methodology and/or model is versatile and can be used to provide valuable insights in regions with varying levels of satellite coverage, international attention and general information availability.

4.7. Data integration

The higher resolution WorldView and Pleiades images were integrated at various steps in the research in ways explained below:

1. Ground truth- - Initially, the labelling was done from direct observations from PS images. Also, the texture analysis used for the detection of damage, debris and temporary shelters (including transitions) was done on the PS images only. Separately from the labelling and texture analysis on

PS, the available higher-resolution images were used to validate and confirm the reliability and effectiveness of the labelling and texture analysis.

2. Confirming the presence of activity- As shown in Figure 14, confirming the presence of certain dynamic activities like debris collection sites or shelters was sometimes difficult with PS images alone, due to reasons like similar appearance with objects in the vicinity or unclarity due to resolution. In such cases, available higher-resolution images were used to confirm the presence for labelling. The available time-series images from PlanetScope were further used to understand the transition of the identified dynamic activities.

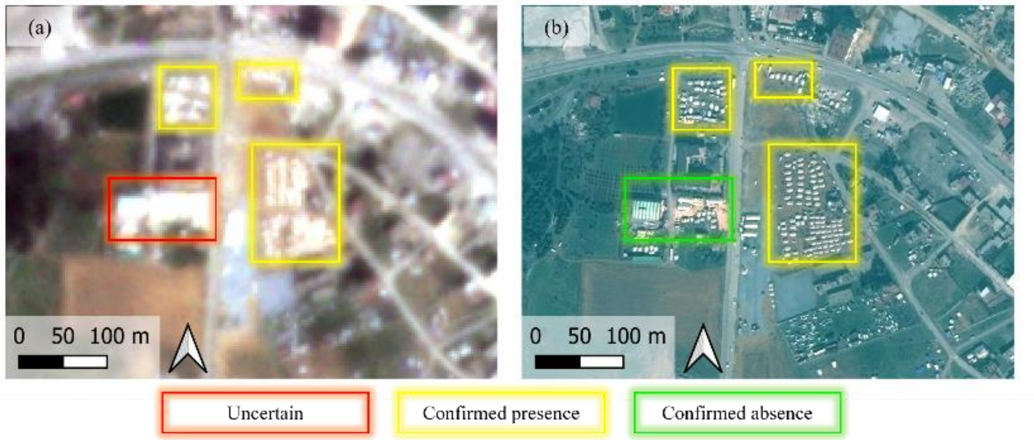

Figure 14. Understanding the presence of temporary shelters from (a) PlanetScope and (b) Pleiades image

3. Data integration- With the limited availability of higher resolution images (maximum two images from different dates for the AOIs), undertaking a detailed and comprehensive pixel-level integration for all PS images was not attainable. However, a focused image sharpening test was conducted to check the feasibility of incorporating higher-resolution Pleiades image with PS images. Such very high-resolution images are not freely available and for this research were accessed through Airbus's education and research programme. A high-pass modulation method (Li et al., 2020) was followed for sharpening each individual band (red, green and blue) image of PS with the corresponding individual band image from Pleiades. In this method, the higher-resolution image (Pleiades) is first down-sampled to match the resolution of PS image. The down-sampled image is then subtracted from the original higher-resolution image to create a 'high-pass' image. This high-pass image is blended with the lower-resolution PlanetScope image by adding it with a blending or modulation factor (Equation 2). This modulation factor determines the strength/intensity of information being added from the high-pass image. The blending/modulating factors of 0.2, 0.5 and 1 were tested. This test was conducted with PlanetScope and Pleiades images from 01 and 02 March 2023 respectively (approximately a month after the event) from Nurdagi (AOI 3- sparsely populated area). Pleiades images from 08 and 09 February were also available but were not considered due to high illumination difference and cloud cover.

The quality assessment of sharpened images was done by comparing the edges of the original and sharpened images using the Canny algorithm, which is one of the most popular traditional algorithms for edge detection (Chen et al., 2024). It is simple to understand analytically, commonly available in different software libraries and computationally efficient (Abraham et al., 2021). The 'cv2.Canny' function from the OpenCV library was used which identifies the edges by looking for areas of rapid intensity change (OpenCV, 2024). The number of edge pixels were calculated using this method and compared with the original and sharpened images to measure the effect of sharpening process. An increase in the number of edges indicates enhanced details (Abraham et al., 2021).

Equation 2. High-pass modulation method for sharpening PS image using higher-resolution Pleiades image

$$\underbrace{\text{Original} - \text{Down sampled}}_{\text{Pleiades image}} = [(\text{High pass image}) * \text{modulation factor}] + \text{PS image}$$

In summary, our methodology consists of using GLCM to extract texture features from PS images. Both building footprint and grid-based approaches were used for the classification of damage, while only the grid-based approach was used for the classification of response activities in focus. A supervised machine learning algorithm, Random Forest, was selected for classification purposes. Available higher-resolution satellite images were also integrated in various ways to illustrate their synergistic potential with PS data to support the analysis.
The following section presents the key results and key findings of the study.

5. RESULTS

In this chapter, the analysis results for each sub-objective are provided.
Section 5.1 presents the results of damage detection from both densely and sparsely populated areas. It includes findings from the building footprint approach and explains the rationale for transitioning to the grid-based approach. The section also shows the change in performance due to this shift. Further, it explains the process of determining the building size threshold for damage detection, highlighting the challenges in accurately determining that value. Additionally, the generalizability of the damage detection model, trained and tested on data from Türkiye to data from Syria is explained.
Section 5.2 presents the results of response assessment from both densely and sparsely populated areas, highlighting that response activities were detected with high accuracy in both regions.
Section 5.3 presents the approach and results of integrating Pleiades data with PS, aiming to increase the comprehensiveness of damage detection and response assessment.

5.1. Damage detection

5.1.1. Densely populated regions

The building footprints were initially labelled manually from direct observations and each building unit was used to extract the different texture features (Figure 8 a) from PS multispectral images. The research first focused on finding one texture feature that would satisfactorily detect damage. However, none of the texture features individually were able to discriminate the binary classes for damage detection. Annex 4 provides the evaluation metrics showing the low accuracy, precision, recall and F1 values of individual texture measures ranging from 0.4-0.6.

The feature selection functionality of random forest algorithm was applied to improve the performance of classification (Akbari et al., 2020). This feature selection functionality selected all the texture features except correlation and entropy and then retained the random forest classifier with these. However, the observed area under the curve (AUC) value lower than 0.7 (Figure 15) failed to meet the acceptable threshold for reliable accuracy (Annex 2).

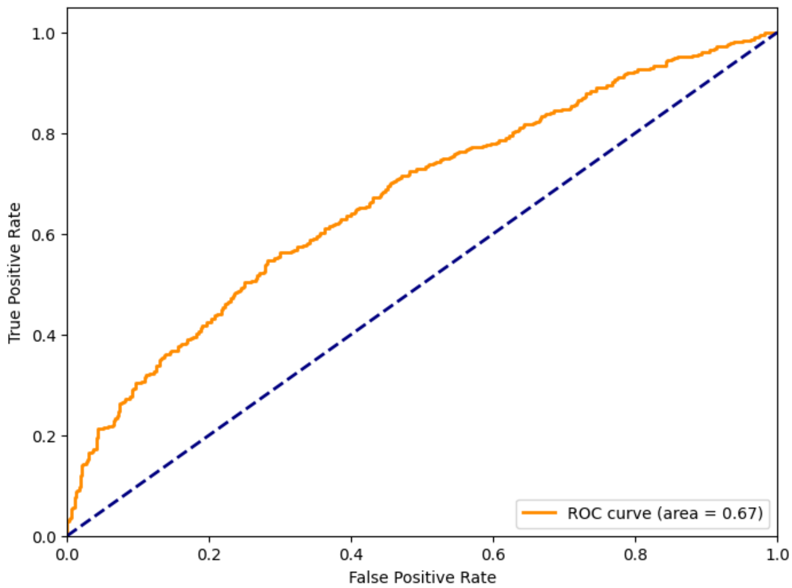

Figure 15. Area under the ROC curve for damage detection after feature selection, labelling at building footprint level (Table 8 a)

To understand the distribution of correct predictions made using this approach, accuracy per building range was calculated. Figure 16 shows the accuracy per building range along with the number of samples belonging to each range.

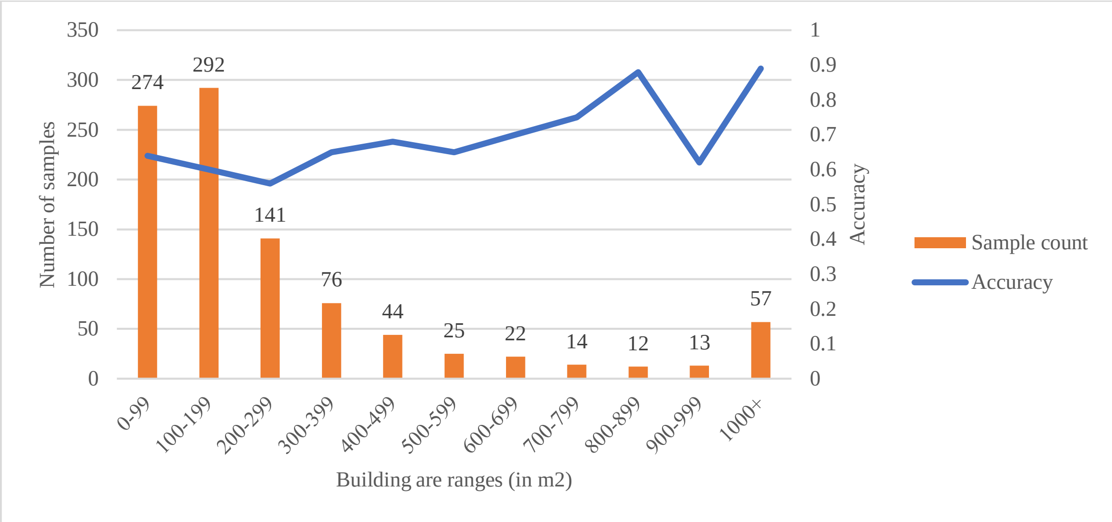

Figure 16. Accuracy per building range: Densely populated area for damaged labelling at building footprint level (Table 8 a)

It can be observed that the accuracy of damage detection increased with the increasing size of the buildings. The dips in the chart are misclassifications due to illumination differences, shadows and similar artefacts. Based on this observation, a grid-based approach was adopted for analysis (Table 8 b and c). The building sizes that showed an accuracy of 0.7 and above were selected for testing. Annex 3 shows that the performance of all the selected grid sizes for damage detection (labelling as Table 8 c) was comparable with high AUC values of 0.7 and above. However, to select the appropriate grid size, 'recall' values were further checked (Figure 17). The grid size with the highest recall for 'observable damage' was selected for analysis. This is because a higher recall value indicates fewer false negatives, meaning fewer missed damages.

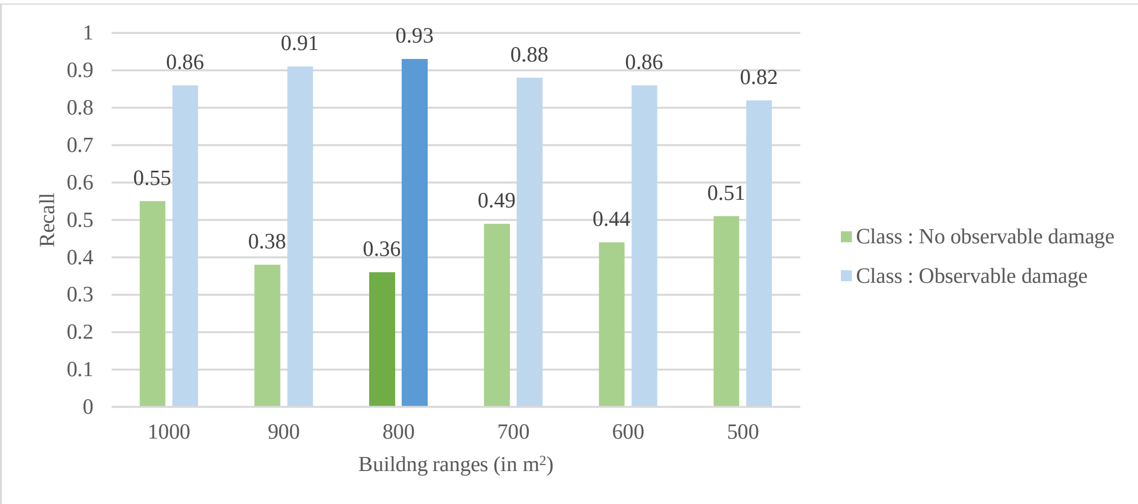

Figure 17. Recall values of different grid sizes for damage detection using damage labelling at the grid level (Table 8 c and d)

Therefore, the grid size selected for analysis was 800 m². This grid size was tested for damage detection in sparsely populated areas and labelling and testing classification for response activities in focus.

5.1.2. Sparsely populated regions

Damage detection using building footprint with both individual texture features and feature selection method on multispectral PS images showed suboptimal performance with ROC AUC below 0.6 for sparsely populated regions. The grid-based approach with a grid size of 800 m² was applied to detect damage, however, this grid size did not give acceptable accuracy results. The distribution of correct predictions per building range was examined for sparsely populated areas (Figure 18). While the chart shows a reasonable degree of accuracy for smaller buildings, due to the lower number of larger buildings (typical in sparsely populated areas) the model's prediction for these ranges was less consistent.

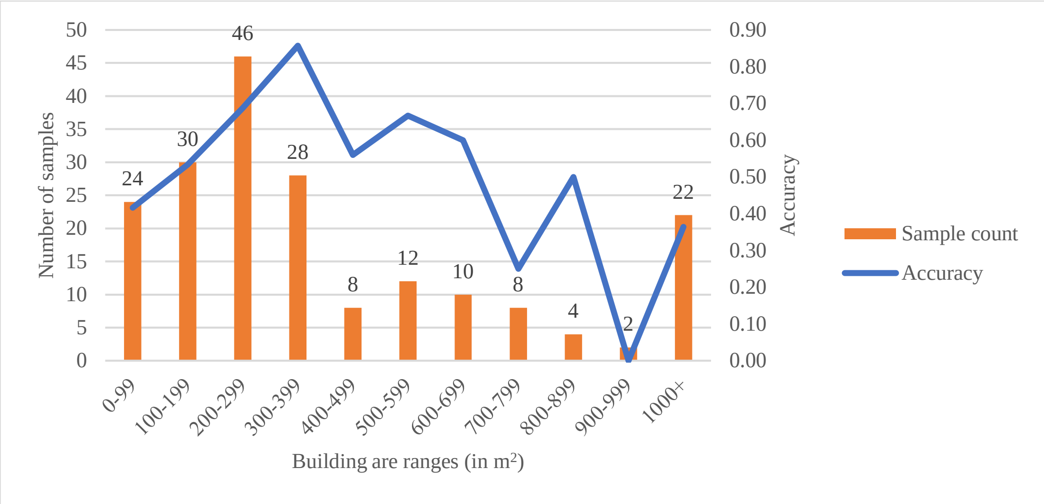

Figure 18. Accuracy per building range: Sparsely populated area

Figure 19 shows the classification results which highlight those buildings in the range of 300-399 m² that were accurately detected for damage. Therefore, a grid size of 300 m² was selected for testing damage detection for sparsely populated regions.

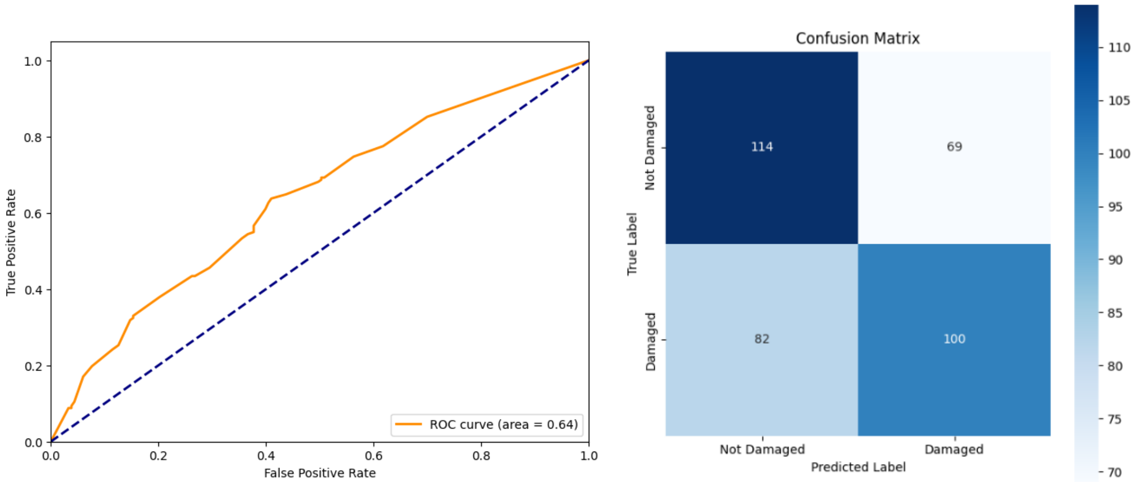

Figure 19. Area under the ROC curve and confusion matrix for damage detection in sparsely populated area with grid size of 300 m²

An AUC of 0.64 indicates modest discrimination of classes but it does not show high accuracy. The confusion matrix further highlights that for sparsely populated areas significant number of damaged areas could not be differentiated from those that were not damaged.

While experimenting with integration of PS with available higher-resolution Pleiades satellite images (explained in detail in section 5.3), individual red, green and blue bands were extracted from both PS and Pleiades images. Due to absence of pre-event Pleiades image, image differencing could not be performed, and only post-event images were used for damage detection classification. While multispectral PS images could not detect damages in sparely populated areas with high accuracy (Figure 19), it was observed that individual bands were capable of achieving this (Table 11).

Table 11. Accuracy for damage detection by individual bands for sparsely populated region

PS Band	ROC AUC
Red	0.76
Green	0.75
Blue	0.74

The results of damage detection from densely and sparsely populated areas show that while multispectral PlanetScope images can capture large-scale damages in densely populated areas, individual bands work better for sparsely populated regions.

Secondary damages due to aftershocks could not be studied due to the unavailability of information on the same required for labelling and validation.

5.1.3. Building size threshold for damage detection

Using the method employed by Kussul et al. (2024) to determine the relationship between the detected craters due to war and their areas, a density plot was used to find the building size threshold for damage detection using texture measures on PS data. In the density plot, the x-axis represents the building area (m^2) and the y-axis represents the probability density. The plot shows how the density of building areas is distributed for correct and incorrect predictions. Although the visual representation might suggest that the area under the curve for correct predictions is smaller than that for incorrect predictions, this is due to the distribution of the data points. The total area under each curve sums to 1, ensuring valid probability distribution for both correct and incorrect predictions.

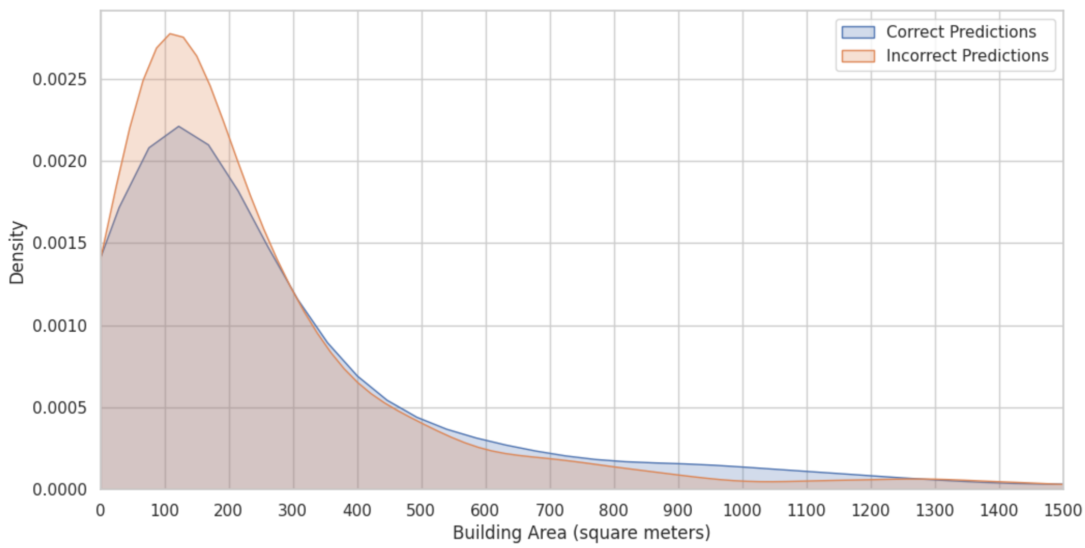

Figure 20. Probability density plot of building areas by prediction accuracy

Figure 20 shows that the accuracy of smaller buildings tends to be lower, indicated by the higher density of incorrect predictions compared to the correct ones. Despite this observation, it is challenging to find the exact threshold for minimum detectable damage size because of several factors and limitations:

- The number of samples in different size ranges (Figures 16 and 18) varies significantly, leading to less reliable accuracy measurements.
- Despite correction efforts to align the building footprints (section 4.1.2.1), minor misalignments persisted, particularly affecting damage detection.
- The effectiveness of texture-based analysis relies not only on the spatial resolution of the image but also on potential artefacts (Annex 6) induced by the sensor and noise like shadows, haze etc., as texture is calculated from pixels within the defined window in GLCM. Even if the building is not under direct shadow or affected by any other artefact, the presence of such issues in the neighbouring pixel can still alter the texture. These can create patterns that lead to misclassification by either mimicking the actual damage or hiding the damage.
- The detection of damage largely depended on the complete collapse of buildings, which visibly showed the presence of debris and/or the absence of a roof (Figure 21). Smaller buildings exhibiting these characteristics were correctly identified as damaged, whereas those with partial damage and no significant change in or around the building often went undetected.

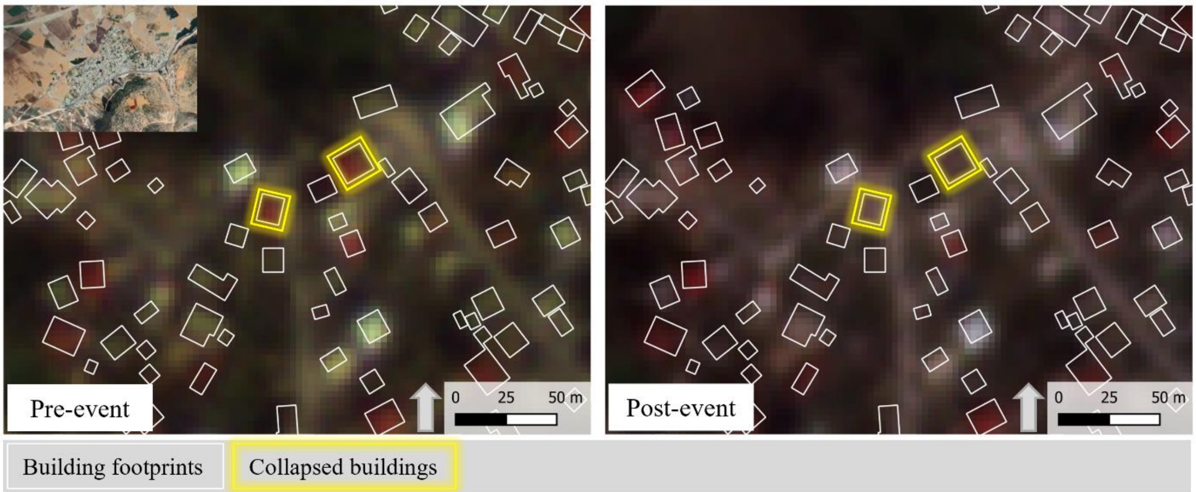

Figure 21. Absence of roof detected as damage for building sizes 100 m² (approx.) from Sakcagozu (AOI 4)

Therefore, determining an exact threshold for the building size for damage detection is complex due to challenges in texture analysis coupled with artefacts in PS images, misalignment of building footprints and sample size differences. Additionally, damage detection is straightforward for buildings with evident collapse, while partial damage particularly to smaller buildings is harder to identify. These factors make it difficult to establish a size threshold for reliable damage detection based on the methodology of this research and also highlight that the detection of damage does not solely depend on the building size.

5.1.4. Quantification of damage using KDE

Due to the variability of GLCM texture measures, direct quantification of damage through the selected texture measures was not feasible. To overcome this challenge, the Kernel Density Estimator (KDE) was employed for damage quantification (explained in section 4.5.1). Figure 22 visualizes the spatial distribution of damaged buildings using KDE across Kahramanmaras (AOI 1). The map shows varying density of damage, from blue (no damage) to red (highest concentration of damage).

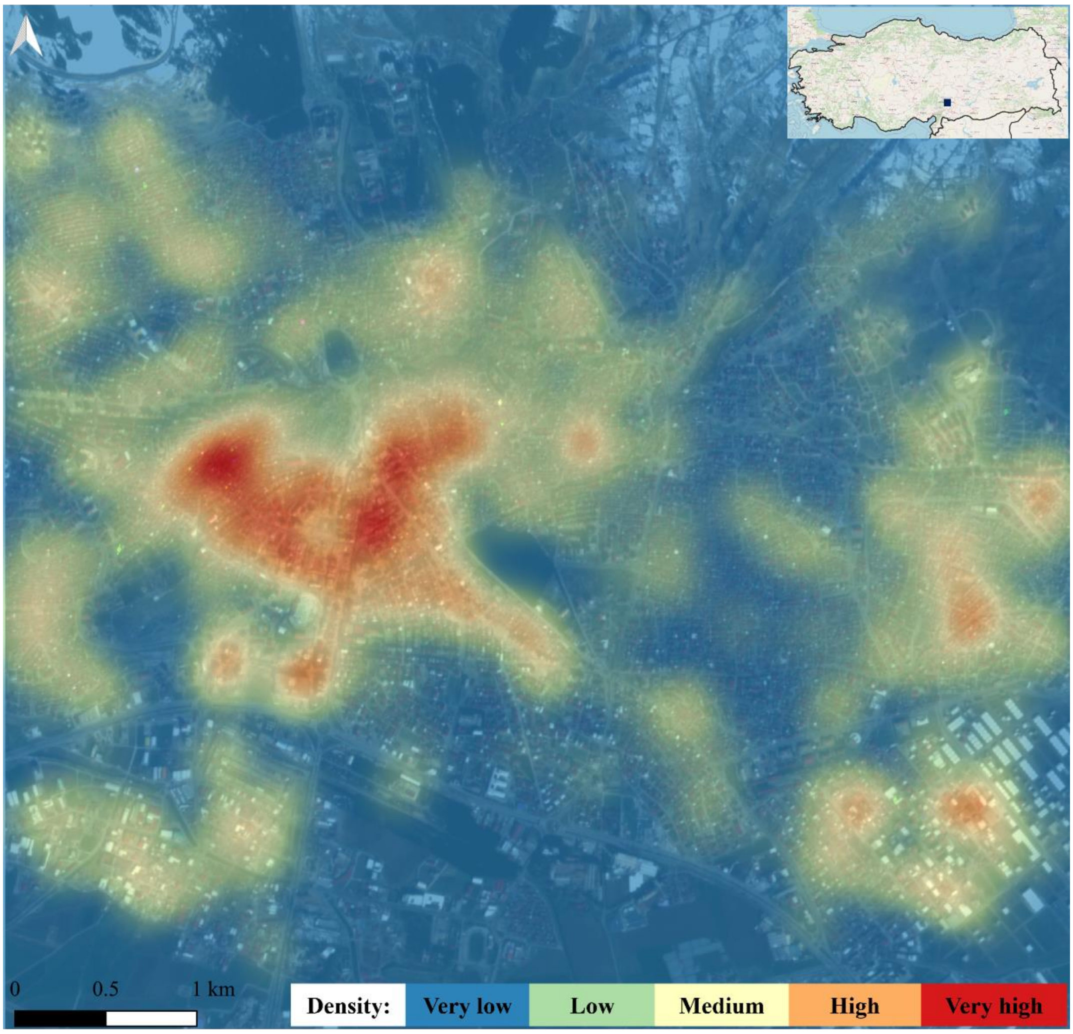

Figure 22. Kernel Density Estimation output for Kahramanmaras (AOI 1) showing damage density as of 08 February 2023

It can be observed that areas with more damage have higher density values (orange and red), whereas areas with few or no damage have lower density values (blue, green and yellow). To ensure a balanced representation of damage across the study area, the damage density classes were created by dividing the data into five equal parts. The KDE density values vary across different areas due to the distribution of damage within each area of interest.

5.1.5. Generalizability of the damage detection model

As mentioned in 3.1, due to the limited availability of higher-resolution images and required information from Syria, which was also impacted by the earthquake, the research mainly focused on locations from Türkiye. However, to test the generalizability of the damage detection model trained and tested on Türkiye data, Jindires (Aleppo) located in Syria was selected.

Direct application of the model trained on data from Türkiye for damage detection in Syria gave poor accuracy results, with a ROC AUC of 0.41. This can be attributed to the difference between the buildings and damage patterns from the two regions (Figure 13) resulting in different texture patterns that correspond to the change. Further, pre-existing damaged buildings due to the war in the region (Alhaffar et al., 2023) can also be one of the reasons behind the observed difference.

An independent samples T-test was performed to compare the means of the texture measures from Türkiye and Syria to determine the points of differences. T-tests also calculate p-values to provide further support in highlighting the differences. A low p-value (<= 0.05) shows a high difference while a high p-value (>0.05) shows no significant difference (Adamu et al., 2018). The texture measures representing damaged and non-damaged grid units from both the countries were compared, table 12 shows the results.

Table 12. T-test results with p-values for texture measures from Türkiye and Syria for damage detection

Comparison	Texture	T-statistics	p-value
Syria damage vs. Türkiye damage	Variance	1.097	0.277
	Mean	4.077	0.000128
	Homogeneity	1.949	0.0557
	Entropy	-2.094	0.0399
	Dissimilarity	-1.39	0.169
	Contrast	-0.004	0.997
Syria non-damage vs. Türkiye non-damage	Variance	0.019	0.985
	Mean	3.21	0.002
	Homogeneity	3.384	0.0013
	Entropy	-2.356	0.0222
	Dissimilarity	-2.823	0.0067
	Contrast	-1.013	0.316

* Significant difference and potential difference

On comparing 'damaged' texture measures from Türkiye and Syria, it can be observed from the T-values that mean and entropy show high differences, indicating significant variation of these textures from damaged areas between the two regions. The p-value of homogeneity also suggests potential difference, but variance, dissimilarity and contrast show no significant difference. On comparing 'non-damaged' texture measures from Türkiye and Syria, it can be observed from the T-values that mean, homogeneity, entropy and dissimilarity show high differences indicating significant variation of these textures from non-damaged areas between the two regions.

These differences explain the low accuracy observed when generalising the classification model from Türkiye to Syria. The variations in texture measures, such as mean and entropy, between the two regions suggest that the buildings and damage patterns differ significantly between the two regions. The model was retrained using data from Syria (following the same methodology applied to data from Türkiye), resulting in a higher accuracy value of 0.7. The higher accuracy can be attributed to the model learning the unique and different texture features representing damage from Syria.

5.2. Response assessment

5.2.1. Temporary shelters

One of the response activities focused on in this research was the evolution of temporary shelters. This included identifying their presence, absence, removal and transition to semi-permanent container settlements. The grid-based approach employed for damage detection (grid size 800 m^2) was applied for labelling and detecting the evolution of temporary shelters. Table 13 shows the performance of different texture measures, highlighting that 'mean' gave the highest accuracy of 0.82.

Table 13. Performance of different texture measures for detecting the evolution of temporary shelters

Texture	Absent	Present	Removed	Semi-permanent	Micro-average ROC
ASM	0.71	0.64	0.55	0.77	0.71
Contrast	0.65	0.59	0.65	0.63	0.68
Correlation	0.66	0.61	0.58	0.61	0.67
Dissimilarity	0.68	060	0.66	0.66	0.70
Entropy	0.69	0.64	0.60	0.73	0.71
Homogeneity	0.70	0.58	0.74	0.68	0.71
Mean	0.82	0.67	0.79	0.85	**0.82**
Variance	0.66	0.66	0.85	0.69	0.70

The accuracy of detecting the presence of temporary shelters is comparatively lower than other classes due to the difference in the placement of these structures. While many shelters were clustered together, there were also cases where individual shelters were built on any available open space (Annex 5). These isolated structures which were small in size, posed challenges in detection, affecting the accuracy. Detecting the evolution of temporary shelters with high accuracy was possible for both densely and sparsely populated because the types of shelters that were established in both regions were the same.

Additionally, the minimum number of images required to monitor the evolution of temporary shelters effectively was assessed. Figure 23 presents the graph depicting the decreasing accuracy as the number of images in the time series decreases.

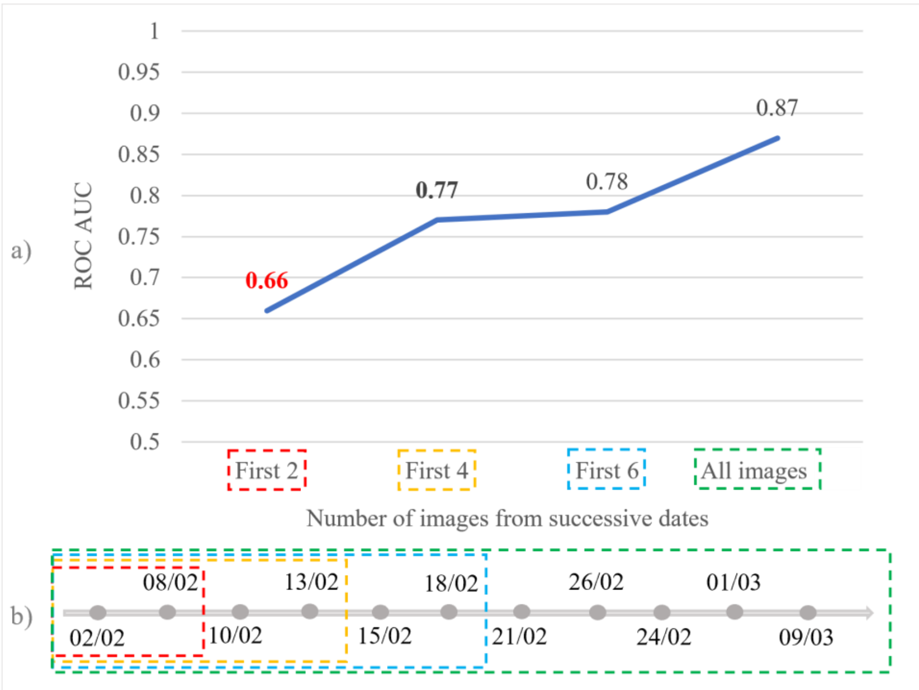

Figure 23. (a) Accuracy for different time-series combinations when detecting the evolution of temporary shelters and (b) available images from Nurdagi (AOI 3)

It can be observed that a minimum of four images, including pre-event images, is necessary to achieve high detection accuracy.

5.2.2. Debris

The other response activity focused on in this research was debris. Due to the lower resolution of PS images and limited availability of higher-resolution images from post-event dates, monitoring debris removal progress was challenging. Therefore, the scope of this research was confined to debris detection. Utilising the available higher-resolution images and research conducted by Mavroulis et al. (2023), the sites of debris disposal were identified and included as an additional class in the debris detection process. However, the samples in this class were lower than other classes. To balance the dataset, class weights proportional to the frequency of each class were assigned. The less pronounced ROC AUC curve (Annex 7), particularly for the 'debris disposal site' class, further highlights the lower number of samples in this class. The three classes of debris were detected with high accuracy in both densely and sparsely populated areas. This could be attributed to the focus being only on completely or partially collapsed buildings that evidently showed destroyed materials in their vicinity (these were also the correctly identified damaged buildings highlighted in the previous sections). Table 14 shows the performance of different texture measures (combined from densely and sparsely populated regions) for the detection of debris and its disposal site.

Table 14. Performance of different texture measures for detecting debris

Texture	Absent	Present	Disposal site	Micro-average ROC
ASM	0.86	0.88	0.85	0.89
Contrast	0.62	0.67	0.61	0.63
Correlation	0.59	0.65	0.66	0.64
Dissimilarity	0.88	0.92	0.87	0.91
Entropy	0.85	0.87	0.87	0.89
Homogeneity	0.82	0.87	0.84	0.87
Mean	0.91	0.90	0.94	0.92
Variance	0.84	0.90	0.88	0.89

It can be observed that all texture measures, except contrast and correlation, gave high accuracies (0.8 and above) for the detection of all the classes (< 0.7).

5.2.3. Quantification of shelter area and expansion

The expansion of temporary shelters, particularly the container settlements was done using the time-series images from Nurdagi (AOI 3), explained in section 4.5.2. There were a total of 10 images from this location and each image showed an evident increase in area covered by these shelters during the response phase. The following were calculated:

- Cumulative area covered- By calculating the area covered by temporary shelters on each date (counting the number of grids of size 800 m^2) to estimate the increase in area over the specified duration.
- Rate of expansion- By understanding the change in cumulative area per unit time (m^2/day) to find the speed at which the temporary shelters were spreading.

Table 22 in annex 8 provides detailed information on the calculations.
Figure 24 shows that the initial growth of container shelters was slow, this can indicate that organizing and deploying resources took time. However, the increase from February 10 suggests that more resources might have been mobilized for constructing stronger shelters for the impacted population. The steady growth highlights constant efforts to expand the shelters.
The sharp peak in Figure 25 indicates (on 15th February) indicates focused response efforts regarding shelter provision and construction around that time. The decreasing trend suggests that the initial need for shelters

may have been met or available space expansion or resources could have had limitations. However, the continued positive rate of expansion shows that the expansion continued, though at a slower rate.

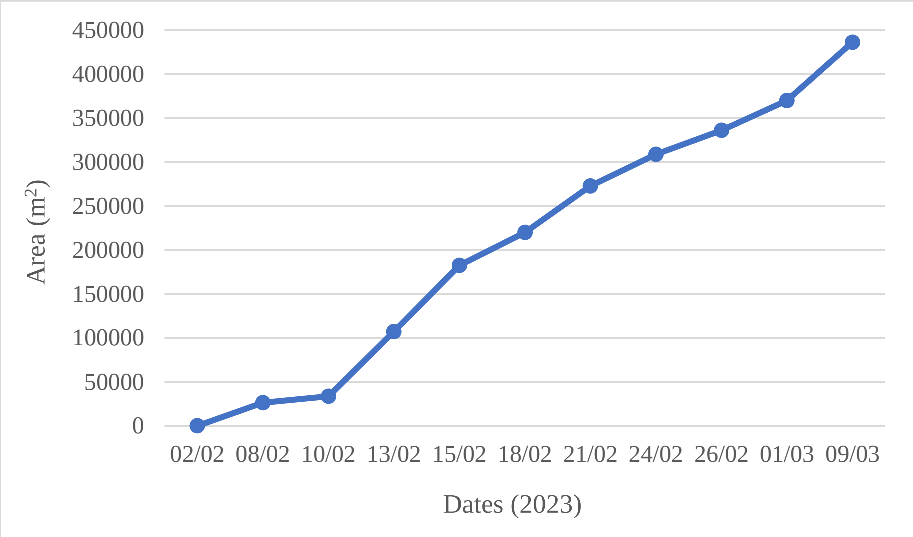

Figure 24. Cumulative area covered by temporary shelters (container settlements) in Nurdagi after the earthquake

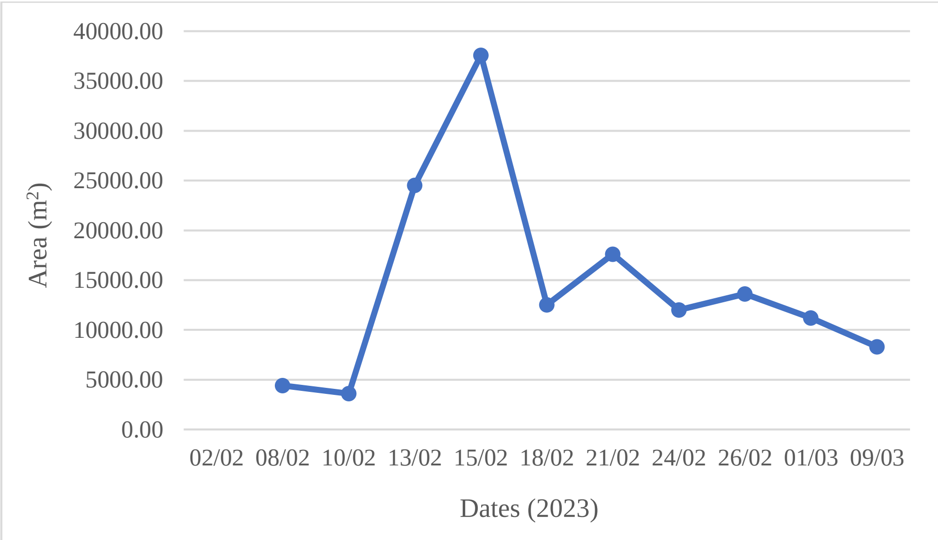

Figure 25. Average daily rate of expansion of temporary shelters (container settlements) in Nurdagi (m^2/day) after the earthquake

Such quantitative analysis can help understand shelter dynamics, allocation of resources and overall impact of intervention.

Debris detection was another aspect that was studied and that can be quantified using the same KDE analysis employed for damage quantification (explained in section 5.1.4). However, to avoid redundancy, the visualization of the debris density map has been provided in annex 9. This decision is based on the observation that the majority of damage identified by PS images relates to completely or partially collapsed structures, which already indicates either the absence of a roof or the presence of debris.

Table 15 summarizes the findings, focusing on damage and response activity detection supported by PlanetScope, along with minimum data requirements for each.

Table 15. Summary of findings from damage and response activities detection with PlanetScope

Parameters		Damage	Temporary shelters	Debris
Random Forest Classification	Binary	✓	✓	✓
	Multi-class	✗	✓	✓
Primary		✓	NA	NA
Unit of labelling	Building footprint	✗	✗	✗
	Grid-based	✓	✓	✓
Area of focus	Densely populated area	✓	✓	✓
	Sparsely populated area	✓	✓	✓
Quantification		✓ Showing spatial distribution of damage density in the study area	✓ Cumulative area and expansion rate of shelter construction	✓ Showing spatial distribution of debris density in the study area
Minimum requirements for the images		Post-event image	Hyper-temporal images, minimum 4 (including pre-event image)	Bi-temporal (pre and post) images for detection, additional images from a week (minimum) after the event for detecting debris collection sites

5.3. Integration of PS with higher-resolution satellite image

5.3.1. Use of higher-resolution images as ground truth

After labelling the PS images based on direct observations and obtaining the classification results on damage detection (explained in section 5.1), the higher resolution WorldView images were used to support the labelling process (5% change and 20% increase in 'observed damage' labels) (explained in section 4.6). This approach was undertaken to evaluate the impact of utilising the available higher-resolution dataset on classification accuracy. Figure 26 shows the ROC AUC plot obtained from the classification results using this approach.

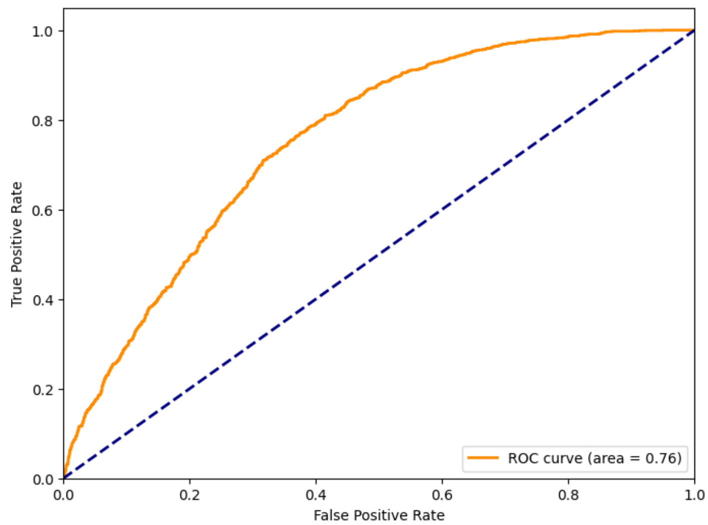

Figure 26. Area under the ROC curve for damage detection after using WorldView images to support labelling.

The accuracies of classification with and without the use of WorldView images for labelling are 0.76 and 0.7, respectively (section 5.1). The slight increase in performance highlights that while PS images alone can identify damage patterns, incorporating higher-resolution WorldView images significantly enhances the accuracy of damage detection. This suggests that the additional information provided by WorldView enabled the identification of the patterns that are difficult to find through visual interpretation of PS images alone.

5.3.2. Use of higher-resolution image for sharpening PS image

In addition to using higher-resolution images as ground truth and confirming the presence of damage and response activities as mentioned in previous sections, they were also used to increase the details of PS images through pan-sharpening (explained in section 4.6). Due to the unavailability of panchromatic Pleiades image, its individual red, green and blue bands were used to sharpen the corresponding red, green and blue bands of PS images from Nurdagi (AOI 3). Additionally, only one post-event image was sharpened and thereby used for damage detection due to the absence of a pre-event Pleiades image.

The high-pass modulation method was used to sharpen the PS image using one Pleiades image as explained in section 4.7. This was followed by edge detection using the Canny edge detection method to evaluate the effects of sharpening.

Table 16. Comparison of edge pixels between original and sharpened post-event PS image (individual bands)

Band	No sharpening	Sharpening with modulating factor 0.2	Sharpening with modulating factor 0.5	Sharpening with modulating factor 1
Red	258310	259208	266388	248262
Green	224374	225518	237189	221802
Blue	184466	185676	206462	197329

Table 16 shows that sharpening with a factor of 0.5 significantly increases the number of edge pixels across all bands, while a factor of 1 leads to a reduction in the number of edge pixels suggesting potential over-sharpening that might cause blurring of details.
After producing individual red, green and blue-band sharpened PS images, GLCM was performed, followed by damage detection to compare the accuracy results with and without sharpening.

Table 17. Comparison of damage detection accuracies between original and sharpened post-event PS image (individual bands)

Band	No sharpening	Sharpening with modulating factor 0.2	Sharpening with modulating factor 0.5	Sharpening with modulating factor 1
Red	0.76	0.73	0.80	0.75
Green	0.75	0.76	0.76	0.80
Blue	0.74	0.74	0.78	0.76

From Table 17 it can be observed that sharpening with the modulation factor of 0.5 gives higher accuracy, particularly for the red and blue bands. However, the green band shows an improvement with a modulation factor of 1. As expected, sharpening enhanced the details in the image, thereby improving the damage detection accuracy. However, excessive sharpening resulting from a modulation factor of 1 does not yield better results due to the introduction of noise and artefacts due to the sharpening (as seen for red and blue bands).

Tables 16 and 17 collectively suggest that the sharpening factor of 0.5 is the most effective in enhancing image quality for edge detection and improving damage detection accuracy.

Figure 27 shows the sharpened PS image resulting from different modulation factors.

Figure 27. Visual comparison of PS images sharpened by a post-event Pleiades image using modulation factors for Nurdagi (AOI 3) showing (a) temporary shelters, (b) road cross-section and debris pile, (c) buildings.

The classification performance of response activities could not be tested due to the unavailability of Pleiades images from post-event dates. However, it can be observed from Figure 27 that the temporary shelters, debris and buildings become more pronounced when a PS image is sharpened. This indicates that individual shelters (Annex 5), debris piles and building damage could potentially be detected with higher accuracy compared to the accuracy result from the PS image alone (explained in section 5.2.1).

The following chapter will provide a detailed discussion of all the results presented in this chapter.

6. DISCUSSION

This research aimed to assess the suitability of PlanetScope in identifying post-disaster damages, and response activities, using the case study of Turkey-Syria earthquakes from February 2023. The methodology involved texture-based feature extraction using GLCM, summarising the changed texture for building and grid units, followed by classification using a supervised machine learning algorithm, random forest. Damage and response activities were identified for the selected areas of interest in Turkey, from both densely and sparsely populated locations. Although Syria was also significantly impacted by the earthquake amidst ongoing conflict, due to the limited availability of higher-resolution images (only one freely available post-event WorldView image), it could not be included as one of the areas of the main focus in this research. However, a location from Syria (Jindires, Aleppo) was selected to test the generalisability of the model trained and tested on data from Turkey. In this chapter, the methods and results corresponding to each sub-objective of this research will be critically examined and discussed.

Research sub-objective 1: To investigate the utility of PlanetScope in detecting post-disaster damage.

R.Q. 1.1: Can PS be used to undertake damage detection in both densely and sparsely populated regions?

This research shifted from detecting damage at the building level to a grid level. The initial attempts to identify a single texture measure using GLCM from the multispectral PS image for damage detection were unsuccessful, with the individual texture measures giving poor accuracy (lower than 0.6). By employing feature importance in the random forest algorithm, it was found that a combination of features could collectively improve accuracy. Despite this, building-level damage detection using GLCM was challenging (accuracy lower than 0.7). This can be attributed to:

- Building footprint information- Studies by Li et al. (2023) and Ullah et al. (2023) have highlighted the issues of misalignment and completeness (respectively) of building footprints from OpenStreetMap (the main building footprint dataset used in this research). Although the alignment issues were reduced using transformations and missing footprints were added from the Microsoft building dataset, inconsistencies in the building information persisted. These inconsistencies can lead to misclassification, affecting the reliability of damage detection.
- Limitations of PS images- The relatively lower spatial resolution of three meters is not optimal for capturing damage to buildings that do not show significant changes due to their small size and/or partial damage. Despite pre-processing, ensuring consistent data quality across the large number of time-series images acquired for monitoring change was challenging. Pickering et al., (2021) noted that different sensors and image acquisition conditions can introduce inconsistencies that can further affect change detection.
- Window size in GLCM- The texture measures were calculated using a window size of 3 by 3 pixels. For each building unit, these texture measures were summarized by calculating the mean of all the texture pixels within that unit. However, since some buildings may extend beyond the window size, this approach might not capture the full extent of changes, potentially resulting in some building damages being overlooked.

Several factors led to the transition from building-level damage detection to a grid-based approach. Using a grid size larger than a typical small building but comparable to the size of a larger building allowed to utilize surrounding information more effectively during manual labelling. This approach ensured that if there were multiple small buildings within a grid, their collective damage could be assessed together. Additionally, if there is only a single large building within the grid, the grid size will capture the building accurately. Furthermore, for automatic labelling, this surrounding information helps improve the accuracy of damage detection by considering the context provided by neighbouring buildings or structures. Upon transitioning to a grid-based approach, where damage detection was conducted on a larger scale, better results were obtained, with ROC AUC of 0.7 and higher. The grid size of 800 m^2 was selected based on its highest recall value (fewer missed damage) observed in densely populated areas for damage detection while comparing the evaluation matrix of different grid-sizes (Annex 3). In contrast, sparsely populated areas, with fewer buildings and smaller building sizes, required a smaller grid-size of 300 m^2 for damage detection, though the accuracy remained less than 0.7. This grid size was also selected based on accuracy observed for different building size ranges. However, the inconsistency in the sample size between the different building size ranges in sparsely populated areas led to high variability in accuracy. Although a balanced dataset was created by under-sampling the majority class for damage classification, another step to balance the samples in different area ranges would have provided better insights for selecting an appropriate grid-size for both densely and sparsely populated areas. Such a grid-based method for classification simplified the labelling process, which was faster and proved to be reliable for identifying damaged areas. This can particularly be beneficial in situations where rapid assessments are needed. Also, the approach of labelling ensured that all potential damages were detected, by labelling any grid which contained even parts of the damaged building. However, this can also lead to overestimation of damage and loss of detail.

Interestingly, experiments with individual spectral bands showed that they could detect damage in sparsely populated areas with high accuracy (0.7 and above) with a grid size of 300 m^2. This can be attributed to the spatial details of multispectral images not being as refined as those of single-band images (Zhang et al., 2023). He et al. (2021) also highlighted that multispectral images captured at different times often experience radiation differences, that can significantly impact the accuracy of change detection. Lastly, post-event PS images alone are sufficient for damage detection, without the need for pre-event images. The use of only post-event images for damage detection has also been supported by multiple studies such as by Cao et al., (2020), Nex et al. (2019) and Valentijn (2020).

In conclusion, while PlanetScope imagery is not effective for accurately detecting building-level damages, it is suitable for conducting large-scale (grid-based) damage assessments. This grid-based approach can prove useful for providing an overview of damaged areas in any desired location with PlanetScope. Further, multispectral images are effective for detecting damages in densely populated areas, whereas individual spectral bands provide reliable results in sparsely populated regions. Lastly, post-event PS images alone are sufficient to capture changes indicating damage.

R.Q. 1.2: Can the identified damage by PS be quantified?

The analysis in this research focused on binary classification of damage and the texture measures derived from GLCM varied differently to indicate changes observed. This variation made it difficult to assign a quantitative measure to the damage observed using GLCM texture values. As a result, KDE was employed to estimate the density of damage across the area of interest to provide a quantifiable measure of damage. Figure 22 shows that identifying areas of high damage density can help concerned authorities prioritize resource allocation. This can also guide rescue forces and emergency response teams to areas requiring the most support, improving the efficiency and effectiveness of the operations. This can further prove useful for city planners by understanding the damage pattern and providing required building codes and guidelines for resilient infrastructure in highly damaged areas.

The attempt to find the minimum threshold of damage detection was challenging. The accuracy of damage detection was found to increase with increasing building size, particularly becoming more reliable for buildings from 300 m^2 onwards. One of the study areas selected from Kahramanmaras (AOI 1) comprises of 977 buildings with an average size of 340 m^2. The average size of buildings that collapsed in Kahramanmaras is 450 m^2, while the average size of buildings that did not collapse is 230 m^2. This indicates that larger buildings, particularly above 300 m^2, are more likely to be detected as damaged. These larger buildings comprise of high-rise structures, making them detectable when completely damaged. These high-rise buildings are not uniformly distributed across all the AOIs and are primarily present in urban areas like Kahramanmaras (AOI 1), Antakya (AOI 6) etc. In contrast, sparsely populated or rural areas like Turkoglu (AOI 2) and Nurdagi (AOI 3) have significantly smaller average building sizes, around 200 m^2. The average size of both observed damaged and non-damaged buildings in these areas falls within this same range. This shows that smaller buildings in rural areas are closer in size to the threshold where detection accuracy gets lower. However, Figure 21 showed that damages were also detected accurately for building sizes close to 100 m^2, if the structure had completely collapsed and the scene did not contain artifacts like shadow, cloud cover etc. This suggests that the detection of damage is effective even for smaller buildings. However, finding the minimum building size for damage detection using PS and the methodology used in this research remained challenging.

While there are limited studies addressing minimum detectable damage size, research focusing only on building detection provides useful insights. In alignment with the findings in this thesis research, You et al. (2018) highlighted that precision and recall for building detection improve significantly with larger building sizes, but detecting smaller buildings is still challenging. Mason et al., (2023) also highlighted that even with d deep learning algorithms like CNN, detecting smaller structures remains generally challenging. However, in their research on extracting building inventory using PS images, Kaplan et al. (2020) found that their deep learning method effectively identifies small buildings, although not specifying the size of the small buildings.

The findings from this research and existing studies show that PS data with advanced algorithms shows the potential to detect building damages of varying sizes. The detection of the minimum threshold in this research remained challenging due to the analytical techniques employed. However, the quantification of damage was feasible using kernel density estimation. Similar algorithms like density-based spatial clustering (DBSCAN), spatial autocorrelation etc. can also be employed to identify spatial patterns (clustered or dispersed) and provide an overview of damage level across the area of interest.

Additional R.Q: How well does the generalizability of the damage detection model trained and tested on data from Türkiye extend to detecting damage in Syria?

Due to the limited availability of ground truth and higher-resolution images from Syria, its locations could not be included for detailed analysis in this research. However, Jindires from Aleppo was used to check the generalizability of the damage detection model trained and tested on data from Türkiye. Statistical analysis using the T-test revealed significant differences in texture patterns related to earthquake damage between Türkiye and Syria. Additionally, pre-earthquake war-related damage adds to the differences in texture patterns, particularly between the pre-event images used from the two regions. Therefore, the model performed poorly when applied to data from Syria, achieving a low ROC AUC of 0.41. However, after incorporating Syrian data into the training process, the model's performance significantly improved, achieving the ROC AUC of 0.7. This indicates the importance of including region-specific data to ensure higher accuracy and reliability of the model's performance in damage detection in diverse geographic contexts (Arya et al., 2020). There are also studies that have proposed advanced machine learning methods to enhance the generalizability across different hazards and locations without using a target domain data (Jakubik et al., 2023; Nex et al., 2019). Such methods further reduce the necessity for location-specific damage information, enabling more effective transfer of damage detection models across different areas of interest.

Research sub-objective 2: To investigate the utility of PlanetScope in detecting post-disaster response activities.

R.Q. 2.1: For which response activities can PS be used to monitor in both densely and sparsely populated regions?

The response activities studied in this research were the evolution of temporary shelters and debris removal progress.

Temporary shelters

The evolution of temporary shelter included detecting its presence, absence, removal and transition to semi-permanent (container) settlements. It was found that using the methodology employed in this research, all the mentioned categories of temporary shelter evolution can be detected with high accuracy in both densely and sparsely populated areas. This is because the type of temporary shelters being set up were the same across the country. The grid-based approach was applied here as well, using a grid size of 800 m^2. However, individual temporary shelters that were set up in isolation or on random open spaces available, were detected with relatively low accuracy. This was primarily due to their small size and limited resolution of PlanetScope and GLCM texture to capture them efficiently. Similar findings were reported by Füreder et al. (2015), who, despite using higher resolution pan-sharpened WorldView-2 satellite images, were not able to detect smaller shelters with high-accuracy compared to larger or clustered shelters. Other studies using very-high-resolution satellite images to detect shelters, such as those by Gella et al. (2022) and Ghorbanzadeh et al., (2022), have only detected the presence and absence of these shelters using deep learning algorithms. While not focusing on each shelter unit, this thesis research further highlighted the application of texture features on lower-resolution PS images can also support monitoring the transition of temporary shelters.

Debris

Although the initial idea for this research was to monitor the removal progress of debris using the available time-series PS images, the limited spatial resolution of images posed challenges in understanding the progress directly. Additionally, the higher-resolution images available are from one or two days immediately after the event with some locations having a maximum of two images from the first week after the earthquake. The absence of higher-resolution images from a bit longer after the event does not allow to see the removal progress as the removal took usually place several days and weeks after the event. Hence, the removal progress could not be studied in this research. This research covered detecting the presence of debris and its collection locations documented by Mavroulis et al. (2023) that were identified with available WorldView and Pleiades images for the areas of interest. The classification results from both densely and sparsely populated areas showed that the presence of debris and its collection site can be detected with high accuracy with the methodology employed and data used in this research.

Christaki et al. (2022) also employed GLCM on very-high resolution images acquired using UAV and showed that debris removal progress can be successfully mapped. With higher resolution, the texture variation at the building level can be captured efficiently, and observed changes can directly indicate the presence or absence of debris. The study by Zhao et al. (2022) also utilized texture features derived from LBP to create a framework for detecting road damage and debris using high-resolution satellite images, although the resolution or source of the image was not specified. Additionally, other recent studies by Yilmaz et al., (2023) and Seydi et al. (2023) highlight the effectiveness of feature extraction in capturing the patterns and details associated with the changes being studied, regardless of the classification algorithm employed. These studies collectively underscore the importance of feature extraction in improving the accuracy of classification.

R.Q. 2.2: Can the identified activities by PS be quantified?

The spatial resolution of PS images posed significant limitations in quantifying the response activities in this research. Additionally, the grid-based approach was employed to monitor the classes of temporary shelters and debris in a defined zone. This approach could not support direct quantification.

However, PS images can be used for monitoring the rate of expansion or reduction of temporary shelters during the response phase using the available time-series data. Similar studies on monitoring informal and temporary shelters by Liu et al. (2019) and Mudau et al. (2022) successfully monitored the changes and rate of growth of these shelters but did not cover their precise quantification. Such an analysis from different areas of impact can provide insights into the reach and speed of authorities providing rehabilitation to the population. This can also highlight areas that may be underserved, highlighting the need to further find the reasons behind the same and take action accordingly. This information can help the authorities understand how quickly they scale up response efforts depending on the demand and adjust their methods as per requirement. Lastly, monitoring the expansion of shelters can help in planning for recovery.

For debris, the limited spatial detail of PS hindered the exact quantification of its volume. Existing studies on debris quantification such as Bekkaye et al. (2024), Labiak et al. (2011) and Miura (2019) have demonstrated that very-high-resolution data sources provide the required details to quantify the volume of debris. However, KDE employed for quantifying damage density can also be used for debris to get a quantitative measure of the spatial distribution of debris across the area of interest.

Research sub-objective 3: To determine the synergetic potential of PS with available higher resolution satellite images to increase the comprehensiveness of change detection using data integration technique.

R.Q. 3.1: How can higher-resolution data be integrated with PS?

R.Q. 3.2: How does the incorporation impact the comprehensiveness of damage and response assessment?

In this research, the integration of available higher-resolution images with PS images was conducted in the following three ways:

1. Ground truth- WorldView images were used as a benchmark to validate the classification performance of PS.
2. Confirming the presence of activities- Due to PS's limited spatial resolution, it was difficult to identify the debris collection site and confidently differentiate temporary shelters with similar structures in the scene. Higher-resolution satellite images (WorldView and Pleiades) were used to address this issue.
3. Sharpening- PS image from Nurdagi (AOI 3) was sharpened using the available Pleiades image, to increase the details of the former. A detailed sharpening attempt with multiple images could not be performed due to the limited availability of higher-resolution images.

As explained in section 5.3.1, using WorldView images improved the accuracy of damage classification in PS images. This shows that the higher-resolution dataset provided reliable ground truth, leading to an improved validation process. The higher details in WorldView images helped identify damage instances that were missed when manually labelled through visual interpretation of PS images alone. This approach of using high-resolution remote sensing data as ground truth is supported by several studies. For example, UAV data have been used as ground truth for mapping crop variety (Craver et al., 2020), and a combination of OSM and high-resolution optical datasets as ground truth has supported building footprint extraction (Li et al., 2019). This also highlights the utility of using freely available datasets, particularly under open data programs to support humanitarian crises, when ground truth availability is limited. Additionally, confirming the presence of elements like temporary shelters and debris collection locations that were not easily recognisable in the PS images alone, highlights the usefulness of integrating higher-resolution data for detailed situational awareness (Kedia et al., 2022).

Lastly, PS images were sharpened using available Pleiades image by following the concept of pan-sharpening. Pan-sharpening involves merging high-resolution panchromatic images with lower-resolution multispectral images to produce a higher-resolution multispectral image (Meng et al., 2019). Due to the absence of a higher-resolution panchromatic image, individual spectral bands (red, green and blue) from higher-resolution Pleiades images were extracted and corresponding individual bands of PS were sharpened using a high-pass modulation method. The quality assessment of sharpened images was performed using Canny edge detection. The results showed noticeable enhancement in details and edge pixels with modulation factors of 0.2 and 0.5, which can facilitate easier interpretation of elements in PS images. However, it was also observed that sharpening using a modulation factor of 1 led to a reduction of edge pixels, that potentially blurred details and resulted in lower accuracy for damage detection. This highlights the need for carefully applying sharpening and similar image-processing techniques to avoid issues.

The sharpening method used in this research was selected due to its low computational requirements/efforts and simplicity to demonstrate the synergistic potential of PS with available higher-resolution datasets. However, newer sharpening and fusion techniques leveraging deep learning-based algorithms, although requiring large amounts of training datasets, have also been developed and shown reliable performance in enhancing details of lower-resolution datasets (Javan et al., 2021). For example, Shin et al. (2020) designed a deep learning model for enhancing the resolution of PlanetScope images using WorldView images, and Latte et al. (2020) presented a CNN-based method for improving the spatial resolution of Sentinel-2 images using PlanetScope images.

In conclusion, this research demonstrates that integrating higher-resolution images in various ways significantly enhances the validity, discriminative abilities and details of PS images, thereby improving the overall analysis. This confirms that higher-resolution datasets can be used for enhancing the comprehensiveness of analysis, particularly when using relatively lower-resolution satellite data sources like PS.

Supervised machine learning

This research employed a supervised machine algorithm, random forest, for classification. This was selected over state-of-the-art deep learning methods due to the following reasons:

1. Exploratory nature of the research- Although PlanetScope has been used in many studies to show its effectiveness in detecting environmental damage and integrating with satellite images of different resolutions to enhance image details (highlighted in previous sections), its potential for identifying post-disaster damage and response activities was underexplored. For this exploratory research, an easily implementable model requiring low operational and computational resources (Ramezan et al., 2021; Zhu et al., 2017) was selected to establish a baseline before applying a more complex model.
2. Data limitations- Deep learning models need large, labelled datasets for effective training (Li et al., 2023). However, due to limited access to PlanetScope images and its corresponding labelled dataset (created manually) along with ground truth data for validation, this research opted for a supervised machine learning algorithm.
3. Overfitting- Deep learning models can overfit when the training data are not large enough (Safonova et al., 2023). Given the data limitations in this research, the supervised machine learning model was selected. Although cases of overfitting were observed during the analysis, they were addressed by adjusting the hyper-parameters of the model.

After discussing the analysis, the following chapter will present limitations and recommendations followed by the conclusion.

7. RECOMMENDATIONS AND CONCLUSIONS

Section 7.1 outlines the research limitations and suggests recommendations for future work. Section 7.2 offers a concluding remark from the author's perspective.

7.1. Recommendations

The section below lists the limitations of this study with recommendations to address them.

- PlanetScope data and pre-processing: In this research, hyper-temporal images from different areas of interest were acquired. Some individual scenes were made up of images from more than one satellite dove, resulting in geometric and radiometric inconsistencies. This meant that these inconsistencies were present not only between images taken on different dates but also within a single image created by merging multiple images from the same date. Despite PlanetScope images being considered analysis-ready, another round of pre-processing was performed to reduce the differences in the time-series images from the different areas of interest. However, geometric inconsistencies in images persisted in certain cases. Future research with PlanetScope should also focus on utilizing advanced algorithms for more effective pre-processing to enhance the quality of such merged satellite images.
- Building footprint data- As explained in the methodology section, the building footprint data from both OSM and Microsoft did not align accurately with the actual buildings in the scene. After applying a transformation to correct this issue, it was observed that the alignment improved for specific building sets used as references for transformation. However, the same transformation did not work well for many other footprint units, indicating that the alignment issue varied within the dataset. Future work should focus on exploring more building datasets such as Google Open Buildings (based on the area of interest) with minimal issues and utilizing better transformation methods to correct misalignments on a case-by-case basis.
- Grid unit for labelling- The grid unit size selected for this research was 800 m^2, based on the highest recall value (indicating fewer missed damages) observed for damage detection in buildings larger than 500 m^2. The choice of 500 m^2 as the starting point was due to the increased accuracy in damage detection for buildings of this size and above. However, it was also noted that smaller buildings that had completely collapsed were also detected accurately. Table 8 highlights the uncertainty in labelling with larger grid sizes. Therefore, testing smaller grid sizes while comparing the accuracy and recall for damage detection across different building ranges could have led to a better-informed decision on grid size selection.
- Balanced dataset- To create a balanced dataset for binary classification of damage, the number of majority samples ('no damage') was reduced to match the number of minority samples ('damaged'), resulting in a decrease in total number of samples. For multiclass classification for response activities, a weighted approach was used, assigning weights to each minority class proportional to its frequency in the dataset to ensure a balanced representation. This demonstrates inconsistency in the methods used to address the class imbalance between the damage and response activity classification. Future work should aim for a consistent strategy to handle class imbalance while also focusing on not reducing the sample size. For example, over-sampling techniques can be employed to generate synthetic samples. This can also help in generating enough samples to support the application of deep learning algorithms.
- Feature extraction- The choice of selecting texture feature extraction was based on the limited data availability and the need for simpler interpretability of features. Future research should explore the extraction of other relevant features based on shape and colour for improved accuracy (You et al.,

2020). Additionally, deep learning approaches such as CNNs should also be considered, especially when more data becomes available.

- Supervised machine learning- This research employed supervised machine learning due to the limited amount of data. The Random Forest algorithm was selected because it can efficiently handle high-dimensional data generated after feature extraction. Future work should also explore semi-supervised and unsupervised learning approaches like clustering, GAN etc. that do not require large, labelled datasets (Dunphy et al., 2022; Tilon et al., 2020).
- Feature selection- The texture feature selection for different AOIs in Türkiye showed common textures across locations, but there was also variation in the features that were excluded. When aiming for a generalizable classification model, it will be more beneficial to include all the features rather than performing feature selection. This approach can address potential issues arising from the observed variation in texture feature selection, ensuring the model's applicability across different geographical regions.
- Dimensionality reduction- Multispectral images were used directly to extract texture features, followed by Random Forest algorithm for classification, known for its capability to handle high-dimensional data. Therefore, dimensionality reduction was not prioritized. However, similar research focusing on texture feature extraction by Kim et al. (2023) noted that the inter-correlation of multiple texture features can reduce the effectiveness of the model. To address this issue, they used Principal Component Analysis (PCA) to reduce redundant information and enhance the utility of texture features for damage detection. Future work should also incorporate dimensionality reduction techniques to improve the model's performance.
- Generalizability of model- This research focused exclusively on the Türkiye-Syria earthquake, particularly regions from Türkiye. Future research focusing on the generalizability of the model should also incorporate images from multiple locations affected by earthquakes to create a larger dataset for enhanced generalization performance (Zhu et al., 2022). PlanetScope data provides that opportunity with its rich dataset (for events after 2017), especially for events with minimal cloud cover.
- Data integration- PlanetScope image was sharpened with Pleiades image using a High-Pass modulation method. This simpler approach was chosen to demonstrate the synergistic potential of the available dataset. However, advanced sharpening and image fusion techniques, such as the one developed by Shin et al. (2020), have shown both qualitative and quantitative improvements in the generated images using deep learning frameworks. Future work should explore these advanced methods, particularly if the research is not constrained by time and computational resources. Such an integration with available higher-resolution images can also help support direct quantification, for example, the of volume of debris.

7.2. Conclusions

This study aimed to assess the utility of PlanetScope images for post-disaster damage and response assessment, using Türkiye-Syria earthquakes from February 2023 as the case study. The results demonstrate that PlanetScope can be effectively used for grid-based damage detection, identifying zones or regions with completely or partially collapsed buildings. Additionally, calculating damage densities for impacted areas can help identify damage hotspots. Such an analysis can aid emergency responders in prioritizing areas that need immediate attention, ensuring efficient allocation of resources. PlanetScope's spatial coverage and high temporal resolution provide frequent data (near daily images) for any area of interest, that can enable rapid damage assessments, particularly for those disaster events that are not associated with the formation of clouds (that obstruct ground information during image acquisition). For scaling up this methodology, advanced pre-processing, feature extraction and data from diverse locations should be included for a robust model that can be applied to different events, scenarios and geographical locations. Furthermore, the results show that PlanetScope imagery is effective not only for detecting damage but also for response activities, such as the evolution of temporary shelters and debris. This can allow authorities to monitor the construction of shelters and track the timely provision of required support. Accurate detection of debris and spatial distribution of its density can help in prioritizing cleanup efforts. However, it is recommended to establish a baseline in terms of how authorities currently monitor progress and how then satellite-based analyses can complement these existing methods.

The integration of available higher-resolution data, WorldView and Pleiades images, showed multiple practical benefits for improving the comprehensiveness of damage and response assessments. These images were not only used as ground truth for validating the model and confirming the presence of temporary shelters and debris collection sites but also to enhance the details of PlanetScope images using image sharpening techniques. This approach highlights the synergistic potential of freely available satellite images (particularly released to aid humanitarian efforts after a disaster event) with PlanetScope data. By using the available higher-resolution images, the study was able to achieve a more accurate damage assessment. However, the availability of higher-resolution images can be restricted due to their cost, acquisition time and location. These higher-resolution images typically cover smaller areas compared to PlanetScope, which may limit their utility for large-scale assessments, unless multiple images are available. Additionally, the integration test performed for this research was for one specific location for which a high-resolution Pleiades image acquired on the same date and acquisition angle close to that of PlanetScope was available. This made the sharpening process easier. However, integrating data from different sources can be complex due to differences in resolution, acquisition time and angle, image quality etc. which can pose challenges in the integration process. For practical purposes, advanced image fusion techniques that adjust to the variations between different data sources should be explored.

Despite challenges due to data quality, this study demonstrates the significant utility of PlanetScope in large-scale damage and response assessment. While higher-resolution counterparts like WorldView and Pleiades offer superior spatial resolution, their high-cost and limited, on-demand coverage restrict their use for such tasks. PlanetScope, with its more accessible, available and extensive coverage with lower costs, proves to be a valuable source for post-disaster assessments. Its potential should be further explored to support on-ground responding authorities, policymakers and other relevant organizations in effectively managing disaster response efforts.

LIST OF REFERENCES

Abdollahi, A., Pradhan, B., Shukla, N., Chakraborty, S., & Alamri, A. (2020). Deep Learning Approaches Applied to Remote Sensing Datasets for Road Extraction: A State-Of-The-Art Review. *Remote Sensing 2020, Vol. 12, Page 1444*, *12*(9), 1444. https://doi.org/10.3390/RS12091444

Abraham, J., & Wloka, C. (2021). *Edge Detection for Satellite Images without Deep Networks*. https://arxiv.org/abs/2105.12633v1

Adamu, B., Tansey, K., & Ogutu, B. (2018). Remote sensing for detection and monitoring of vegetation affected by oil spills. *International Journal of Remote Sensing*, *39*(11), 3628–3645. https://doi.org/10.1080/01431161.2018.1448483

Adriano, B., Xia, J., Baier, G., Yokoya, N., & Koshimura, S. (2019). Multi-Source Data Fusion Based on Ensemble Learning for Rapid Building Damage Mapping during the 2018 Sulawesi Earthquake and Tsunami in Palu, Indonesia. *Remote Sensing 2019, Vol. 11, Page 886*, *11*(7), 886. https://doi.org/10.3390/RS11070886

Adriano, B., Yokoya, N., Xia, J., & Baier, G. (2021). Big earth observation data processing for disaster damage mapping. *Handbook of Big Geospatial Data*, 99–118. https://doi.org/10.1007/978-3-030-55462-0_4/FIGURES/5

Aimaiti, Y., Sanon, C., Koch, M., Baise, L. G., & Moaveni, B. (2022). War Related Building Damage Assessment in Kyiv, Ukraine, Using Sentinel-1 Radar and Sentinel-2 Optical Images. *Remote Sensing 2022, Vol. 14, Page 6239*, *14*(24), 6239. https://doi.org/10.3390/RS14246239

Airbus. (2012). *Pléiades Imagery User Guide*. https://www.intelligence-airbusds.com/en/8718-user-guides

Airbus. (2013). *SPOT 6/7 Imagery- User Guide*. https://earth.esa.int/eogateway/documents/20142/37627/SPOT-6-7-imagery-user-guide.pdf

Airbus. (2021). *Pléiades Neo User Guide*. https://wp-cdn.apollomapping.com/web_assets/user_uploads/2021/11/08103301/2021.10_PleiadesNeo_UserGuide-EarlyRelease_20211015.pdf

Akbari, E., Boloorani, A. D., Samany, N. N., Hamzeh, S., Soufizadeh, S., & Pignatti, S. (2020). Crop Mapping Using Random Forest and Particle Swarm Optimization based on Multi-Temporal Sentinel-2. *Remote Sensing 2020, Vol. 12, Page 1449*, *12*(9), 1449. https://doi.org/10.3390/RS12091449

Alhaffar, M. B. A., Joury, E., & Eriksson, A. (2023). Community engagement and crowdsourcing for effective disaster response and rescue operations during the earthquake in Syria. *International Journal of Disaster Risk Reduction*, *98*, 104096. https://doi.org/10.1016/J.IJDRR.2023.104096

Alloghani, M., Al-Jumeily, D., Mustafina, J., Hussain, A., & Aljaaf, A. J. (2020). *A Systematic Review on Supervised and Unsupervised Machine Learning Algorithms for Data Science*. 3–21. https://doi.org/10.1007/978-3-030-22475-2_1

Alpyürür, M., & Lav, M. A. (2022). An assessment of probabilistic seismic hazard for the cities in Southwest Turkey using historical and instrumental earthquake catalogs. *Natural Hazards*, *114*(1), 335–365. https://doi.org/10.1007/S11069-022-05392-X/FIGURES/18

Antoniou, V., & Potsiou, C. (2020). A Deep Learning Method to Accelerate the Disaster Response Process. *Remote Sensing 2020, Vol. 12, Page 544*, *12*(3), 544. https://doi.org/10.3390/RS12030544

Arya, D., Maeda, H., Ghosh, S. K., Toshniwal, D., Mraz, A., Kashiyama, T., & Sekimoto, Y. (2020). *Transfer Learning-based Road Damage Detection for Multiple Countries*. https://arxiv.org/abs/2008.13101v1

Axel, C., van Aardt, J. A. N., Aros-Vera, F., & Holguín-Veras, J. (2016). Remote sensing-based detection and quantification of roadway debris following natural disasters. *Laser Radar Technology and Applications XXI*, *9832*, 98320C. https://doi.org/10.1117/12.2223073

Batista, M. H., & Haertel, V. (2010). On the classification of remote sensing high spatial resolution image data. *International Journal of Remote Sensing*, *31*(20), 5533–5548. https://doi.org/10.1080/01431160903485786

Bekkaye, J. H., & Jafari, N. H. (2024). Application and comparison of remote sensing techniques for data-driven disaster debris quantification. *International Journal of Remote Sensing*, *45*(8), 2808–2831. https://doi.org/10.1080/01431161.2024.2339197

Belgiu, M., & Drăgut, L. (2016). Random forest in remote sensing: A review of applications and future directions. *ISPRS Journal of Photogrammetry and Remote Sensing*, *114*, 24–31. https://doi.org/10.1016/J.ISPRSJPRS.2016.01.011

Blanco, A. C. (2022). Typhoon damage mapping using normalized differenced spatial autocorrelation and PlanetScope images. *The International Archives of the Photogrammetry, Remote Sensing and Spatial Information Sciences*, *XLIII-B3-2022*. https://doi.org/10.5194/isprs-archives-XLIII-B3-2022-1077-2022

Boccardo, P., & Tonolo, F. G. (2015). Remote sensing role in emergency mapping for disaster response. *Engineering Geology for Society and Territory - Volume 5: Urban Geology, Sustainable Planning and Landscape Exploitation*, 17–24. https://doi.org/10.1007/978-3-319-09048-1_3/COVER

Bosher, L., Chmutina, K., & van Niekerk, D. (2021). Stop going around in circles: towards a reconceptualisation of disaster risk management phases. *Disaster Prevention and Management: An International Journal*, *30*(4–5), 525–537. https://doi.org/10.1108/DPM-03-2021-0071

Braun, A., Fakhri, F., & Hochschild, V. (2019). Refugee Camp Monitoring and Environmental Change Assessment of Kutupalong, Bangladesh, Based on Radar Imagery of Sentinel-1 and ALOS-2. *Remote Sensing 2019, Vol. 11, Page 2047*, *11*(17), 2047. https://doi.org/10.3390/RS11172047

Cao, M., Ming, D., Xu, L., Fang, J., Liu, L., Ling, X., & Ma, W. (2019). Frequency Spectrum-Based Optimal Texture Window Size Selection for High Spatial Resolution Remote Sensing Image Analysis. *Journal of Spectroscopy*, *2019*. https://doi.org/10.1155/2019/4970376

Cao, Q. D., & Choe, Y. (2020). Building damage annotation on post-hurricane satellite imagery based on convolutional neural networks. *Natural Hazards*, *103*(3), 3357–3376. https://doi.org/10.1007/S11069-020-04133-2/FIGURES/13

Cerbelaud, A., Roupioz, L., Blanchet, G., Breil, P., & Briottet, X. (2021). Supervised classification methods for automatic damage detection caused by heavy rainfall using multi-temporal high resolution optical imagery and auxiliary data. *The International Archives of the Photogrammetry, Remote Sensing and Spatial Information Sciences*, *XLIII-B3-2021*(B3-2021), 693–700. https://doi.org/10.5194/ISPRS-ARCHIVES-XLIII-B3-2021-693-2021

Chen, J., & Cho, Y. K. (2022). CrackEmbed: Point feature embedding for crack segmentation from disaster site point clouds with anomaly detection. *Advanced Engineering Informatics*, *52*. https://doi.org/10.1016/j.aei.2022.101550

Chen, L., Pan, J., Yang, J., & Wang, M. (2024). CS-Net: Deep Multibranch Network Considering Scene Features for Sharpness Assessment of Remote Sensing Images. *IEEE Transactions on Geoscience and Remote Sensing*, *62*, 1–14. https://doi.org/10.1109/TGRS.2024.3377629

Cho, A. Y., Park, S. E., Kim, D. J., Kim, J., Li, C., & Song, J. (2023). Burned Area Mapping Using Unitemporal PlanetScope Imagery With a Deep Learning Based Approach. *IEEE Journal of Selected Topics in Applied Earth Observations and Remote Sensing*, *16*, 242–253. https://doi.org/10.1109/JSTARS.2022.3225070

Christaki, M., Vasilakos, C., Papadopoulou, E. E., Tataris, G., Siarkos, I., & Soulakellis, N. (2022). Building Change Detection Based on a Gray-Level Co-Occurrence Matrix and Artificial Neural Networks. *Drones 2022, Vol. 6, Page 414*, *6*(12), 414. https://doi.org/10.3390/DRONES6120414

Chung, M., Han, Y., & Kim, Y. (2020). A Framework for Unsupervised Wildfire Damage Assessment Using VHR Satellite Images with PlanetScope Data. *Remote Sensing 2020, Vol. 12, Page 3835*, *12*(22), 3835. https://doi.org/10.3390/RS12223835

Cotrufo, S., Sandu, C., Giulio Tonolo, F., & Boccardo, P. (2018). Building damage assessment scale tailored to remote sensing vertical imagery. *European Journal of Remote Sensing*, *51*(1), 991–1005. https://doi.org/10.1080/22797254.2018.1527662

Cumbane, S. P., & Gidófalvi, G. (2019). Review of Big Data and Processing Frameworks for Disaster Response Applications. *ISPRS International Journal of Geo-Information 2019, Vol. 8, Page 387*, *8*(9), 387. https://doi.org/10.3390/IJGI8090387

Dadrass Javan, F., Samadzadegan, F., Mehravar, S., Toosi, A., Khatami, R., & Stein, A. (2021). A review of image fusion techniques for pan-sharpening of high-resolution satellite imagery. *ISPRS Journal of Photogrammetry and Remote Sensing*, *171*, 101–117. https://doi.org/10.1016/J.ISPRSJPRS.2020.11.001

Deng, L., & Wang, Y. (2022). Post-disaster building damage assessment based on improved U-Net. *Scientific Reports 2022 12:1*, *12*(1), 1–13. https://doi.org/10.1038/s41598-022-20114-w

Du, Q., Peng, J., Chen, X., He, Q., He, L., Nie, Q., Zhu, W., Chi, M., Wang, Y., & Wang, C. (2024). *Single-temporal Supervised Remote Change Detection for Domain Generalization*. https://arxiv.org/abs/2404.11326v4

Dunphy, K., Fekri, M. N., Grolinger, K., & Sadhu, A. (2022). Data Augmentation for Deep-Learning-Based Multiclass Structural Damage Detection Using Limited Information. *Sensors 2022, Vol. 22, Page 6193*, *22*(16), 6193. https://doi.org/10.3390/S22166193

El-Kelani, R., & Atatri, A. (2024). Preliminary Analysis of the Aftershock Sequence of the February 6, 2023, Turkey Earthquake. *An-Najah University Journal for Research - A (Natural Sciences)*, *38*(1), 34–41. https://doi.org/10.35552/ANUJR.A.38.1.2148

Erdogan, M., & Yilmaz, A. (2019). Detection of building damage caused by Van Earthquake using image and Digital Surface Model (DSM) difference. *International Journal of Remote Sensing*, *40*(10), 3772–3786. https://doi.org/10.1080/01431161.2018.1552816

EUSI. (2020). *WorldView-4 Data Sheet*. https://www.euspaceimaging.com/wp-content/uploads/WorldView-4-Data-Sheet-2020.pdf

FEMA. (2016). *National Disaster Recovery Framework*. https://www.fema.gov/sites/default/files/2020-06/national_disaster_recovery_framework_2nd.pdf

Filho, C. R. M., do Valle Junior, R. F., de Melo Silva, M. M. A. P., Mendes, R. G., de Souza Rolim, G., Pissarra, T. C. T., de Melo, M. C., Valera, C. A., Pacheco, F. A. L., & Fernandes, L. F. S. (2023). The Accuracy of Land Use and Cover Mapping across Time in Environmental Disaster Zones: The Case of the B1 Tailings Dam Rupture in Brumadinho, Brazil. *Sustainability (Switzerland)*, *15*(8), 6949. https://doi.org/10.3390/SU15086949/S1

Fleming, C. H., & Calabrese, J. M. (2017). A new kernel density estimator for accurate home-range and species-range area estimation. *Methods in Ecology and Evolution*, *8*(5), 571–579. https://doi.org/10.1111/2041-210X.12673

Fontainha, T. C., Leiras, A., Bandeira, R. A. de M., & Scavarda, L. F. (2022). Stakeholder satisfaction in complex relationships during the disaster response: a structured review and a case study perspective. *Production Planning & Control*, *33*(6–7), 517–538. https://doi.org/10.1080/09537287.2020.1834127

Fotiou, K., Argyriou, A. V., Alatza, S., Theocharidis, C., Loupasakis, C., Prodromou, M., Apostolakis, A., Pittaki-Chrysodonta, Z., Kaskara, M., Kontoes, C., Themistocleous, K., Hadjimitsis, D. G., & Tzouvaras, M. (2023). Impact assessment of the catastrophic earthquakes of 6 February 2023 in Turkey and Syria via the exploitation of satellite datasets. *Https://Doi.Org/10.1117/12.2682926*, *12786*, 475–487. https://doi.org/10.1117/12.2682926

Francini, S., McRoberts, R. E., Giannetti, F., Mencucci, M., Marchetti, M., Scarascia Mugnozza, G., & Chirici, G. (2020). Near-real time forest change detection using PlanetScope imagery. *European Journal of Remote Sensing*, *53*(1), 233–244. https://doi.org/10.1080/22797254.2020.1806734

Frazier, A. E., & Hemingway, B. L. (2021). A Technical Review of Planet Smallsat Data: Practical Considerations for Processing and Using PlanetScope Imagery. *Remote Sensing 2021, Vol. 13, Page 3930*, *13*(19), 3930. https://doi.org/10.3390/RS13193930

Friedrich, H. K., & Van Den Hoek, J. (2020). Breaking ground: Automated disturbance detection with Landsat time series captures rapid refugee settlement establishment and growth in North Uganda. *Computers, Environment and Urban Systems*, *82*, 101499. https://doi.org/10.1016/J.COMPENVURBSYS.2020.101499

Fu, X., Kouyama, T., Yang, H., Nakamura, R., & Yoshikawa, I. (2022). Toward Faster and Accurate Post-Disaster Damage Assessment: Development of End-to-End Building Damage Detection Framework with Super-Resolution Architecture. *International Geoscience and Remote Sensing Symposium (IGARSS)*, *2022-July*, 1588–1591. https://doi.org/10.1109/IGARSS46834.2022.9883317

Füreder, P., Lang, S., Rogenhofer, E., Tiede, D., & Papp, A. (2015). Monitoring Displaced People in Crisis Situations Using Multi-temporal VHR Satellite Data During Humanitarian Operations in South Sudan. *Journal for Geographic Information Science*, 391–401. https://doi.org/10.1553/giscience2015s391

Gella, G. W., Wendt, L., Lang, S., Tiede, D., Hofer, B., Gao, Y., & Braun, A. (2022). Mapping of Dwellings in IDP/Refugee Settlements from Very High-Resolution Satellite Imagery Using a Mask Region-Based Convolutional Neural Network. *Remote Sensing*, *14*(3). https://doi.org/10.3390/rs14030689

Gevaert, C., Buunk, T., Van, M. J. C., Homberg, D., Gevaert, C. M., & Van Den Homberg, M. J. C. (2024). Auditing geospatial datasets for biases: using global building datasets for disaster risk management. *Authorea Preprints*. https://doi.org/10.36227/TECHRXIV.170594611.18565119/V1

Ghaffarian, S., & Emtehani, S. (2021). Monitoring Urban Deprived Areas with Remote Sensing and Machine Learning in Case of Disaster Recovery. *Climate 2021, Vol. 9, Page 58*, *9*(4), 58. https://doi.org/10.3390/CLI9040058

Ghaffarian, S., Farhadabad, A. R., & Kerle, N. (2020). Post-Disaster Recovery Monitoring with Google Earth Engine. *Applied Sciences*, *10*(13). https://doi.org/10.3390/APP10134574

Ghaffarian, S., & Kerle, N. (2019). Towards post-disaster debris identification for precise damage and recovery assessments from uav and satellite images. *International Archives of the Photogrammetry, Remote Sensing and Spatial Information Sciences - ISPRS Archives*, *42*(2/W13), 297–302. https://doi.org/10.5194/isprs-archives-XLII-2-W13-297-2019

Ghaffarian, S., Kerle, N., & Filatova, T. (2018). Remote Sensing-Based Proxies for Urban Disaster Risk Management and Resilience: A Review. *Remote Sensing 2018, Vol. 10, Page 1760*, *10*(11), 1760. https://doi.org/10.3390/RS10111760

Ghorbanzadeh, O., Crivellari, A., Tiede, D., Ghamisi, P., & Lang, S. (2022). Mapping Dwellings in IDP/Refugee Settlements Using Deep Learning. *Remote Sensing 2022, Vol. 14, Page 6382*, *14*(24), 6382. https://doi.org/10.3390/RS14246382

Gibson, R. K., Mitchell, A., & Chang, H. C. (2023). Image Texture Analysis Enhances Classification of Fire Extent and Severity Using Sentinel 1 and 2 Satellite Imagery. *Remote Sensing*, *15*(14), 3512. https://doi.org/10.3390/RS15143512/S1

Gohil, V., Dev, S., Upasani, G., Lo, D., Ranganathan, P., & Delimitrou, C. (2024). The Importance of Generalizability in Machine Learning for Systems. *IEEE Computer Architecture Letters*, *23*(1), 95–98. https://doi.org/10.1109/LCA.2024.3384449

Government of Turkey. (2023). *Türkiye earthquakes recovery and reconstruction assessment*. https://reliefweb.int/report/turkiye/turkiye-earthquakes-recovery-and-reconstruction-assessment

Hall-Beyer, M. (2017). *GLCM Texture: A Tutorial v. 3.0 March 2017*. https://doi.org/10.11575/PRISM/33280

Hamilton, D., Gibson, W., Harris, D., & McGath, C. (2023). Evaluation of Multi-Spectral Band Efficacy for Mapping Wildland Fire Burn Severity from PlanetScope Imagery. *Remote Sensing 2023, Vol. 15, Page 5196*, *15*(21), 5196. https://doi.org/10.3390/RS15215196

Havivi, S., Rotman, S. R., Blumberg, D. G., & Maman, S. (2022). Damage Assessment in Rural Environments Following Natural Disasters Using Multi-Sensor Remote Sensing Data. *Sensors 2022, Vol. 22, Page 9998*, *22*(24), 9998. https://doi.org/10.3390/S22249998

He, Y., Jia, Z., Yang, J., & Kasabov, N. K. (2021). Multispectral Image Change Detection Based on Single-Band Slow Feature Analysis. *Remote Sensing 2021, Vol. 13, Page 2969*, *13*(15), 2969. https://doi.org/10.3390/RS13152969

Hegarty-Craver, M., Polly, J., O'Neil, M., Ujeneza, N., Rineer, J., Beach, R. H., Lapidus, D., & Temple, D. S. (2020). Remote Crop Mapping at Scale: Using Satellite Imagery and UAV-Acquired Data as Ground Truth. *Remote Sensing 2020, Vol. 12, Page 1984*, *12*(12), 1984. https://doi.org/10.3390/RS12121984

Hofmann, T. (2001). Unsupervised learning by probabilistic Latent Semantic Analysis. *Machine Learning*, *42*(1–2), 177–196. https://doi.org/10.1023/A:1007617005950/METRICS

Hosseiny, B., Abdi, A. M., & Jamali, S. (2022). Urban land use and land cover classification with interpretable machine learning – A case study using Sentinel-2 and auxiliary data. *Remote Sensing Applications: Society and Environment*, *28*, 100843. https://doi.org/10.1016/J.RSASE.2022.100843

Huang, C., Chen, B., Sun, C., Wang, Y., Zhang, J., Yang, H., Wu, S., Tu, P., Nguyen, M. T., Hong, S., & He, C. (2023). Synergistic Application of Multiple Machine Learning Algorithms and Hyperparameter Optimization Strategies for Net Ecosystem Productivity Prediction in Southeast Asia. *Remote Sensing 2024, Vol. 16, Page 17*, *16*(1), 17. https://doi.org/10.3390/RS16010017

Humeau-Heurtier, A. (2019). Texture feature extraction methods: A survey. *IEEE Access*, *7*, 8975–9000. https://doi.org/10.1109/ACCESS.2018.2890743

IFRC. (2021). *World Disasters Report 2020*. https://media.ifrc.org/ifrc/world-disaster-report-2020

IFRC, National Disaster Reduction Centre of China, & Academy of Disaster Reduction and Emergency Management. (2021). *Global Natural Disaster Assessment Report 2020*. https://www.preventionweb.net/publication/2020-global-natural-disaster-assessment-report

Izadi, M., Mohammadzadeh, A., & Haghighattalab, A. (2017). A New Neuro-Fuzzy Approach for Post-earthquake Road Damage Assessment Using GA and SVM Classification from QuickBird Satellite Images. *Journal of the Indian Society of Remote Sensing*, *45*(6), 965–977. https://doi.org/10.1007/S12524-017-0660-3/TABLES/6

Jakubik, J., Muszynski, M., Vossing, M., Kuhl, N., & Brunschwiler, T. (2023). Toward Foundation Models for Earth Monitoring: Generalizable Deep Learning Models for Natural Hazard Segmentation. *International Geoscience and Remote Sensing Symposium (IGARSS)*, *2023-July*, 5638–5641. https://doi.org/10.1109/IGARSS52108.2023.10282643

Ji, M., Liu, L., Du, R., & Buchroithner, M. F. (2019). A Comparative Study of Texture and Convolutional Neural Network Features for Detecting Collapsed Buildings After Earthquakes Using Pre- and Post-Event Satellite Imagery. *Remote Sensing 2019, Vol. 11, Page 1202*, *11*(10), 1202. https://doi.org/10.3390/RS11101202

Kaplan, G., & Kaplan, O. (2020). PlanetScope Imagery for Extracting Building Inventory Information. *Environmental Sciences Proceedings 2021, Vol. 5, Page 19*, *5*(1), 19. https://doi.org/10.3390/IECG2020-08537

Kazmi, S. S. A., Ahmed, M., Mumtaz, R., & Anwar, Z. (2022). Spatiotemporal Clustering and Analysis of Road Accident Hotspots by Exploiting GIS Technology and Kernel Density Estimation. *The Computer Journal*, *65*(2), 155–176. https://doi.org/10.1093/COMJNL/BXZ158

Kedia, T., Ratcliff, J., O'Connor, M., Oluic, S., Rose, M., Freeman, J., & Rainwater-Lovett, K. (2022). Technologies Enabling Situational Awareness During Disaster Response: A Systematic Review. *Disaster Medicine and Public Health Preparedness*, *16*(1), 341–359. https://doi.org/10.1017/DMP.2020.196

Khatami, R., Mountrakis, G., & Stehman, S. V. (2017). Mapping per-pixel predicted accuracy of classified remote sensing images. *Remote Sensing of Environment*, *191*, 156–167. https://doi.org/10.1016/J.RSE.2017.01.025

Khodaverdizahraee, N., Rastiveis, H., & Jouybari, A. (2020). Segment-by-segment comparison technique for earthquake-induced building damage map generation using satellite imagery. *International Journal of Disaster Risk Reduction*, *46*, 101505. https://doi.org/10.1016/J.IJDRR.2020.101505

Kim, M., Park, S. E., & Lee, S. J. (2023). Detection of Damaged Buildings Using Temporal SAR Data with Different Observation Modes. *Remote Sensing 2023, Vol. 15, Page 308*, *15*(2), 308. https://doi.org/10.3390/RS15020308

Kumar, B., Dikshit, O., Gupta, A., & Singh, M. K. (2020). Feature extraction for hyperspectral image classification: a review. *International Journal of Remote Sensing*, *41*(16), 6248–6287. https://doi.org/10.1080/01431161.2020.1736732

Kupidura, P. (2019). The Comparison of Different Methods of Texture Analysis for Their Efficacy for Land Use Classification in Satellite Imagery. *Remote Sensing 2019, Vol. 11, Page 1233*, *11*(10), 1233. https://doi.org/10.3390/RS11101233

Kussul, N., Drozd, S., Skakun, S., Duncan, E., & Becker-Reshef, I. (2024). *Fusion of very high and moderate spatial resolution satellite data for detection and mapping of damages in agricultural fields*. 1–7. https://doi.org/10.1109/DESSERT61349.2023.10416533

Labiak, R. C., Aardt, J. A. N. van, Bespalov, D., Eychner, D., Wirch, E., & Bischof, H.-P. (2011). Automated method for detection and quantification of building damage and debris using post-disaster lidar data. *Https://Doi.Org/10.1117/12.883509*, *8037*, 145–152. https://doi.org/10.1117/12.883509

Latte, N., & Lejeune, P. (2020). PlanetScope Radiometric Normalization and Sentinel-2 Super-Resolution (2.5 m): A Straightforward Spectral-Spatial Fusion of Multi-Satellite Multi-Sensor Images Using Residual Convolutional Neural Networks. *Remote Sensing 2020, Vol. 12, Page 2366*, *12*(15), 2366. https://doi.org/10.3390/RS12152366

Le, K. G., Liu, P., & Lin, L. T. (2022). Traffic accident hotspot identification by integrating kernel density estimation and spatial autocorrelation analysis: a case study. *International Journal of Crashworthiness*, *27*(2), 543–553. https://doi.org/10.1080/13588265.2020.1826800

Leach, N. R., Popien, P., Goodman, M. C., & Tellman, B. (2022). Leveraging convolutional neural networks for semantic segmentation of global floods with PlanetScope imagery. *International Geoscience and Remote Sensing Symposium (IGARSS)*, *2022-July*, 314–317. https://doi.org/10.1109/IGARSS46834.2022.9884272

Li, H., Cui, J., Zhang, X., Han, Y., & Cao, L. (2022). Dimensionality Reduction and Classification of Hyperspectral Remote Sensing Image Feature Extraction. *Remote Sensing 2022, Vol. 14, Page 4579*, *14*(18), 4579. https://doi.org/10.3390/RS14184579

Li, W., He, C., Fang, J., Zheng, J., Fu, H., & Yu, L. (2019). Semantic Segmentation-Based Building Footprint Extraction Using Very High-Resolution Satellite Images and Multi-Source GIS Data. *Remote Sensing 2019, Vol. 11, Page 403*, *11*(4), 403. https://doi.org/10.3390/RS11040403

Li, Y., Li, X., Zhang, Y., Peng, D., & Bruzzone, L. (2023). Cost-efficient information extraction from massive remote sensing data: When weakly supervised deep learning meets remote sensing big data. *International Journal of Applied Earth Observation and Geoinformation*, *120*, 103345. https://doi.org/10.1016/J.JAG.2023.103345

Li, Y., Tang, X., Tian, T., Zhu, Z., Usmani, M., Bovolo, F., & Napolitano, M. (2023). Remote Sensing and Deep Learning to Understand Noisy OpenStreetMap. *Remote Sensing 2023, Vol. 15, Page 4639*, *15*(18), 4639. https://doi.org/10.3390/RS15184639

Li, Z., Zhang, H. K., Roy, D. P., Yan, L., & Huang, H. (2020). Sharpening the Sentinel-2 10 and 20 m Bands to Planetscope-0 3 m Resolution. *Remote Sensing 2020, Vol. 12, Page 2406*, *12*(15), 2406. https://doi.org/10.3390/RS12152406

Liping, C., Yujun, S., & Saeed, S. (2018). Monitoring and predicting land use and land cover changes using remote sensing and GIS techniques—A case study of a hilly area, Jiangle, China. *PLOS ONE*, *13*(7), e0200493. https://doi.org/10.1371/JOURNAL.PONE.0200493

Liu, C., Sepasgozar, S. M. E., Zhang, Q., & Ge, L. (2022). A novel attention-based deep learning method for post-disaster building damage classification. *Expert Systems with Applications*, *202*, 117268. https://doi.org/10.1016/J.ESWA.2022.117268

Liu, C., Zhang, H., Pan, Y., -, al, Brandoli Machado, B., Nunes Gonçalves, W., & Martinez Bruno -, O. (2021). Research Progress in Remote Sensing Image Texture Analysis. *Journal of Physics: Conference Series*, *1961*(1), 012028. https://doi.org/10.1088/1742-6596/1961/1/012028

Liu, R., Kuffer, M., & Persello, C. (2019). The Temporal Dynamics of Slums Employing a CNN-Based Change Detection Approach. *Remote Sensing 2019, Vol. 11, Page 2844*, *11*(23), 2844. https://doi.org/10.3390/RS11232844

Liu, R., Zhu, W., & Yang, X. (2023). Screening Image Features of Collapsed Buildings for Operational and Rapid Remote Sensing Identification. *Remote Sensing 2023, Vol. 15, Page 5747*, *15*(24), 5747. https://doi.org/10.3390/RS15245747

Loo, B. P. Y., Yao, S., & Wu, J. (2011). Spatial point analysis of road crashes in Shanghai: A GIS-based network kernel density method. *Proceedings - 2011 19th International Conference on Geoinformatics, Geoinformatics 2011*. https://doi.org/10.1109/GEOINFORMATICS.2011.5980938

Lubin, A., & Saleem, A. (2019). Remote sensing-based mapping of the destruction to Aleppo during the Syrian Civil War between 2011 and 2017. *Applied Geography*, *108*, 30–38. https://doi.org/10.1016/J.APGEOG.2019.05.004

Lunga, D., Arndt, J., Gerrand, J., & Stewart, R. (2021). ReSFlow: A Remote Sensing Imagery Data-Flow for Improved Model Generalization. *IEEE Journal of Selected Topics in Applied Earth Observations and Remote Sensing*, *14*, 10468–10483. https://doi.org/10.1109/JSTARS.2021.3119001

Luo, H., Liu, C., Wu, C., & Guo, X. (2018). Urban Change Detection Based on Dempster–Shafer Theory for Multitemporal Very High-Resolution Imagery. *Remote Sensing 2018, Vol. 10, Page 980*, *10*(7), 980. https://doi.org/10.3390/RS10070980

Maghsoudi, A., & Moshtari, M. (2021). Challenges in disaster relief operations: evidence from the 2017 Kermanshah earthquake. *Journal of Humanitarian Logistics and Supply Chain Management*, *11*(1), 107–134. https://doi.org/10.1108/JHLSCM-08-2019-0054/FULL/PDF

Mason, R. E., Vaughn, N. R., & Asner, G. P. (2023). Mapping Buildings across Heterogeneous Landscapes: Machine Learning and Deep Learning Applied to Multi-Modal Remote Sensing Data. *Remote Sensing 2023, Vol. 15, Page 4389*, *15*(18), 4389. https://doi.org/10.3390/RS15184389

Mavroulis, S., Mavrouli, M., Vassilakis, E., Argyropoulos, I., Carydis, P., & Lekkas, E. (2023). Debris Management in Turkey Provinces Affected by the 6 February 2023 Earthquakes: Challenges during Recovery and Potential Health and Environmental Risks. *Applied Sciences 2023, Vol. 13, Page 8823*, *13*(15), 8823. https://doi.org/10.3390/APP13158823

MAXAR. (2020). *GeoEye-1 Data Sheet*. http://content.satimagingcorp.com.s3.amazonaws.com/static/satellite-sensor-specification/GeoEye-1-PDF-Download.pdf

Maxwell, A. E., Warner, T. A., & Fang, F. (2018). Implementation of machine-learning classification in remote sensing: an applied review. *International Journal of Remote Sensing*, *39*(9), 2784–2817. https://doi.org/10.1080/01431161.2018.1433343

Mei, X., Pan, E., Ma, Y., Dai, X., Huang, J., Fan, F., Du, Q., Zheng, H., & Ma, J. (2019). A Random Forest Machine Learning Approach for the Retrieval of Leaf Chlorophyll Content in Wheat. *Remote Sensing 2019, Vol. 11, Page 920*, *11*(8), 920. https://doi.org/10.3390/RS11080920

Meng, X., Shen, H., Li, H., Zhang, L., & Fu, R. (2019). Review of the pansharpening methods for remote sensing images based on the idea of meta-analysis: Practical discussion and challenges. *Information Fusion*, *46*, 102–113. https://doi.org/10.1016/J.INFFUS.2018.05.006

Metzger, P., Robert, J., & Sierra, A. (2014). A Geographical Approach to Disaster Management: Analyzing Vulnerability in Relation to Decision and Intervention Resources in Lima and Callao. *International Journal of Mass Emergencies & Disasters*, *32*(1), 26–42. https://doi.org/10.1177/028072701403200102

Miura, H. (2019). Fusion Analysis of Optical Satellite Images and Digital Elevation Model for Quantifying Volume in Debris Flow Disaster. *Remote Sensing 2019, Vol. 11, Page 1096*, *11*(9), 1096. https://doi.org/10.3390/RS11091096

Mudau, N., & Mhangara, P. (2022). Towards understanding informal settlement growth patterns: Contribution to SDG reporting and spatial planning. *Remote Sensing Applications: Society and Environment*, *27*, 100801. https://doi.org/10.1016/J.RSASE.2022.100801

Muhammad, M., Williams-Jones, G., Stead, D., Tortini, R., Falorni, G., & Donati, D. (2022). Applications of Image-Based Computer Vision for Remote Surveillance of Slope Instability. *Frontiers in Earth Science*, *10*, 909078. https://doi.org/10.3389/FEART.2022.909078/BIBTEX

National Research Council. (2006). Facing Hazards and Disasters. In *Facing Hazards and Disasters*. National Academies Press. https://doi.org/10.17226/11671

Nex, F., Duarte, D., Tonolo, F. G., & Kerle, N. (2019). Structural Building Damage Detection with Deep Learning: Assessment of a State-of-the-Art CNN in Operational Conditions. *Remote Sensing 2019, Vol. 11, Page 2765*, *11*(23), 2765. https://doi.org/10.3390/RS11232765

Norris, F. H., Stevens, S. P., Pfefferbaum, B., Wyche, K. F., & Pfefferbaum, R. L. (2008). Community resilience as a metaphor, theory, set of capacities, and strategy for disaster readiness. *American Journal of Community Psychology*, *41*(1–2), 127–150. https://doi.org/10.1007/S10464-007-9156-6/FIGURES/2

Oden, R. V. N., Militello, L. G., Ross, K. G., & Lopez, C. E. (2012). Four key challenges in disaster response. *Proceedings of the Human Factors and Ergonomics Society*, 488–492. https://doi.org/10.1177/1071181312561050

Olorunfemi, I. E., Fasinmirin, J. T., Olufayo, A. A., & Komolafe, A. A. (2020). GIS and remote sensing-based analysis of the impacts of land use/land cover change (LULCC) on the environmental sustainability of Ekiti State, southwestern Nigeria. *Environment, Development and Sustainability*, *22*(2), 661–692. https://doi.org/10.1007/S10668-018-0214-Z/FIGURES/13

Omarzadeh, D., Karimzadeh, S., Matsuoka, M., & Feizizadeh, B. (2021). Earthquake Aftermath from Very High-Resolution WorldView-2 Image and Semi-Automated Object-Based Image Analysis (Case Study: Kermanshah, Sarpol-e Zahab, Iran). *Remote Sensing 2021, Vol. 13, Page 4272*, *13*(21), 4272. https://doi.org/10.3390/RS13214272

OpenCV. (n.d.). *OpenCV: Canny Edge Detection*. 2024. Retrieved June 12, 2024, from https://docs.opencv.org/4.x/da/d22/tutorial_py_canny.html

Pal, M. (2005). Random forest classifier for remote sensing classification. *International Journal of Remote Sensing*, *26*(1), 217–222. https://doi.org/10.1080/01431160412331269698

Patwary, M. M., Ashraf, S., Swed, S., & Shoib, S. (2023). The Impact of the Devastating Turkey-Syria Earthquake on the Fragile Health Care System in War-Torn Syria. *Prehospital and Disaster Medicine*, *38*(4), 537–538. https://doi.org/10.1017/S1049023X23005903

Pickering, J., Tyukavina, A., Lima, A., Khan, A., Potapov, P., Adusei, B., & Hansen, M. C. (2021). Using Multi-Resolution Satellite Data to Quantify Land Dynamics: Applications of PlanetScope Imagery for Cropland and Tree-Cover Loss Area Estimation. *Remote Sensing 2021, Vol. 13, Page 2191*, *13*(11), 2191. https://doi.org/10.3390/RS13112191

Pirrone, D., Bovolo, F., & Bruzzone, L. (2020). An Approach to Unsupervised Detection of Fully and Partially Destroyed Buildings in Multitemporal VHR SAR Images. *IEEE Journal of Selected Topics in Applied Earth Observations and Remote Sensing*, *13*, 5938–5953. https://doi.org/10.1109/JSTARS.2020.3026838

Planet Labs. (2022). *Planet imagery product specifications*. https://assets.planet.com/docs/Planet_Combined_Imagery_Product_Specs_letter_screen.pdf

Pollino, M., Cappucci, S., Giordano, L., Iantosca, D., De Cecco, L., Bersan, D., Rosato, V., & Borfecchia, F. (2020). Assessing Earthquake-Induced Urban Rubble by Means of Multiplatform Remotely Sensed Data. *ISPRS International Journal of Geo-Information 2020, Vol. 9, Page 262*, *9*(4), 262. https://doi.org/10.3390/IJGI9040262

Pyo, J. C., Han, K. J., Cho, Y., Kim, D., & Jin, D. (2022). Generalization of U-Net Semantic Segmentation for Forest Change Detection in South Korea Using Airborne Imagery. *Forests 2022, Vol. 13, Page 2170*, *13*(12), 2170. https://doi.org/10.3390/F13122170

Quan, Y., Zhong, X., Feng, W., Dauphin, G., Gao, L., & Xing, M. (2020). A Novel Feature Extension Method for the Forest Disaster Monitoring Using Multispectral Data. *Remote Sensing 2020, Vol. 12, Page 2261*, *12*(14), 2261. https://doi.org/10.3390/RS12142261

Ramezan, C. A., Warner, T. A., Maxwell, A. E., & Price, B. S. (2021). Effects of Training Set Size on Supervised Machine-Learning Land-Cover Classification of Large-Area High-Resolution Remotely Sensed Data. *Remote Sensing 2021, Vol. 13, Page 368*, *13*(3), 368. https://doi.org/10.3390/RS13030368

Rogova, G. L., Scott, P. D., Lollett, C., & Mudiyanur, R. (2006). Reasoning about situations in the early post-disaster response environment. *2006 9th International Conference on Information Fusion, FUSION*. https://doi.org/10.1109/ICIF.2006.301643

Rolf, E., Proctor, J., Carleton, T., Bolliger, I., Shankar, V., Ishihara, M., Recht, B., & Hsiang, S. (2021). A generalizable and accessible approach to machine learning with global satellite imagery. *Nature Communications 2021 12:1*, *12*(1), 1–11. https://doi.org/10.1038/s41467-021-24638-z

Román, M. O., Stokes, E. C., Shrestha, R., Wang, Z., Schultz, L., Sepúlveda Carlo, E. A., Sun, Q., Bell, J., Molthan, A., Kalb, V., Ji, C., Seto, K. C., McClain, S. N., & Enenkel, M. (2019). Satellite-based assessment of electricity restoration efforts in Puerto Rico after Hurricane Maria. *PLOS ONE*, *14*(6), e0218883. https://doi.org/10.1371/JOURNAL.PONE.0218883

Roy, D. P., Huang, H., Houborg, R., & Martins, V. S. (2021). A global analysis of the temporal availability of PlanetScope high spatial resolution multi-spectral imagery. *Remote Sensing of Environment*, *264*, 112586. https://doi.org/10.1016/J.RSE.2021.112586

Saffarzadeh, A., Shimaoka, T., Nakayama, H., Hanashima, T., Yamaguchi, K., & Manabe, K. (2017). Tasks and problems involved in the handling of disaster waste upon April 2016 Kumamoto Earthquake, Japan. *Natural Hazards*, *89*(3), 1273–1290. https://doi.org/10.1007/S11069-017-3021-1/TABLES/1

Safonova, A., Ghazaryan, G., Stiller, S., Main-Knorn, M., Nendel, C., & Ryo, M. (2023). Ten deep learning techniques to address small data problems with remote sensing. *International Journal of Applied Earth Observation and Geoinformation*, *125*, 103569. https://doi.org/10.1016/J.JAG.2023.103569

Salau, A. O., & Jain, S. (2019). Feature Extraction: A Survey of the Types, Techniques, Applications. *2019 International Conference on Signal Processing and Communication, ICSC 2019*, 158–164. https://doi.org/10.1109/ICSC45622.2019.8938371

Samper, J., Shelby, J. A., & Behary, D. (2020). The Paradox of Informal Settlements Revealed in an ATLAS of Informality: Findings from Mapping Growth in the Most Common Yet Unmapped Forms of Urbanization. *Sustainability 2020, Vol. 12, Page 9510*, *12*(22), 9510. https://doi.org/10.3390/SU12229510

Santra, A., Santra Mitra, S., Mitra, D., & Sarkar, A. (2019). Relative Radiometric Normalisation - performance testing of selected techniques and impact analysis on vegetation and water bodies. *Geocarto International*, *34*(1), 98–113. https://doi.org/10.1080/10106049.2017.1367424

SatSummit. (2015, November 23). *State of Satellite Imagery*. https://landscape.satsummit.io/capture/resolution-considerations.html

Schaeffer, B. A., Whitman, P., Conmy, R., Salls, W., Coffer, M., Graybill, D., & Lebrasse, M. C. (2022). Potential for commercial PlanetScope satellites in oil response monitoring. *Marine Pollution Bulletin*, *183*, 114077. https://doi.org/10.1016/J.MARPOLBUL.2022.114077

Serifoglu Yilmaz, C., Yilmaz, V., Tansey, K., & Aljehani, N. S. O. (2023). Automated detection of damaged buildings in post-disaster scenarios: a case study of Kahramanmaraş (Türkiye) earthquakes on February 6, 2023. *Natural Hazards*, 1–25. https://doi.org/10.1007/S11069-023-06154-Z/TABLES/3

Seydi, S. T., Hasanlou, M., Chanussot, J., & Ghamisi, P. (2023). BDD-Net+: A Building Damage Detection Framework Based on Modified Coat-Net. *IEEE Journal of Selected Topics in Applied Earth Observations and Remote Sensing*, *16*, 4232–4247. https://doi.org/10.1109/JSTARS.2023.3267847

Shafique, A., Cao, G., Khan, Z., Asad, M., & Aslam, M. (2022). Deep Learning-Based Change Detection in Remote Sensing Images: A Review. *Remote Sensing 2022, Vol. 14, Page 871*, *14*(4), 871. https://doi.org/10.3390/RS14040871

Shafique, K., & Warren, C. M. J. (2016). Stakeholders and Their Significance in Post Natural Disaster Reconstruction Projects: A Systematic Review of the Literature. *Asian Social Science*, *12*(10). https://doi.org/10.5539/ass.v12n10p1

Shi, D., & Yang, X. (2016). An assessment of algorithmic parameters affecting image classification accuracy by random forests. *Photogrammetric Engineering and Remote Sensing*, *82*(6), 407–417. https://doi.org/10.14358/PERS.82.6.407

Shin, C., Kim, S., & Kim, Y. (2020). From Planetscope to Worldview: Micro-Satellite Image Super-Resolution with Optimal Transport Distance. *Proceedings - International Conference on Image Processing, ICIP*, *2020-October*, 898–902. https://doi.org/10.1109/ICIP40778.2020.9190810

Shuo, Z., Jingyu, Z., Zhengxiang, Z., & Jianjun, Z. (2021). Identifying the density of grassland fire points with kernel density estimation based on spatial distribution characteristics. *Open Geosciences*, *13*(1), 796–806. https://doi.org/10.1515/GEO-2020-0265/DOWNLOADASSET/SUPPL/GEO-2020-0265_SM.PDF

Sonobe, M. (2020). *Characteristics of texture index of damaged buildings using time-series high-resolution optical satellite images*. https://doi.org/10.5194/isprs-archives-XLIII-B3-2020-1709-2020

Spasenovic, K., & Carrion, D. (2019). Quality check of crisis maps produced over five years by Copernicus EMS. *ISPRS Geospatial Week 2019*, *XLII-2/W13*. https://doi.org/10.5194/isprs-archives-XLII-2-W13-1263-2019

Stone, C., & Mohammed, C. (2017). Application of Remote Sensing Technologies for Assessing Planted Forests Damaged by Insect Pests and Fungal Pathogens: a Review. *Current Forestry Reports*, *3*(2), 75–92. https://doi.org/10.1007/S40725-017-0056-1/FIGURES/1

Syifa, M., Kadavi, P. R., & Lee, C. W. (2019). An Artificial Intelligence Application for Post-Earthquake Damage Mapping in Palu, Central Sulawesi, Indonesia. *Sensors 2019, Vol. 19, Page 542*, *19*(3), 542. https://doi.org/10.3390/S19030542

Szpakowski, D. M., & Jensen, J. L. R. (2019). A Review of the Applications of Remote Sensing in Fire Ecology. *Remote Sensing 2019, Vol. 11, Page 2638*, *11*(22), 2638. https://doi.org/10.3390/RS11222638

Tavus, B., Kocaman, S., & Gokceoglu, C. (2022). Flood damage assessment with Sentinel-1 and Sentinel-2 data after Sardoba dam break with GLCM features and Random Forest method. *Science of The Total Environment*, *816*, 151585. https://doi.org/10.1016/J.SCITOTENV.2021.151585

Thakali, L., Kwon, T. J., & Fu, L. (2015). Identification of crash hotspots using kernel density estimation and kriging methods: a comparison. *Journal of Modern Transportation*, *23*(2), 93–106. https://doi.org/10.1007/S40534-015-0068-0/FIGURES/10

The World Bank, & GFDRR. (2023). *Global Rapid Post-Disaster Damage Estimation (GRADE) Report*. https://documents.worldbank.org/en/publication/documents-reports/documentdetail/099022723021250141/p1788430aeb62f08009b2302bd4074030fb

Tilon, S., Nex, F., Kerle, N., & Vosselman, G. (2020). Post-Disaster Building Damage Detection from Earth Observation Imagery Using Unsupervised and Transferable Anomaly Detecting Generative Adversarial Networks. *Remote Sensing 2020, Vol. 12, Page 4193*, *12*(24), 4193. https://doi.org/10.3390/RS12244193

Todd, D., & Todd, H. (2011). *Natural Disaster Response Lessons from Evaluations of the World Bank and Others*. http://hdl.handle.net/10986/27353

Tomaszewski, B., Judex, M., Szarzynski, J., Radestock, C., & Wirkus, L. (2015). Geographic Information Systems for Disaster Response: A Review. *Journal of Homeland Security and Emergency Management*, *12*(3), 571–602. https://doi.org/10.1515/JHSEM-2014-0082/MACHINEREADABLECITATION/RIS

Tong, X., Hong, Z., Liu, S., Zhang, X., Xie, H., Li, Z., Yang, S., Wang, W., & Bao, F. (2012). Building-damage detection using pre- and post-seismic high-resolution satellite stereo imagery: A case study of the May 2008 Wenchuan earthquake. *ISPRS Journal of Photogrammetry and Remote Sensing*, *68*(1), 13–27. https://doi.org/10.1016/J.ISPRSJPRS.2011.12.004

Ullah, T., Lautenbach, S., Herfort, B., Reinmuth, M., & Schorlemmer, D. (2023). Assessing Completeness of OpenStreetMap Building Footprints Using MapSwipe. *ISPRS International Journal of Geo-Information 2023, Vol. 12, Page 143*, *12*(4), 143. https://doi.org/10.3390/IJGI12040143

UNDRR. (2013). *Report of the open-ended intergovernmental expert working group on indicators and terminology relating to disaster risk reduction*. https://www.undrr.org/publication/report-open-ended-intergovernmental-expert-working-group-indicators-and-terminology

UNDRR. (2022). *Global Assessment Report on Disaster Risk Reduction 2022*. https://www.undrr.org/gar/gar2022-our-world-risk-gar

UNISDR. (2015). *Sendai Framework for Disaster Risk Reduction 2015-2030*. https://www.undrr.org/quick/11409

Uwishema, O. (2023). Addressing the effects of the earthquakes on Türkiye's health-care system. *The Lancet*, *401*(10378), 727. https://doi.org/10.1016/S0140-6736(23)00326-4

Valentijn, T. (2020). *The Practical Applicability of a CNN for Automated Building Damage Assessment* [Aalto University]. https://aaltodoc.aalto.fi/server/api/core/bitstreams/b20ecf34-ace1-409e-a395-59dc66291921/content

Valentijn, T., Margutti, J., van den Homberg, M., & Laaksonen, J. (2020). Multi-Hazard and Spatial Transferability of a CNN for Automated Building Damage Assessment. *Remote Sensing 2020, Vol. 12, Page 2839*, *12*(17), 2839. https://doi.org/10.3390/RS12172839

Verschoor, M. A. F. (2022). *The impact of spatial resolution and satellite data type characteristics on Automated Damage Assessment using a Convolutional Neural Network* [Delft University of Technology]. https://repository.tudelft.nl/islandora/object/uuid%3A65f73194-d045-430b-8112-5b8cf27d7293

Vetrivel, A., Gerke, M., Kerle, N., Nex, F., & Vosselman, G. (2018). Disaster damage detection through synergistic use of deep learning and 3D point cloud features derived from very high resolution oblique aerial images, and multiple-kernel-learning. *ISPRS Journal of Photogrammetry and Remote Sensing*, *140*, 45–59. https://doi.org/10.1016/J.ISPRSJPRS.2017.03.001

Virtriana, R., Harto, A. B., Atmaja, F. W., Meilano, I., Fauzan, K. N., Anggraini, T. S., Ihsan, K. T. N., Mustika, F. C., & Suminar, W. (2023). Machine learning remote sensing using the random forest classifier to detect the building damage caused by the Anak Krakatau Volcano tsunami. *Geomatics, Natural Hazards and Risk*, *14*(1), 28–51. https://doi.org/10.1080/19475705.2022.2147455

Vizzari, M. (2022). PlanetScope, Sentinel-2, and Sentinel-1 Data Integration for Object-Based Land Cover Classification in Google Earth Engine. *Remote Sensing*, *14*(11), 2628. https://doi.org/10.3390/RS14112628/S1

Wang, J., Yang, M., Chen, Z., Lu, J., & Zhang, L. (2022). An MLC and U-Net Integrated Method for Land Use/Land Cover Change Detection Based on Time Series NDVI-Composed Image from PlanetScope Satellite. *Water 2022, Vol. 14, Page 3363*, *14*(21), 3363. https://doi.org/10.3390/W14213363

Wang, Q., Zhao, R., & Wang, N. (2024). Spatially non-stationarity relationships between high-density built environment and waterlogging disaster: Insights from xiamen island, china. *Ecological Indicators*, *162*, 112021. https://doi.org/10.1016/J.ECOLIND.2024.112021

Wang, Z., Ginzler, C., & Waser, L. T. (2020). Assessing structural changes at the forest edge using kernel density estimation. *Forest Ecology and Management*, *456*, 117639. https://doi.org/10.1016/J.FORECO.2019.117639

Wei, D., & Yang, W. (2020). Detecting damaged buildings using a texture feature contribution index from post-earthquake remote sensing images. *Remote Sensing Letters*, *11*(2), 127–136. https://doi.org/10.1080/2150704X.2019.1692389

Wu, C., Zhang, F., Xia, J., Xu, Y., Li, G., Xie, J., Du, Z., & Liu, R. (2021). Building Damage Detection Using U-Net with Attention Mechanism from Pre- and Post-Disaster Remote Sensing Datasets. *Remote Sensing 2021, Vol. 13, Page 905*, *13*(5), 905. https://doi.org/10.3390/RS13050905

Xie, Y., Feng, D., Chen, H., Liu, Z., Mao, W., Zhu, J., Hu, Y., & Baik, S. W. (2022). Damaged Building Detection from Post-Earthquake Remote Sensing Imagery Considering Heterogeneity Characteristics. *IEEE Transactions on Geoscience and Remote Sensing*, *60*. https://doi.org/10.1109/TGRS.2022.3200872

Xu, X., Chen, Y., Zhang, J., Chen, Y., Anandhan, P., & Manickam, A. (2021). A novel approach for scene classification from remote sensing images using deep learning methods. *European Journal of Remote Sensing*, *54*(sup2), 383–395. https://doi.org/10.1080/22797254.2020.1790995

Yang, J., Hou, H., & Hu, H. (2024). Exploring the Intelligent Emergency Management Mode of Rural Natural Disasters in the Era of Digital Technology. *Sustainability 2024, Vol. 16, Page 2366*, *16*(6), 2366. https://doi.org/10.3390/SU16062366

Yang, L., Chen, Y., Song, S., Li, F., & Huang, G. (2021). Deep Siamese Networks Based Change Detection with Remote Sensing Images. *Remote Sensing 2021, Vol. 13, Page 3394*, *13*(17), 3394. https://doi.org/10.3390/RS13173394

Ye, Y., Jiao, W., & Yan, H. (2020). Managing Relief Inventories Responding to Natural Disasters: Gaps Between Practice and Literature. *Production and Operations Management*, *29*(4), 807–832. https://doi.org/10.1111/POMS.13136

You, Y., Cao, J., & Zhou, W. (2020). A Survey of Change Detection Methods Based on Remote Sensing Images for Multi-Source and Multi-Objective Scenarios. *Remote Sensing 2020, Vol. 12, Page 2460*, *12*(15), 2460. https://doi.org/10.3390/RS12152460

You, Y., Wang, S., Ma, Y., Chen, G., Wang, B., Shen, M., & Liu, W. (2018). Building Detection from VHR Remote Sensing Imagery Based on the Morphological Building Index. *Remote Sensing*, *10*(8). https://doi.org/10.3390/RS10081287

Zhang, H., Li, Q., Liu, J., Shang, J., Du, X., McNairn, H., Champagne, C., Dong, T., & Liu, M. (2017). Image Classification Using RapidEye Data: Integration of Spectral and Textual Features in a Random Forest Classifier. *IEEE Journal of Selected Topics in Applied Earth Observations and Remote Sensing*, *10*(12), 5334–5349. https://doi.org/10.1109/JSTARS.2017.2774807

Zhang, K., Zhang, F., Wan, W., Yu, H., Sun, J., Del Ser, J., Elyan, E., & Hussain, A. (2023). Panchromatic and multispectral image fusion for remote sensing and earth observation: Concepts, taxonomy, literature review, evaluation methodologies and challenges ahead. *Information Fusion*, *93*, 227–242. https://doi.org/10.1016/J.INFFUS.2022.12.026

Zhang, X., Cui, J., Wang, W., & Lin, C. (2017). A Study for Texture Feature Extraction of High-Resolution Satellite Images Based on a Direction Measure and Gray Level Co-Occurrence Matrix Fusion Algorithm. *Sensors 2017, Vol. 17, Page 1474*, *17*(7), 1474. https://doi.org/10.3390/S17071474

Zhao, K., Liu, J., Wang, Q., Wu, X., & Tu, J. (2022). Road Damage Detection From Post-Disaster High-Resolution Remote Sensing Images Based on TLD Framework. *IEEE Access*, *10*, 43552–43561. https://doi.org/10.1109/ACCESS.2022.3169031

Zhou, Z., Zheng, C., Liu, X., Tian, Y., Chen, X., Chen, X., & Dong, Z. (2023). A Dynamic Effective Class Balanced Approach for Remote Sensing Imagery Semantic Segmentation of Imbalanced Data. *Remote Sensing 2023, Vol. 15, Page 1768*, *15*(7), 1768. https://doi.org/10.3390/RS15071768

Zhu, Q., Guo, X., Deng, W., Guan, Q., Zhong, Y., Zhang, L., & Li, D. (2022). Land-Use/Land-Cover change detection based on a Siamese global learning framework for high spatial resolution remote sensing imagery. *ISPRS Journal of Photogrammetry and Remote Sensing*, *184*, 63–78. https://doi.org/10.1016/J.ISPRSJPRS.2021.12.005

Zhu, X. X., Tuia, D., Mou, L., Xia, G. S., Zhang, L., Xu, F., & Fraundorfer, F. (2017). Deep Learning in Remote Sensing: A Comprehensive Review and List of Resources. *IEEE Geoscience and Remote Sensing Magazine*, *5*(4), 8–36. https://doi.org/10.1109/MGRS.2017.2762307

8. ANNEX

Annex 1- Comparison of high-resolution satellite characteristics

The following table shows the characteristics of different high-resolution satellites.

Table 18. High-resolution satellite characteristics comparison

Source	Spatial resolution	Revisit time	Spatial coverage	Cost Per Sq. Km (USD)
PlanetScope	Multispectral: 3.7 m - 4.2 m	1 day	200 million km²/day	2.25
GeoEye 1	Multispectral: 1.64 m Panchromatic: 41 cm	1.7 days	700,000 km²/day	17.5
WorldView 4	Multispectral: 1.24 m Panchromatic: 31 cm	<1.0 day	680,000 km²/ day	22.5
Pleiades Neo	Multispectral: 1.20 m Panchromatic: 30 cm Pan sharpened: 30 cm	Twice daily	2 million km²/ day	22.5
Pleiades 1	Multispectral: 2.8 m Panchromatic: 70 cm	1 day	700,000 km²/day	12.5
SPOT 7	Multispectral: 6 m Panchromatic: 1.5 m	1 to 5 days	6 million km²/ day	4.75

(Airbus, 2012, 2013, 2021; EUSI, 2020; MAXAR, 2020; Planet Labs, 2022)

Annex 2- Interpreting ROC AUC values

The following table shows the interpretation of different ranges of ROC AUC (Khatami et al., 2017).

Table 19. Interpretation of the area under the ROC curve

Area under curve	Interpretation
Less than 0.7	No discrimination
0.7 to 0.8	Acceptable
0.8 to 0.9	Excellent
More than 0.9	Outstanding

Annex 3- ROC AUC of different grid sizes for damage classification

The following table shows the different accuracy values obtained by utilizing different grid sizes for damage detection.

Table 20. Area under curve of different grid sizes for damage detection

Grid size (m^2)	ROC-AUC
500	0.71
600	0.71
700	0.73
800	0.73
900	0.75
1000	0.81

Annex 4- Individual texture measure: Damage detection evaluation metrics

The following table shows the accuracy, precision, recall and F1 score of damage detection classification by individual texture measures.

Table 21. Evaluation metrics for damage detection of individual texture measures (using building footprints from densely populated areas)

Texture	Accuracy	Precision	Recall	F1
Angular Second Momentum	0.49	0.48	0.51	0.49
Contrast	0.50	0.49	0.53	0.51
Correlation	0.54	0.50	0.62	0.57
Dissimilarity	0.54	0.53	0.53	0.53
Entropy	0.52	0.52	0.52	0.52
Homogeneity	0.47	0.49	0.51	0.49
Mean	0.54	0.53	0.63	0.58
Variance	0.49	0.49	0.49	0.49

Annex 5- Comparing individual and clustered temporary shelters.

The following figure shows the difference in the pattern of temporary shelters, showing clustered and individual shelters from Nurgadi (AOI 3).

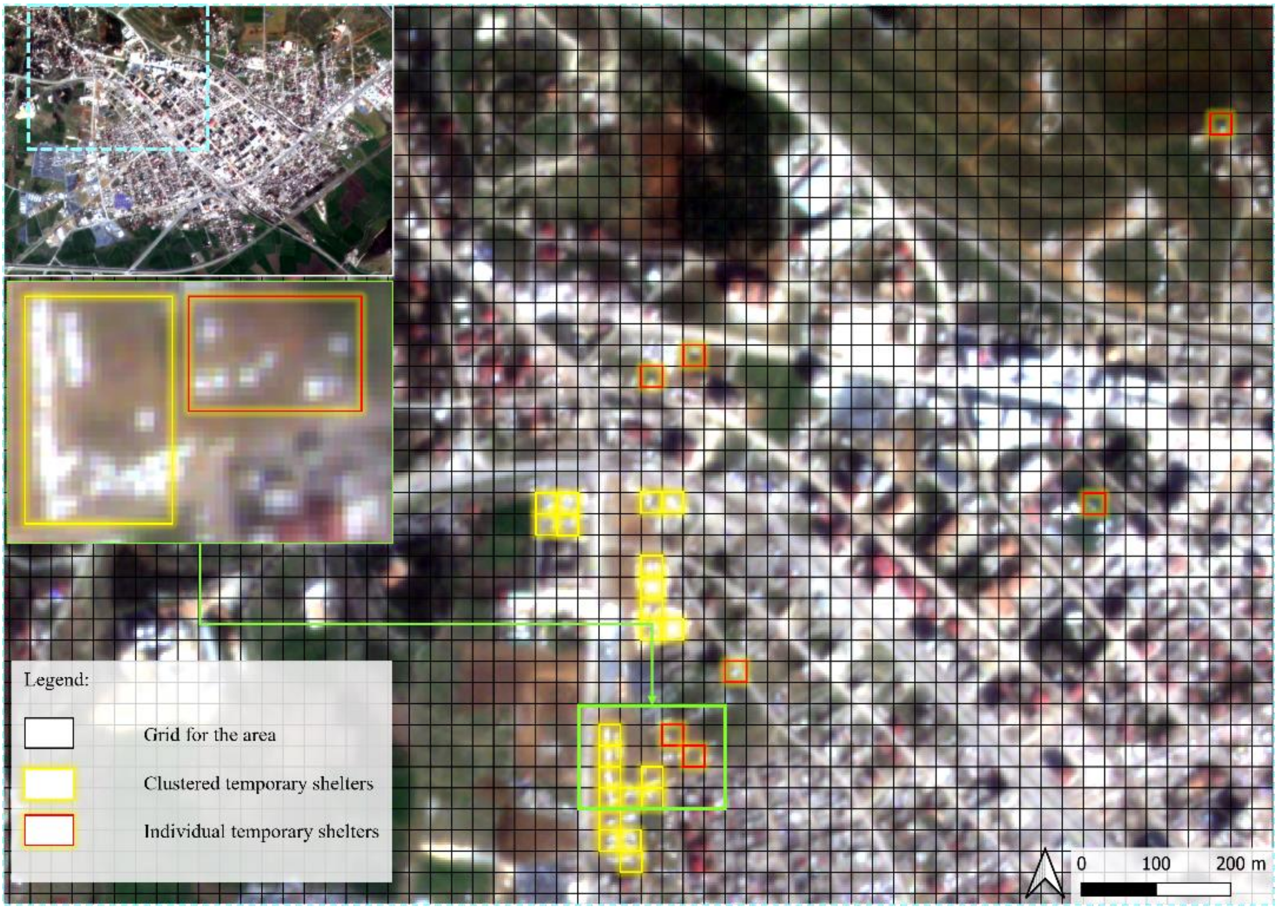

Figure 28. Individual versus clustered temporary shelters from Nurdagi (AOI 3)

Annex 6- Observed artefacts in PS images.

The following figure shows the artefacts and shadows observed in PS images that can potentially alter texture measures calculated from such images.

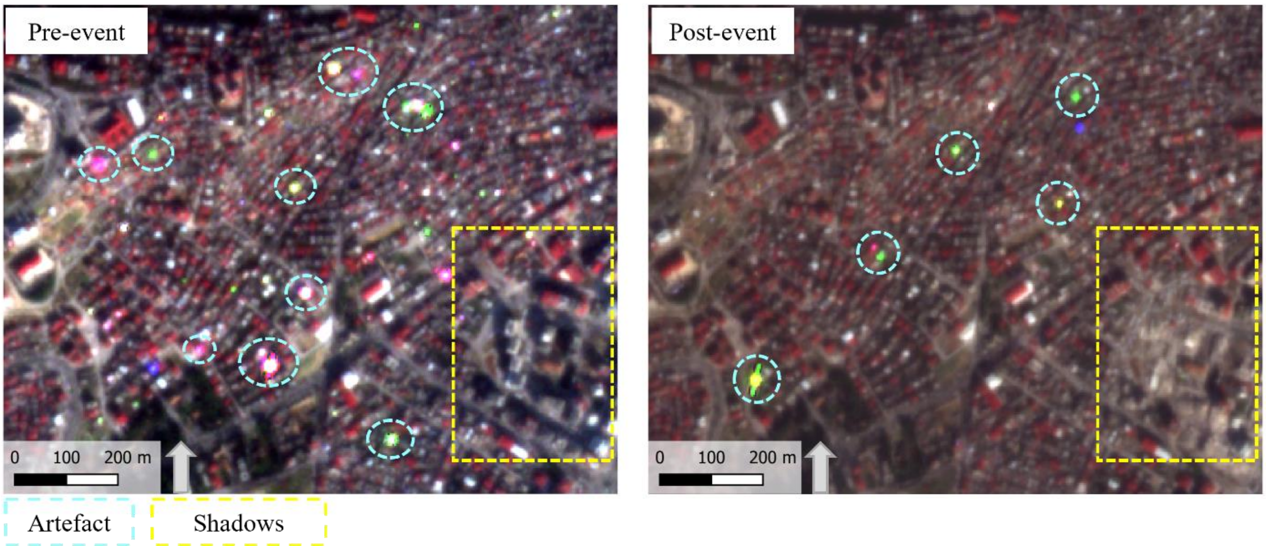

Figure 29. Observed artefacts in PS images Kahramanmaras (AOI 1)

Annex 7- ROC AUC of Debris classification.

The following plot shows the resulting ROC AUC of the texture measure angular second momentum (ASM) from the classification of debris. This plot highlights the smaller number of samples in 'debris disposal site' class, through the noticeable less smooth curve of that class.

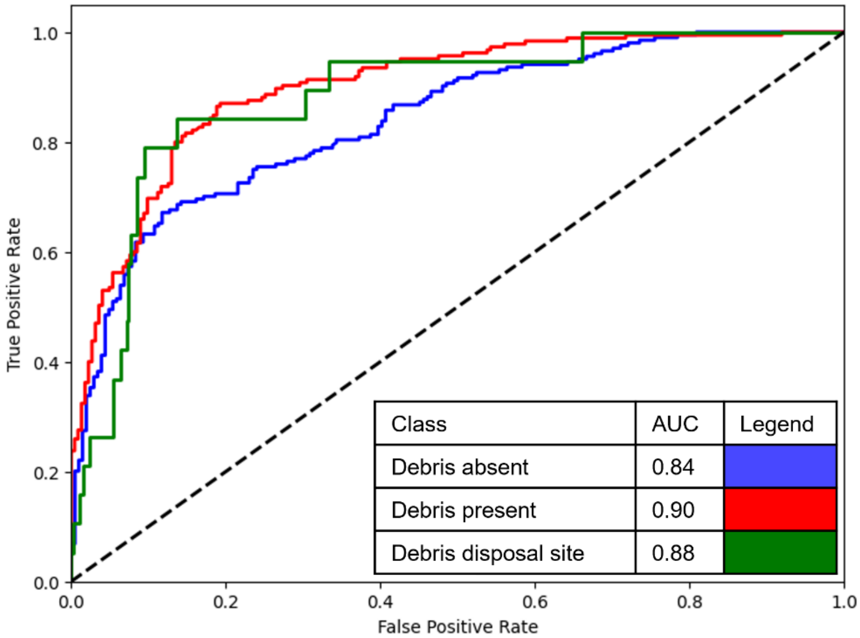

Figure 30. Area under the ROC curve for debris classification (ASM)

Annex 8- Calculating cumulative area and rate of expansion of temporary shelters.

The following table presents data on the cumulative area and rate of expansion of temporary shelters in Nurdagi (AOI 3). It includes the grid area covered by temporary shelters, the cumulative count of grids, the estimated total area, the difference in area between consecutive dates, the number of days between measurements, and the rate of expansion in m^2.

Columns:

- T- Dates of measurements.
- A- Fixed area of grid unit.
- B- Total number of grids covered by temporary shelters on each date.
- C- The product of the grid area (A) and the cumulative count of grids (B).
- D- Difference in total area covered between the current (T_n) and the previous (T_{n-1}) measurement.
- E- The number of days between the current and the previous measurement.
- F- The rate of expansion calculated by dividing the difference in area by the number of days.

Table 22. Calculation of cumulative area and rate of expansion of temporary shelters in Nurdagi (February-March)

T	A	B	C	D	E	F
Dates (2023)	Grid area (m^2) (1 grid unit)	Cumulative count of grids covered by temporary shelters	Estimate of total area covered (m^2) (A * B)	Difference in area (m^2) $C(T_n-T_{n-1})$	No. of days	Rate of expansion (m^2/day) (D/E)
02/02	800	0	0	0	0	0
08/02	800	33	26400	26400	6	4400
10/02	800	42	33600	7200	2	3600
13/02	800	134	107200	73600	3	24533.33
15/02	800	228	182400	75200	2	37600
18/02	800	275	220000	37600	3	12533.33
21/02	800	341	272800	52800	3	17600
24/02	800	386	308800	36000	3	12000
26/02	800	420	336000	27200	2	13600
01/03	800	462	369600	33600	3	11200
09/03	800	545	436000	66400	8	8300

As of March 9, 2023, container settlements cover 6% of the total area available in the AOI.

Annex 9- Kernel density estimation for debris.

The following figure visualizes KDE to quantify the distribution of debris in Antakya (AOI 6). The map overlays KDE results on the PS image of the location, highlighting areas with varying densities of debris.

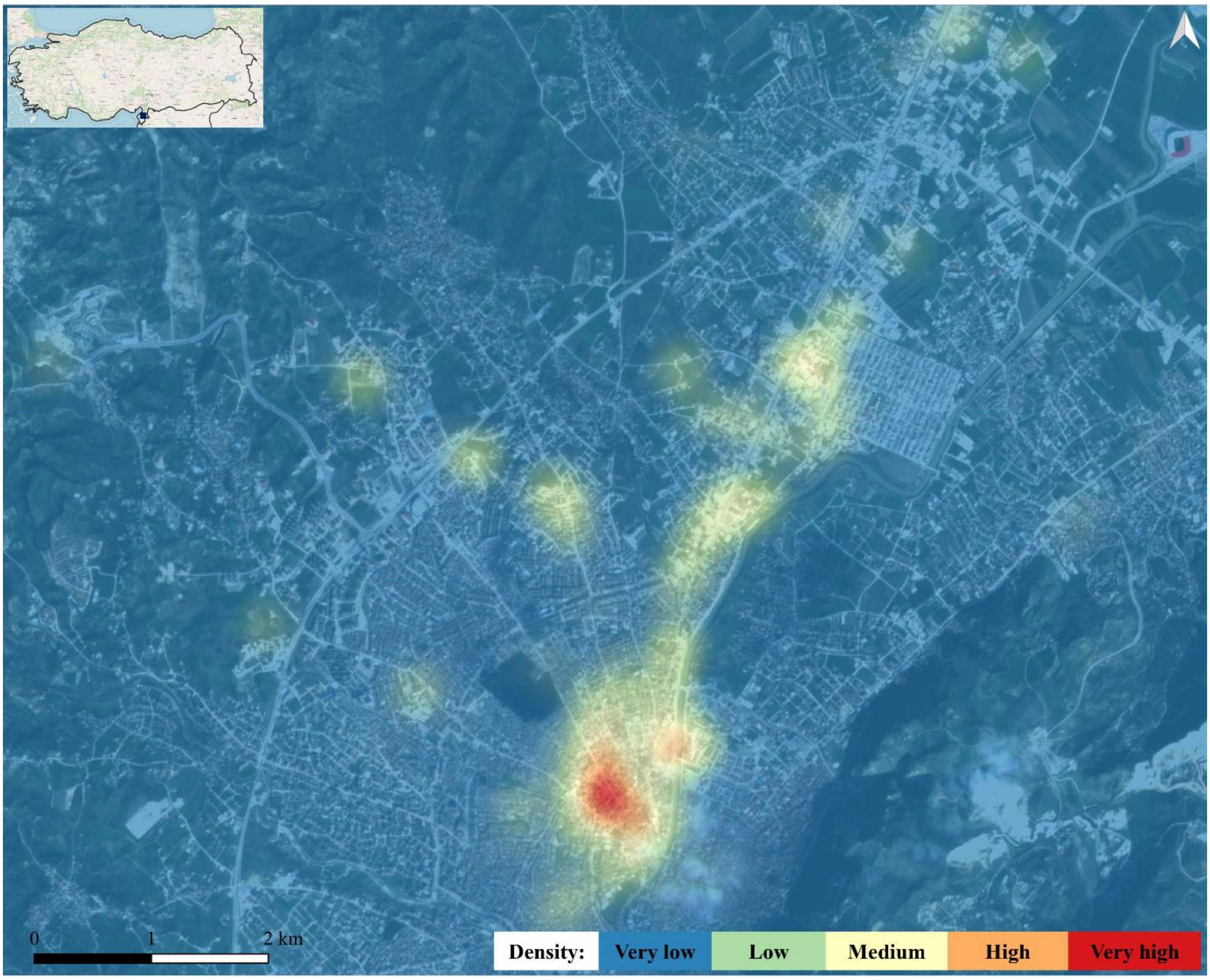

Figure 31. Kernel Density Estimation output for Antakya (AOI 6) showing debris density as of 12 February 2023